Double Negative Metamaterials in Dielectric Waveguide Configurations

Jeffrey R. Clark

Dissertation submitted to the Faculty of the
Virginia Polytechnic Institute and State University
in partial fulfillment of the requirements for the degree of

Doctor of Philosophy
in
Electrical Engineering

Ahmad Safaai-Jazi, Chair
Ioannis M. Besieris
Sedki M. Riad
Timothy Pratt
Werner E. Kohler

August 8, 2006
Blacksburg, Virginia

Keywords: Double Negative Metamaterials, Dielectric Waveguide, Pulse Propagation, Dispersion Characteristics

Copyright 2006, Jeffrey R. Clark

Double Negative Metamaterials in Dielectric Waveguide Configurations

Jeffrey R. Clark

ABSTRACT

With the recent resurgence of interest in double negative (DNG) materials and the reported construction of a metamaterial with DNG characteristics, applications of these materials become feasible and examination of the behavior of systems and devices a potentially fruitful topic. The most promising area of research, upon inquiry into past work related to DNG materials, proves to be dielectric waveguides. The present investigation, then, focuses on the inclusion of DNG materials in various planar dielectric waveguide configurations. These waveguides involve a core region surrounded by various numbers of symmetrically-placed cladding layers.

The present investigation involves the review of the electromagnetic properties of DNG materials by a thorough analysis based on Maxwell's equations. The use of a negative index of refraction for these materials is justified. These results are then used to perform a frequency domain analysis of an N-layer formulation for dielectric waveguides which is general for any combination of DNG and double positive (DPS) materials. This N-layer formulation allows for the derivation of the characteristic equation, which relates the operating frequency and the propagation constant solutions, along with the cutoff conditions and field distributions. A causal material model which obeys the Kramers-Kronig relations and which is based on measurements of a realized metamaterial is studied and used in the investigation in order to produce realistic results.

The N-layer formulation is then applied to the three-layer (slab) waveguide and known results are reviewed. A new interpretation of intramodal degeneracy is given, whereby degenerate modes are split into two separate modes, one with positive phase

velocity and one with negative phase velocity but both with a causal positive group (energy) velocity. Next, the formulation is applied to the five-layer waveguide. New behaviors are observed in this case which are not seen for the three-layer waveguide, including the return of the fundamental mode in some cases, whereas it is never present for the three-layer guide, the absence of certain higher-order modes in some situations and the appearance of new modes. Additionally, for some configurations the order of the even and odd modes in the DNG frequency range is found to be reversed from that of conventional waveguides.

The photonic crystal waveguide, which involves an infinite number of periodically placed cladding layers, is next studied using ray analysis, and a slight variation of the N-layer formulation is used to compare these results with those of the pseudo-photonic crystal waveguide. The pseudo-photonic crystal waveguide is identical to the photonic crystal waveguide with the exception that it has only large but finite number of layers. It is seen that the results of these two cases are similar for conventional modes, but the photonic crystal waveguide allows for new modes called photonic crystal modes which are inaccessible through conventional waveguides. Interesting phenomena such as mode crossings among the photonic crystal modes are observed and discussed.

Using the results from the frequency domain analysis of the five-layer waveguide, a Fourier transform technique is used to study pulse propagation in a waveguide containing DNG materials. A Gaussian pulse is launched in the waveguide over the frequency range covering a portion of the positive- and negative-phase-velocity fundamental transverse electric (TE) modes. Splitting of the input pulse into two separate pulses is observed, where both of these new pulses have a causal, positive energy velocity. The interpretation of intramodal degeneracy given in previous discussions is buttressed with evidence from this portion of the investigation, thus completing the analysis and bringing the present study to its conclusion.

Acknowledgement

I would like to thank my advisor, Dr. Ahmad Safaai-Jazi, for all his time, effort and patience in helping me complete my doctoral work. Thanks are also due to my committee members, Drs. Ioannis Besieris, Timothy Pratt, Sedki Riad and Werner Kohler for their service. My appreciation also goes to my parents who have encouraged me throughout my years of study.

My greatest thanks go to the Lord – Father, Son and Holy Spirit – for health, safety and blessing, and for the strength to seek, in this small way, to think his thoughts after him.

Table of Contents

1 Introduction 1

1.1 Double negative (DNG) metamaterials 2
1.2 Metamaterials as macroscopic dielectric/magnetic materials 4
1.3 A realized DNG metamaterial 5
1.4 Drawbacks and debates 9
1.5 Possible resolutions 11

2 Survey of Past Work 13

2.1 Radiating structures 13
2.2 Guiding structures 15
2.2.1 Dielectric waveguides 17
2.3 Scattering by DNG structures 18
2.4 Summary and research motivation 19

3 Electromagnetic Analysis of DNG Materials 21

3.1 Monochromatic plane wave incident on an arbitrary semi-infinite material 21
3.2 Sign choice for index of refraction in DNG materials 33

4 Planar Dielectric Waveguides Containing DNG Materials 37

4.1 Mathematical foundations 37
4.2 Planar dielectric waveguide 40
4.3 Three-layer dielectric waveguide 45
4.3.1 Even TE modes 46
4.3.2 Odd TE modes 46
4.3.3 Even TM modes 47
4.3.4 Odd TM modes 47
4.3.5 Limits on the propagation constant β 47
4.4 Cutoff conditions 50
4.4.1 Fast-wave modes 50
4.4.2 Slow-wave modes 51
4.5 Numerical analysis of a DPS waveguide 52
4.6 DNG material models 54
4.7 Calculation of loss 58
4.8 Solutions for a DNG slab 60
4.8.1 Group and phase velocities 64
4.8.2 Loss calculation 67

4.9 Summary 68

5 Five-layer Dielectric Waveguide 69

5.1 Characteristic equations 69
5.1.1 Even TE modes 70
5.1.2 Odd TE modes 71
5.1.3 Even TM modes 72
5.1.4 Odd TM modes 72
5.1.5 Limits on the propagation constant β 73
5.2 Cutoff conditions 73
5.2.1 Fast-wave modes 74
5.2.1 Slow-wave modes 76
5.3 Numerical analysis 78
5.3.1 DPS waveguide 78
5.3.2 Refractive index profiles 81
5.3.3 Appearance of new modes 87
5.3.4 Field distributions 89
5.4 Summary 91

6 Photonic Crystal Waveguide 92

6.1 Ray analysis 92
6.2 Pseudo-photonic crystal waveguide 100
6.3 Unique features of the photonic crystal waveguide 105
6.4 Numerical analysis and comparison 106
6.4.1 DPS photonic crystal waveguide 106
6.4.2 DNG photonic crystal waveguide 109
6.5 Summary 112

7 Pulse Propagation in DNG Dielectric Waveguides 113

7.1 Five-layer DNG waveguide 113
7.2 Discrete Fourier analysis 114
7.2.1 Gaussian pulse 115
7.3 Mode excitation 117
7.4 Pulse propagation 119
7.4.1 Numerical results 120
7.5 Summary 122

8 Conclusion 123

8.1 Summary of results 123
8.1.1 Three-layer DNG waveguide 124
8.1.2 Five-layer DNG waveguide 124
8.1.3 Photonic crystal DNG waveguide 125
8.1.4 Pulse propagation in DNG waveguides 125
8.2 Suggestions for further study 126

References 128

Vita. 135

List of Figures

Figure 1-1. An ideal DNG slab takes light from object A and focuses it at image B. . . . 3

Figure 1-2. A square (left) and circular (right) split-ring resonator (SRR). 6

Figure 1-3. A unit cell for an isotropic, negative permeability metamaterial. 6

Figure 1-4. A broadside-coupled SRR on a dielectric slab. 7

Figure 1-5. A two-dimensional DNG metamaterial using wire strips and (square) SRRs. (Reprinted with permission from [4]. Copyright 2006 AAAS.) 8

Figure 1-6. Measurement of refraction for a sample of DNG metamaterial. (Reprinted with permission from [4]. Copyright 2006 AAAS.) 8

Figure 1-7. The real (solid blue) and imaginary (dashed red) parts of the permeability for an SRR metamaterial. The real part of the permeability is negative for only a small range of frequencies near resonance. High loss and dispersion are apparent. Unity is plotted as a reference (dot-dashed black). 9

Figure 1-8. A depiction of refraction from a DPS material to a DNG material and the causality issues raised by this phenomenon. 10

Figure 1-9. A unit cell for an L-C based DNG metamaterial. 12

Figure 2-1. A portion of a backward-wave radiating coplanar-waveguide-based antenna. 14

Figure 2-2. Surface waves traveling along a ground plane (a) are suppressed by a corrugated high-impedance surface (b). 15

Figure 2-3. A square metallic waveguide filled with periodically placed split-ring resonators. 17

Figure 2-4. Two coupled slab waveguides, each of which may be either DNG or DPS and have frequency-dependent material parameters. 18

Figure 3-1. Ray diagram of a plane wave (k_i) incident from a semi-infinite medium (ε_1,μ_1) onto another semi-infinite medium (ε_2,μ_2), resulting in reflected (k_r) and (refracted) transmitted (k_t) waves. n_i is the normal unit vector to the interface. 22

Figure 3-2. The case of E-field perpendicular to the plane of incidence. 26

Figure 3-3. The case of E-field parallel to the plane of incidence. 26

Figure 3-4. The area S, centered on the material interface (shown in profile), is bounded by C. n is a unit vector normal to the interface. 27

Figure 3-5. The area S is a 'pillbox' of height h centered on the interface. n is a unit vector normal to the interface surface. 28

Figure 3-6. Comparison of the implications of a positive index of refraction (left) and a negative index of refraction (right) in a DNG medium. In both cases, a plane wave is incident from a DPS material onto a DNG material. 34

Figure 3-7. An incident plane wave (k_i) from a DPS material refracts negatively in a DNG material (k_t). The reflected wave (k_r) acts as usual. 36

Figure 4-1. Geometry and parameters for a two-dimensional dielectric waveguide with N layers, where $m = {}^{N+1}\!/_{2}$ 41

Figure 4-2. The three-layer (slab) waveguide. 45

Figure 4-3. The TE dispersion characteristics for a simple slab waveguide. Both even and odd modes are shown, where starting from the left the modes are designated TE_0, TE_1, TE_2, etc. 53

Figure 4-4. Normalized field distributions for the TE_0 mode at a normalized frequency of V = 2.21. The factor A_1 is the initial amplitude of the z-component of the magnetic field, and *a* is half the width of the slab. 54

Figure 4-5a. The material parameters ε_r' (left) and μ_r' (right) as a function of frequency f. 56

Figure 4-5b. The material parameters ε_r'' (left) and μ_r'' (right) as a function of frequency f. 57

Figure 4-6. The ratio of ε_r'/ ε_r" (dot-dashed blue) and μ_r'/ μ_r" (solid red). The level of 100 is marked with the broken line as an approximate reference above which the perturbation method is valid. 57

Figure 4-7. The TE dispersion characteristics of a DNG slab waveguide (solid black). The absolute value of n_1 (dashed red) is also plotted for reference. Modes below approximately 10.33 GHz are segmented or unseen due to limited numerical sampling and an infinite density of modes in the neighborhood of 10.3 GHz. 61

Figure 4-8. The TM dispersion characteristics of a DNG slab waveguide (solid black). The absolute value of n_1 (dashed red) is plotted for reference. A close-up of the lower right-hand portion of the plot is inset. Modes below approximately 10.33 GHz are segmented or unseen due to limited numerical sampling and an infinite density of modes in the neighborhood of 10.3 GHz. 61

Figure 4-9. Normalized field distributions for the TE_0 mode of a DNG slab waveguide at a frequency of f = 10.7 GHz. The factor A_1 is the initial amplitude of the z-component of the magnetic field, and *a* is half the width of the slab. 63

Figure 4-10. The actual TE dispersion characteristics for a DNG waveguide. The causally valid solutions (solid black) and the causally invalid solutions (dashed black) are both shown. Both positive and negative values of n_1 (dot-dashed red) are plotted for reference. 65

Figure 4-11. The power flow density (Poynting vector) for a fast-wave mode in a DPS slab waveguide (a) and a slow-wave mode in a DNG slab waveguide (b). Magnitude is depicted by arrow length in the first order and by arrow color in the second order. 66

Figure 4-12. The loss parameter α for the fundamental TE_0 mode from Figure 4-7. The results from both the perturbation method (black) and an exact method (red) are shown. The results are in close agreement. 67

Figure 5-1. A two-dimensional five-layer (quadruple-clad) dielectric waveguide. 69

Figure 5-2. The TE dispersion characteristics for a five-layer waveguide with a = 1m, b = 2m, all permeabilities equal to μ_0, $n_1 = 1.2$, $n_2 = 1.1$ and $n_3 = 1.0$. 79

Figure 5-3. The TM dispersion characteristics for a five-layer waveguide with a = 1m, b = 2m, all permeabilities equal to μ_0, $n_1 = 1.2$, $n_2 = 1.1$ and $n_3 = 1.0$. 79

Figure 5-4. The field distributions for the TE_0 mode of the five-layer waveguide from Figure 5-2 at 500 MHz. 80

Figure 5-5. The four possible refractive index magnitude profiles containing one set of DNG layers (core or inner cladding). The DNG layers vary from zero to negative infinity with frequency. The profiles are not necessarily to scale. 81

Figure 5-6. The TE (a) and TM (b) dispersion characteristics for a five-layer waveguide with the refractive index profile of Figure 5-5(a). Both the positive (solid black) solutions and negative (dashed black) solutions are shown. The first few modes are labeled with the appropriate notation. The guide parameters are a = 0.5cm, b = 1cm, $n_3 = 1.0$, $n_2 = 1.4$ and n_1 is governed by the material model of (4-65) and (4-66) and the parameters given in [4]. The maximum refractive index (dot-dashed red) is also shown. 82

Figure 5-7. The TE (a) and TM (b) dispersion characteristics for a five-layer waveguide with the refractive index profile of Figure 5-5(b). Both the positive (solid black) solutions and negative (dashed black) solutions are shown. The first few modes are labeled with the appropriate notation. The guide parameters are a = 0.5cm, b = 1cm, $n_3 = 1.4$, $n_2 = 1.0$ and n_1 is governed by the material model of (4-65) and (4-66) and the parameters given in [4]. The maximum refractive index (dot-dashed red) is also shown. 83

Figure 5-8. The TE (a) and TM (b) dispersion characteristics for a five-layer waveguide with the refractive index profile of Figure 5-5(c). Both the positive (solid black) solutions and negative (dashed black) solutions are shown. The first few modes are labeled with the appropriate notation. The guide parameters are a = 0.5cm, b = 1cm, $n_3 = 1.0$, $n_1 = 1.4$ and n_2 is governed by the material model of (4-65) and (4-66) and the parameters given in [4]. The maximum refractive index (dot-dashed red) is also shown. 84

Figure 5-9. The TE (a) and TM (b) dispersion characteristics for a five-layer waveguide with the refractive index profile of Figure 5-5(d). Both the positive (solid black) solutions and negative (dashed black) solutions are shown. The first few modes are labeled with the appropriate notation. The guide parameters are a = 0.5cm, b = 1cm, $n_3 = 14$, $n_1 = 1.0$ and n_2 is governed by the material model of (4-65) and (4-66) and the parameters given in [4]. The maximum refractive index (dot-dashed red) is also shown. 85

Figure 5-10. The TE dispersion characteristics for a five-layer waveguide also examined in Figure 5-6, but for b = 1.5cm (a), b = 2.25cm (b) and b = 3cm (c). The maximum refractive index (dot-dashed red) is shown for reference. Positive phase velocity solutions (solid black) are shown along with negative phase velocity solutions (dashed black). 88

Figure 5-11. The normalized field distributions for the TE_0 mode for the waveguide in Figure 5-6 at 67.5 GHz (a), Figure 5-7 at 67.1 GHz (b), Figure 5-8 at 67.5 GHz (c) and Figure 5-9 at 67.1 GHz (d). 90

Figure 6-1. Refractive index profile of a photonic crystal waveguide. 93

Figure 6-2. Three-layer planar structure with incident ray (plane wave). 93

Figure 6-3. Input impedance for an infinitely layered cladding (top) is the same as that of the same cladding, less the first two layers (bottom). 95

Figure 6-4. A ray incident on an infinitely layered structure. The input impedance is periodic, and therefore the top and bottom diagrams are equivalent. 96

Figure 6-5. A ray incident on an infinitely layered structure. The input impedance is periodic, and therefore the top and bottom diagrams are equivalent. 96

Figure 6-6. Geometry and parameters for a two-dimensional photonic crystal waveguide. 99

Figure 6-7. TE dispersion characteristics (solid) for the photonic crystal waveguide with $d_0 = d_1 = d_2 = 1$cm, $\mu_1 = \mu_0$, $\mu_2 = \mu_0$, $\varepsilon_1 = 2.25\ \varepsilon_0$ and $\varepsilon_2 = \varepsilon_0$. The boundary between conventional modes and photonic crystal modes is denoted by a dashed line. 107

Figure 6-8. TM dispersion characteristics (solid) for the photonic crystal waveguide with $d_0 = d_1 = d_2 = 1$cm, $\mu_1 = \mu_0$, $\mu_2 = \mu_0$, $\varepsilon_1 = 2.25\ \varepsilon_0$ and $\varepsilon_2 = \varepsilon_0$. The boundary between conventional modes and photonic crystal modes is denoted by a dashed line. 107

Figure 6-9. Comparison of the solution for the TE_0 mode at 2.5 GHz for the photonic crystal waveguide (broken) and the pseudo-photonic crystal waveguide with a varying number of layers (solid). 108

Figure 6-12. Normalized field distributions for the TE_1 mode at (a) 6 GHz ($\bar{\beta} = 0.355627$) and at (b) 10 GHz ($\bar{\beta} = 1.10629$). 109

Figure 6-11. TE (a) and TM (b) dispersion characteristics for the photonic crystal waveguide with n_1 (dot-dot-dashed red) being DNG and $n_2 = 1$. All layers have a width of 5mm. The positive-phase-velocity modes (solid black) and the negative-phase-velocity modes (dashed black) are expressed as absolute values. The dot-dashed line indicates the border between conventional solutions and photonic crystal solutions. 110

Figure 6-12. Electric field distribution (e_y) for the TE_{0-} mode of a photonic crystal waveguide whose dispersion characteristics are given in Figure 6-11(a). The field distribution is shown for solutions at 10.6 GHz (a) and 10.7 GHz (b). 111

Figure 7-1. TE dispersion characteristics for a five-layer waveguide with both the positive-phase-velocity modes (solid black) and negative-phase-velocity modes (dashed black) shown as positive absolute values. The DNG refractive index n_1 (dot-dashed red) is shown for reference. 114

Figure 7-2. A magnification of the TE_{0+} (solid black) and TE_{0-} (dashed black) dispersion characteristics for the five-layer waveguide. The absolute value of the refractive index n_1 (dot-dashed red) is shown for reference. The pulse frequency amplitude distribution (dot-dot-dashed blue) is also shown. . . . 116

Figure 7-3. Absolute value of the normalized Fourier transform of (7-3) in the time domain. 116

Figure 7-4. A plane wave with frequency distribution $A(\omega)$ incident on the face of a five-layer dielectric waveguide with length L. 117

Figure 7-7. Absolute value of the normalized electric field output at x = 0 of a five-layer DNG waveguide of length L = 1m (a), L = 5m (b) and L = 25m (c), plotted in terms of the time delay. Insets in (c) show magnifications of the pulse tails. 121

1 Introduction

In 1968, Veselago's investigation into the dynamics of materials with simultaneously negative permittivity and permeability was published [1]. Although at the time such materials were unknown, recent developments by Smith and others [2-5] have shown that artificial (or synthetic) materials, or so-called 'metamaterials,' can be constructed which seem to produce these negative material parameters simultaneously. These metamaterials are identified using various names in the literature, as no terminology has of yet been generally agreed upon. The phrase "double negative" (DNG) materials will be used in this discussion, as it is arguable that this is the most descriptive expression.

There have been disagreements and debates over various aspects of DNG metamaterials, and the precise dynamics of waves in a DNG metamaterial have not been fully agreed upon. Claims regarding the potential of DNG metamaterials range in impressiveness. Pendry has suggested, for example, that a DNG slab can act as a so-called "perfect lens" [6] utilizing the reversal of Snell's law in DNG materials which results in negative refraction. On the other hand, it is argued elsewhere that a perfect lens is impossible due to anisotropy, absorption and dispersion in the metamaterial [7,8] and even that negative refraction is impossible on grounds of violation of causality [9]. Smith *et al.*, however, have claimed to have actually measured negative refraction [4,5], while others have questioned their results as being either misinterpreted or not accounting for various factors [10].

Needless to say, then, the subject of DNG metamaterials is a controversial one which is embroiled in many debates. If it is assumed that DNG materials are truly realizable as Smith and others have suggested, then one may inquire as to their potential applicability to the subject of guiding structures such as dielectric waveguides. It will be convenient, before providing an overview of the work accomplished up to the present in this particular area, to present a basic model of metamaterials followed by a brief

synopsis of past research in the development of DNG metamaterials. Some other variations on the theme of metamaterials in general will also be mentioned. A thorough mathematical model of DNG materials will be presented starting with Maxwell's equations. Based on this fundamental approach, applications to dielectric waveguides may be examined in depth. Specifically, planar dielectric waveguides will be investigated using material models from the literature. Although theoretical in nature, the results obtained from this analysis are based upon reported experimental results and, therefore, may be reasonably expected to correspond to actual results should experiments be performed at a future date.

1.1 Double negative (DNG) metamaterials

Although first investigated theoretically in some detail in 1968 by Veselago [1], DNG materials have remained largely unnoticed until recently due to the seemingly unrealizable nature of such materials. A DNG material is defined as having simultaneously negative real components of the permittivity ε and permeability μ. Although interesting in theory, no DNG materials had been found in nature, and therefore further study seemed to be a rather futile endeavor. Since that time, the reported construction of a DNG *metamaterial* (or artificial material) has roused interest in the subject and made it an important and highly debated topic of research.

One of the most interesting statements by Veselago in his paper on DNG materials (then called 'left-handed' materials due to the fact that the **E**, **H** and **k** vectors form a left-handed triad in such materials) is that the index of refraction n, which is related to the relative permittivity and permeability of the material by $n^2 = \mu_r \varepsilon_r$, is negative. This means that the *negative* square root of the product of ε_r and μ_r must be taken, whereas in a double positive (DPS) material the positive root is used. (A double positive material is defined as one in which the real components of μ and ε are simultaneously positive.) If Snell's law holds, then this implies that a wave entering a DNG material from a DPS material (or vice versa) will refract negatively. Figure 1-1 shows a canonical illustration of the imaging properties of a DNG slab.

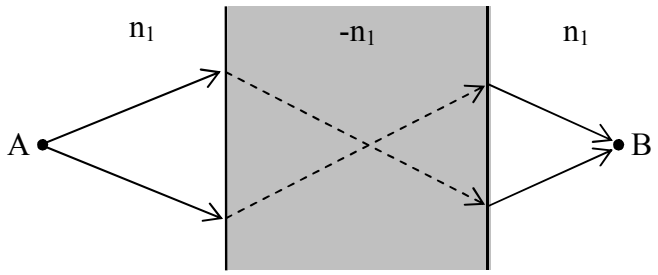


Figure 1-1. An ideal DNG slab takes light from object A and focuses it at image B.

Additionally, Veselago predicted that both the Doppler and Cerenkov effects would be reversed in DNG materials and that radiation pressure (viewed as photons reflecting off a surface) will become radiation tension due to the reversal of the wave vector **k**. It is interesting and important to note that although there is negative phase velocity in a DNG material, the Poynting vector, and thus energy velocity, are in a positive direction (*i.e.*, away from the source). Later, Veselago also suggested a more general form of Fermat's principle of light travel which takes into account DNG as well as DPS materials [11].

It was also suggested in Veselago's paper that dispersion is unavoidable in a DNG material, since otherwise the total energy stored in the material would be negative [1]. It was further argued that a DNG material cannot be isotropic due to the fact that magnetic fields are produced by dipoles rather than charges, unlike electric fields. Although this difficulty could be surmounted in theory, no magnetic monopoles (charges) have yet been discovered. Other papers have also discussed issues of wave propagation in a DNG material [12-18], and some of the details of this subject will enter into the present analysis.

In spite of real or potential drawbacks of DNG materials, the reversal of common phenomena, like refraction, in such materials make them something of a "holy grail" in physics and engineering. This has lead to attempts in recent years to make artificial materials, or 'metamaterials.'

1.2 Metamaterials as macroscopic dielectric/magnetic materials

Dielectric and magnetic materials affect the behavior of electromagnetic fields and waves, and therefore it is necessary to develop a model which accounts for these effects. The model of this behavior is represented mathematically using the material parameters ε (permittivity) and μ (permeability). These parameters appear in Maxwell's equations and the derivative equations governing electromagnetic fields and waves (*e.g.*, Coulomb's law and Faraday's law), and they relate the fields to their respective flux densities and primary sources, namely the charge and current densities. The material parameters arise from a model of dielectric (and magnetic) materials as consisting of polarizable (magnetizable) constituent elements, be they molecules, atoms, ions or subatomic particles. These constituent elements may be modeled in a continuous manner which allows for the characterization of a material, as far as electromagnetic phenomena are concerned, in two quantities which are generally complex tensors.

This model, which views matter as being constituted of a number of discrete atoms or molecules, may be extended from a microscopic form to a macroscopic form. That is, instead of a material being primarily constituted of microscopic particles as the primary governors of its characteristics, a material could be constructed of macroscopic elements (inclusions). This is a so-called 'metamaterial.' As long as the wavelength of operation for any radiation in the structure is much larger than the inclusion size and spacing, an array (2- or 3-dimensional) of inclusions essentially acts like a typical material (surface or volume) according to the theory.

The same principle which applies to the derivation of the permittivity and permeability of conventional materials may also be applied to metamaterials since it is, apparently, only a matter of scale. (Although this may be more or less true; given quantum theory it seems that issues of scale are not as simple as suggested.) Using this principle, materials may be engineered with specific permittivities or permeabilities, according to requirements. Pendry concisely stated this philosophy as follows [19]:

> *"The original objective in defining a permittivity ε and permeability μ was to present a homogeneous view of the*

electromagnetic properties of a medium. Therefore, it is only a small step to replace the atoms of the original concept with structure on a larger scale."

Some of the potential factors affecting these material parameters in a metamaterial are inclusion geometry, element spacing in the array, material composition of inclusions and electric sources in the case of an active metamaterial.

It is quite natural to attempt to utilize this theory as the basis for constructing a metamaterial with simultaneously negative permittivity and permeability, since such materials have not as yet been found either naturally occurring or as the product of more traditional materials engineering. Although the present review focuses primarily on DNG metamaterials, the concept of metamaterials may also be used for the purpose of enhancing the material parameters in a different manner. For example, it may be desirable to have a tuned value of permeability without using a dense, heavy material such as a ferrite. In such a case, a metamaterial might be a viable alternative. These other possibilities for synthetically producing a material with parameters which may be difficult or impossible to find in nature must not be discounted.

1.3 A realized DNG metamaterial

It has been known for some time how to construct a metamaterial with a negative permittivity [20,21]. A 3-dimensional array of intersecting, straight, thin wires acts as a neutral plasma, and when the frequency of operation falls below the plasma frequency, ε effectively becomes negative [22]. A more dynamic metamaterial with negative ε using loaded wire dipoles has been suggested [23]. Of interest, then, is constructing a metamaterial that will produce a negative permeability μ and which may also be combined with another metamaterial to produce both negative ε and μ. Alternatively, a simpler metamaterial which performs both functions would also be acceptable, if not superior. Until recently, attempts at finding a metamaterial with a negative permeability were unsuccessful. In 1999, Pendry, *et al.* [19], published a paper discussing, among

other things, a metamaterial with nonmagnetic, conducting inclusions which yielded an effective negative permeability at some frequencies. This metamaterial involved arrays of split-ring resonators (SRRs) that, near their resonant frequency, collectively act as an effective-negative-permeability material. A diagram of an SRR is shown in Figure 1-2.

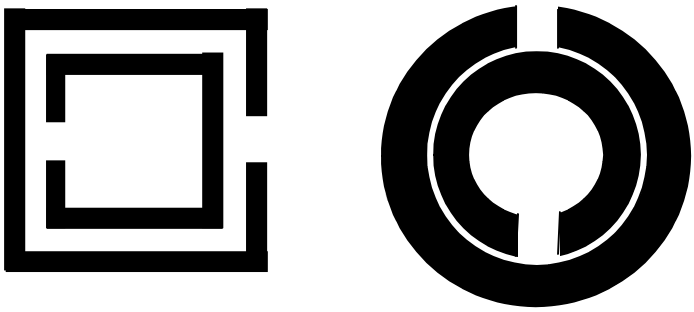


Figure 1-2. A square (left) and circular (right) split-ring resonator (SRR).

Interestingly, this metamaterial has variable magnetic properties (depending on the parameters of the SRRs and lattice spacing) while not utilizing magnetic inclusions. Also, by arranging SRRs in the unit cell appropriately (an example is shown in Figure 1-3), it is suggested that an isotropic metamaterial may be constructed which may avoid the anisotropy predicted by Veselago [1]. Modifications to the SRR, such as a change from edge-coupled to broadside coupled SRRs, have been proposed and shown to improve the performance of the inclusion and the metamaterial [24,25]. Figure 1-4 shows a broadside-coupled SRR.

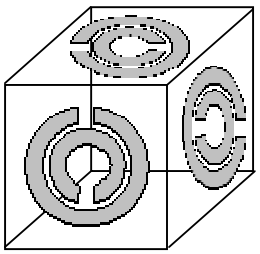


Figure 1-3. A unit cell for an isotropic, negative permeability metamaterial.

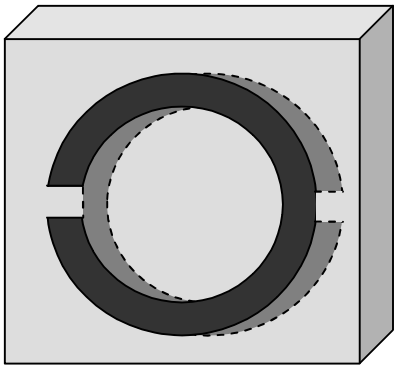


Figure 1-4. A broadside-coupled SRR on a dielectric slab.

In 2000, Smith *et al.* [2] claimed to have created a DNG metamaterial. This metamaterial follows the basic philosophy described thus far: an array of inclusions with specific properties was used to simulate a standard material, except with negative values for ε and μ. They gave a very concise statement of the approach to creating their metamaterial in the following [2]:

> *"A periodic array of conducting elements can behave as an effective medium for electromagnetic scattering when the wavelength is much longer than both the element dimension and lattice spacing."*

The metamaterial studied by Smith *et al.* consisted of a periodic array of split-ring resonators (SRRs) and metal posts or strips, as shown in Figure 1-5. It was found that by adjusting the appropriate parameters such that the range of frequencies near the resonance of the SRRs (where μ is negative) was below the plasma frequency of the wire array a DNG metamaterial could be produced. The initial metamaterial revealed DNG characteristics only for one direction of electromagnetic wave incidence and polarization (*i.e.*, one dimension). In 2001, the same group reported the construction of a two-dimensional DNG metamaterial. Transmission experiments on both the one- and two-dimensional metamaterials indicated the presence of a frequency band in which both ε and μ are simultaneously negative. Two-dimensional isotropy provides the ability to test such phenomena as refraction and the Doppler shift [5].

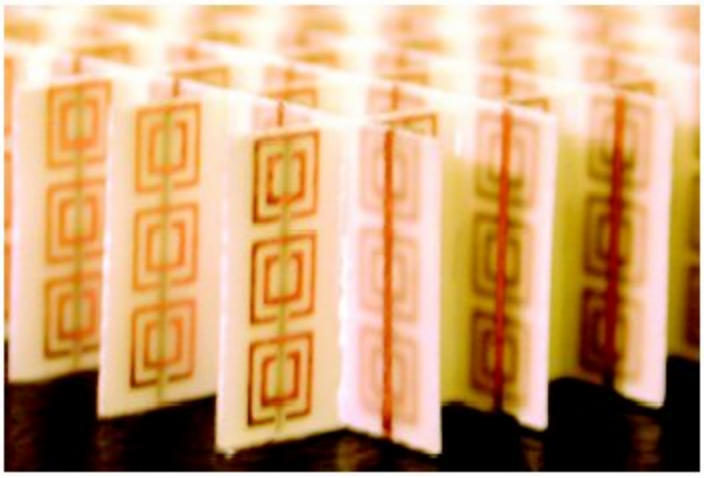


Figure 1-5. A two-dimensional DNG metamaterial using wire strips and (square) SRRs. (Reprinted with permission from [4]. Copyright 2006 AAAS.)

Smith *et al.* performed measurements on some samples of this metamaterial and claim to have measured negative refraction of an electromagnetic wave [4,5]. This is in accordance with the predictions made by Veselago decades earlier. A prism-shaped sample of the metamaterial was irradiated at microwave frequencies and the refraction angle measured. It would seem, therefore, that the goal of producing a DNG metamaterial has been attained. Figure 1-6 depicts the apparatus used for this experiment.

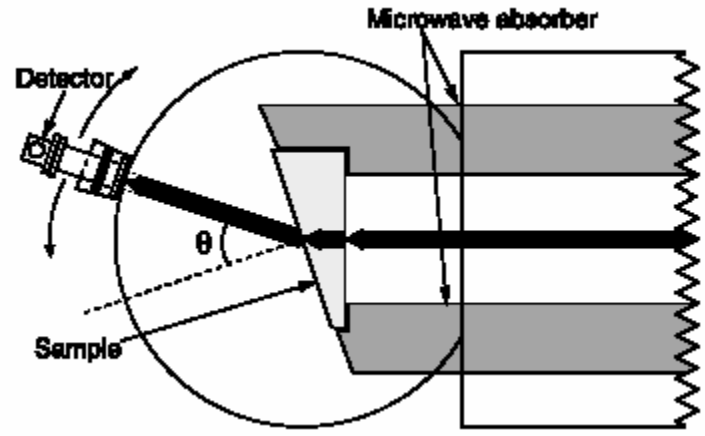


Figure 1-6. Measurement of refraction for a sample of DNG metamaterial. (Reprinted with permission from [4]. Copyright 2006 AAAS.)

1.4 Drawbacks and debates

In spite of the apparent success, the metamaterial developed by Smith *et al.* has its drawbacks and is still the subject of debate. For instance, the fact that the SRR produces a negative permeability only near its resonance implies that the metamaterial is necessarily highly dispersive. Figure 1-7 shows a graph of the permeability for the SRR array described by Pendry [19]. This confirms, for this metamaterial, Veselago's claim that DNG materials are inherently dispersive. Similarly, the bandwidth of the DNG regime is rather narrow. Losses are also a critical issue, and the metamaterial is moderately to highly lossy. It has been argued, however, that losses in the metamaterial can be reduced significantly [26]. Although these are some critical issues which limit the performance and potential of Smith's metamaterial, there are other issues more fundamental which have been raised in the literature.

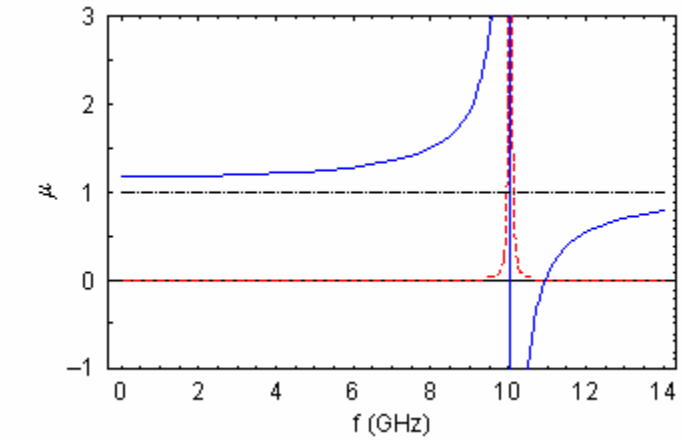


Figure 1-7. The real (solid blue) and imaginary (dashed red) parts of the permeability for an SRR metamaterial. The real part of the permeability is negative for only a small range of frequencies near resonance. High loss and dispersion are apparent. Unity is plotted as a reference (dot-dashed black).

Something of a side issue, but related to the present review, is the use of DNG materials to create a so-called "perfect lens" which, according to Pendry, would overcome the half-wavelength limit on image resolution [6]. This possibility has been contradicted in many papers through appeals to various factors including the nature and function of evanescent waves, the presence of surface waves and the inherent dispersion of the medium [7,8,12]. It has also been suggested that improvements in lens technology may be made using DNG metamaterials, but a "perfect lens" is still unattainable [27].

Additionally, whether or not negative refraction has in fact been measured has been questioned. Lindell *et al.* [29] have claimed that refraction from a DPS to DNG material is not negative but, rather, 'anomalous' (it is stated that a negative index of refraction is not compatible with Snell's law). Valanju *et al.* [9] have published at least one paper suggesting that negative refraction is, in fact, entirely impossible. It was argued in this paper that causality and finite signal speed requirements make negative wave signal refraction unrealizable (although negative phase refraction is admitted to be possible). They further suggest that the divergence of group and signal refraction results in inhomogeneous waves which decay rapidly as a result of their interaction with the DNG material. Figure 1-8 depicts refraction at the interface of a DPS and DNG material. It is argued that for negative refraction, the signal front in must rotate about a point, a phenomenon which violates finite signal speed restrictions.

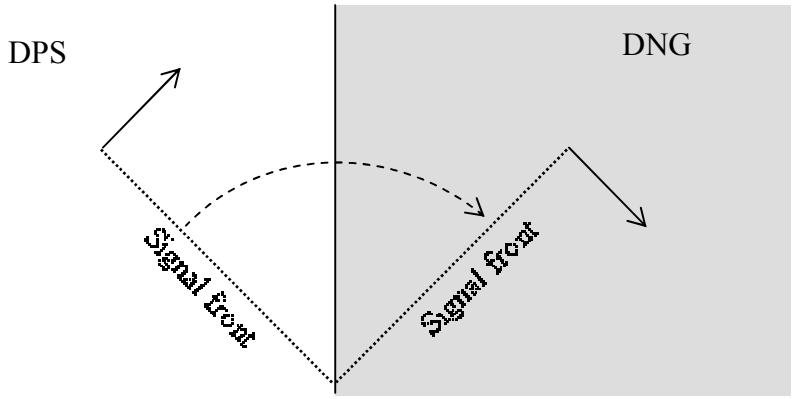


Figure 1-8. A depiction of refraction from a DPS material to a DNG material and the causality issues raised by this phenomenon.

In response to the above criticisms, Pendry, Smith and Schurig [30] published a paper claiming that both the group and phase fronts undergo negative refraction, but that the (previously undistinguished) interference fronts undergo positive refraction. They make this claim based on simulations of a modulated Gaussian beam passing through the interface between a DNG and a DPS material. Additionally, they are able to appeal to the experimental results obtained in [4].

In opposition to this, Garcia and Nieto-Vesperinas [8] have argued that Smith *et al.* have not truly measured negative refraction. They suggest that the lossy character of

the metamaterial in question leads to a complex refractive index, inhomogeneous waves and, therefore, no distinction between a negative index and positive index material. (Although in some cases a "negative index" material is the same as a 'DNG' material, in this case there is a distinction to be made).

In an attempt to address these concerns, Foteinopoulou *et al.* [31] conducted finite-difference time-domain analysis on DNG materials and found that when electromagnetic waves are incident upon a DNG material from a DPS material, there is in fact a delay period during which time the waves are 'trapped' at the interface. The waves are reorganized and then refract negatively to propagate through the DNG material. This delay time mitigates causality concerns since the signal front does not need to rotate about a point as was suggested in [9].

It is clear, then, that the issue of the reality of a negative index of refraction in a DNG metamaterial has not yet been settled. This implies, of course, that any investigation or research into potential applications of DNG metamaterials may have a certain number of ambiguities and misinterpretations associated with it.

1.5 Possible resolutions

Attempts to either resolve the difficulties with the current DNG metamaterials, or to simply realize new possibilities, have been made. It has been suggested that a composite made of alternating layers of negative ε material and negative μ material could act as a DNG material [32]. However, it has been found that, while this acts in some ways like a standard DNG material, it has some anomalous characteristics which make it appear to be more of a hybrid between a DNG and DPS material than a truly DNG material. Tretyakov [33] has suggested that the difficulties with DNG materials may be surmounted by utilizing active inclusions. The use of active elements in the metamaterial would improve the bandwidth, reduce losses and alleviate the causality restriction. Tretyakov proposes the use of loop and dipole antennas loaded with negative impedances (which are realizable with simple op-amp circuits). He also suggests that planar arrays of negatively loaded patches or strips could serve to create thin sheets of DNG material.

Transmission line theory has been used in order to understand and model the dynamics of DNG materials [34]. A two-dimensional metamaterial for RF/microwave circuit and device applications has been suggested using L-C loaded transmission lines [35]. While not having the three-dimensional potential of an SRR/wire metamaterial, it does allow for a much wider bandwidth. Also, if varacters are used in place of capacitors, dynamic control of the two-dimensional material parameters is possible. Figure 1-9 depicts the unit cell for this structure. Negative refraction and wave focusing in such a medium were observed in simulations [36]. Similarly, a two-dimensional planar form of metamaterial using SRRs has been analyzed and implemented [37].

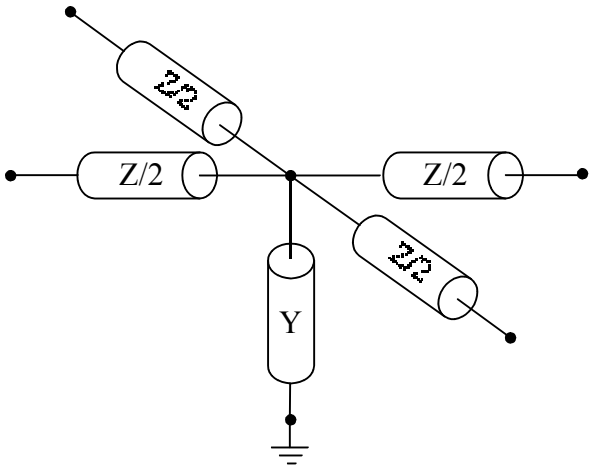


Figure 1-9. A unit cell for an L-C based DNG metamaterial.

As can be seen from the recent literature, DNG metamaterials are both interesting and controversial. The potential applications could be quite fascinating and useful. A broader category of metamaterials, not limited to DNG characteristics, have been discussed very lightly. Here, as well, it seems that potential for further research is available.

2 Survey of Past Work

Having presented a broad overview of double negative (DNG) metamaterials in the previous chapter, it is appropriate to review the most recent research into applications of these metamaterials. A general overview of the research in this area will be presented, including a more focused survey of research concerning applications of DNG metamaterials to dielectric waveguides.

There are essentially three areas of application for DNG metamaterials: radiating structures, guiding structures and scattering bodies. The first group includes such things as antennas, the second transmission lines and waveguides and the third scattering bodies such as spheres, cylinders and assorted other shapes. A brief discussion of recent research in each of these areas will be presented, including a more in-depth review of research related to guiding structures. After this review, the specific topic for this investigation will be identified.

2.1 Radiating structures

Not much work has been done in this area, and given the current forms of metamaterials it is unlikely that there will be many realizable applications for some time. In spite of this, it behooves the reader to take account of what has in fact been investigated. Ziolkowski and Kipple have examined the use of DNG materials as "matching networks" for antennas [38]. By using a DNG shell around an electrically small antenna, they showed that the radiated power of the antenna can be increased by orders of magnitude. Although such a design promises significant benefits, given the current types of available DNG metamaterials this is not realizable. For example, the three dimensional metamaterial developed by Smith *et al.* [2] is not as yet amenable to

spherical configurations. A spherical shell, especially a thin one, would present overwhelming mechanical as well as electromagnetic obstacles for this particular design.

Grbic and Eleftheriades [39, 40] have designed an antenna based on transmission line theory and its applications to planar negative refractive index metamaterials [35,36] that acts as a so-called 'backward-wave' radiating structure. The design is shown in Figure 2-1.

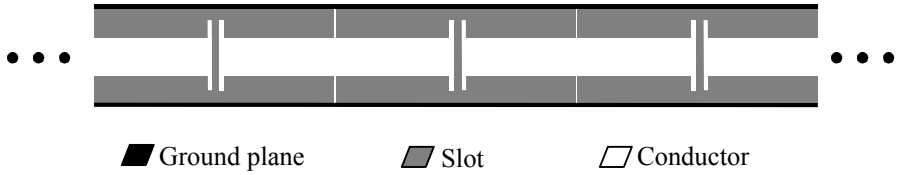


Figure 2-1. A portion of a backward-wave radiating coplanar-waveguide-based antenna.

Tayeb *et al*. [41] have used the concept of metamaterials to construct a ground plane with a low index of refraction for designing electrically compact, highly directive antennas. This ground plane involved stacks of layered wire grids and foam and follows the work of Pendry *et al.* in dealing with wire grids as metamaterials [42,43]. A monopole was experimentally tested in this structure and shown to have some of the expected results.

There has also been a significant amount of research in the area of so-called high impedance electromagnetic surfaces. Sievenpiper *et al.* [44] have pioneered this area of research and shown that, by appropriately constructing the geometry of a ground plane, surface waves may be suppressed by causing radiation rather than guidance, thus improving the radiation patterns of antennas. Such improvements include increased smoothness and a decrease in backward scattering. Figure 2-2 illustrates this result. These surfaces are modeled as having a 'forbidden' frequency band for propagation. Antennas operating over ground planes in the forbidden band will produce no (or highly suppressed) surface waves.

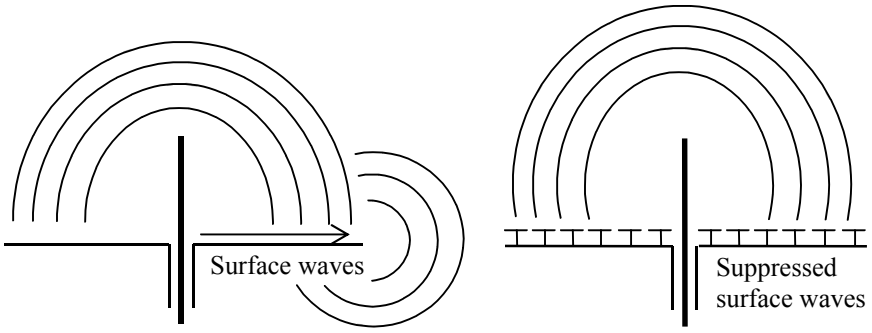


Figure 2-2. Surface waves traveling along a ground plane (a) are suppressed by a corrugated high-impedance surface (b).

Additionally, research has been performed on creating exotic textures to improve or refine the characteristics of these high-impedance surfaces. McVay *et al.* [45] have studied the effect of so-called Hilbert inclusions as the basis for the ground plane texture for antennas. They have observed through simulations improvement in gain and input impedance for dipoles over these surfaces.

2.2 Guiding structures

DNG metamaterials have been fairly widely applied, in theory and experiment, to waveguides. There has been significant research on dielectric, metallic and planar waveguides which employ, in some fashion, DNG metamaterials. To clarify, it is important to recognize that although artificial 'metamaterials' are the only presently realized media with negative effective permittivity and permeability, theoretical models may, for simplicity, simply utilize regular 'materials' which might also be considered 'natural' materials. If a realistic material model is used in the theory (say, a model which corresponds to measurements for a realized metamaterial) then the difference between '(natural) material' and 'metamaterial' in fact becomes unimportant. For this reason, in subsequent chapters the terms 'material' and 'metamaterial' may be used interchangeably and the conceptual differences between these two ignored.

A significant portion of the recent work which has involved applying the concept of DNG metamaterials to planar waveguides has utilized transmission line theory [34-36].

Eleftheriades *et al.* [35] have used the model of dielectrics as a distributed network of inductors (L) and capacitors (C) to develop a planar transmission-line-based metamaterial with effective negative material parameters. This design has been implemented and shown to have a negative index of refraction over a fairly wide bandwidth. Figure 1-9 of the previous chapter depicts a unit cell for this design. Additionally, Iyer *et al.* [46] have claimed to have measured focusing in an L-C metamaterial.

Grbic and Eleftheriades [47] have studied, in theory and simulation, evanescent wave enhancement in two-dimensional L-C transmission-line-based metamaterials and found that amplification of evanescent waves is theoretically possible. Further work has been carried out by Eleftheriades *et al.* [48], Grbic and Eleftheriades [49,50] and Iyer *et al.* [51] on refining the understanding of the concepts, implications and applications of these periodically L-C loaded transmission line metamaterials.

Caloz and Itoh [34], in parallel work, have produced a different design, but one which still follows the essential concept of a transmission line model. Further following this work, Ziolkowski and Cheng [52] have studied a design for a DNG-metamaterial-loaded microstrip transmission line for the purposes of modifying propagation characteristics.

Utilizing the research discussed thus far in this area, there have been a variety of investigations into some novel applications of planar DNG waveguides. These have included couplers with unique properties [53,54] and phase shifters [55]. Other work along these lines has also been done, including examination of coupling between waveguides [56] and various effects associated with planar metamaterials, such as refraction and wave focusing [57].

Other guiding structures employing DNG metamaterials, including filled metallic waveguides, have been investigated as well. Caloz *et al.* have used metallic waveguides filled with DNG materials in simulations to verify some of the expected properties of these materials such as positive wave impedance, negative refraction and negative phase velocity [58]. Additionally, Marqués *et al.* have investigated, through simulations, square metallic waveguides loaded with split-ring resonators [59]. They have suggested that the split-ring resonators, in combination with certain aspects of the behavior of metallic

waveguides, yields an effectively DNG load in the guide. Figure 2-3 shows an illustration of the filled waveguide.

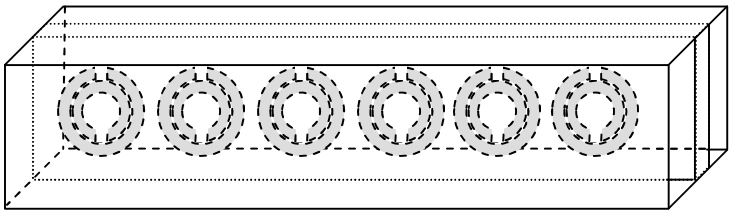


Figure 2-3. A square metallic waveguide filled with periodically placed split-ring resonators.

2.2.1 Dielectric waveguides

There has been a reasonable amount of research in the area of dielectric waveguides containing DNG materials or metamaterials. The first publication on the subject by Shadrivov *et al.* [60] dealt with the simple planar DNG slab waveguide. Many unique and novel results were discovered, including the absence of the fundamental mode, double intra-modal degeneracy and apparent negative group velocity. Other papers further studying the slab have been published as well [61,62]. D'Aguanno *et al.* [63] have examined the double positive (DPS) slab surrounded by DNG claddings. Also, the DNG fiber has been studied by Novitsky and Barkovsky [64]. Nefedov and Tretyakov [65] have studied a two-layer dielectric slab waveguide containing both a DPS and a DNG layer.

Although their work involved both dielectric and metallic waveguides, Alu and Engheta [66] have studied both open and metallic cylindrical waveguides containing combinations of DPS, DNG, negative permittivity and negative permeability coaxial layers. Also, they have studied parallel plate waveguides with pairs of layers of the before mentioned materials [67]. Work has been done by Peacock and Broderick [68] on DNG channel waveguides as well. Halterman *et al.* have studied some characteristics of coupled dielectric slab waveguides [69]: the structure they studied is depicted in Figure 2-4. Shadrivov *et al.* [70] have studied excitation of guided waves in the time domain in multi-layer planar dielectric structures containing DNG materials.

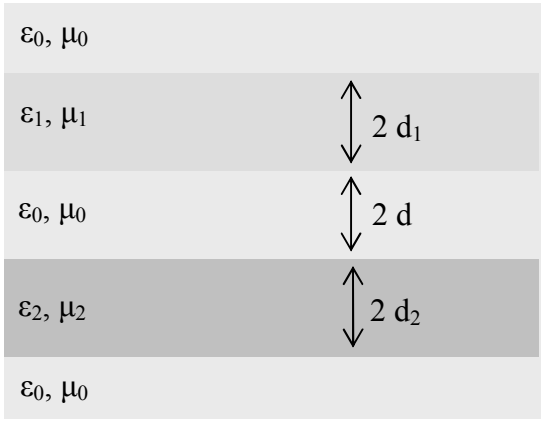


Figure 2-4. Two coupled slab waveguides, each of which may be either DNG or DPS and have frequency-dependent material parameters.

Overall, waveguides seem to be the structures currently most amenable to application of DNG metamaterials. However, given the vast number of possible configurations of waveguides, there are also many possibilities here for future research and for the discovery of new propagation characteristics.

2.3 Scattering by DNG Structures

In addition to guiding and radiating structures, passive DNG material objects also affect fields and waves in their vicinity and thus are of interest. There have been several papers published concerning scattering by DNG objects and structures. These include a study by Lagarkov and Kisel [15] examining plane wave incidence on a circularly cylindrical conductor surrounded by a layer of DNG material. Ruppin has investigated a sphere of DNG material [71].

An area of particular interest has been layered structures including the slab, which as Pendry [6] has argued can act as a perfect lens for an ideal DNG material. Work involving transmission characteristics through multiple-layer DNG structures has also been performed [72-77]. Beyond the before-mentioned articles, not much work in this area has been reported.

2.4 Summary and research motivation

While the present review is not a totally exhaustive listing of all the research that has been undertaken up to this point (in part, no doubt, there are ongoing research projects that have not yet been disclosed), it is representative enough that the general contours of investigation in DNG metamaterials and their applications may be seen fairly clearly. A more thorough review of past work in dielectric (and some DNG-filled metallic) waveguides was presented, as this will be the area of interest for the present investigation.

Given the research that has been done, it appears that waveguides are the most promising area for application of DNG metamaterials. The three-layer (slab) DNG waveguide has been the most extensively studied, and yet questions remain concerning the interpretation of certain aspects of the behavior of this waveguide, including apparently negative group velocity in the guide. Furthermore, this waveguide has been shown to lack the fundamental fast-wave mode [60], a problem which may be dealt with by looking to more complicated geometries. The fundamental mode is useful since its power is focused in the center of the waveguide, whereas higher-order modes have less concentration of power, or even a null, in the center. This characteristic makes the fundamental mode more easily excitable and more efficient in terms of coupling of source power to the waveguide.

Although some multiple-layer structures have been examined lightly [69, 70], N-layer waveguides have not been investigated in detail. Furthermore, the vast majority of the work done thus far has focused on frequency domain analysis, and little has been done to relate the frequency domain results to the time domain through pulse propagation analysis. There is then seen to be a dearth in multiple-layer dielectric waveguide analysis with regard to DNG metamaterials.

It is then the purpose of this investigation to examine N-layer waveguides in detail using frequency domain analysis. The discussion shall begin with a mathematical review of DNG materials, thus providing the necessary basis and understanding upon which an analysis of dielectric waveguides may be built. A generalized formulation for N-layer waveguides shall be presented and used to review the results of the DNG slab

waveguide. However, in addition to reviewing the results already reported in the literature, new results and interpretations shall be given to more fully complete the analysis. The N-layer formulation shall next be used to examine both analytically and numerically the five-layer (or quadruple-clad) DNG waveguide, a configuration which yields many new and interesting results including new modes, certain absent modes, modes out of their expected order and other unique characteristics. Finally, a slight variation on the N-layer formulation shall be used to investigate photonic crystal waveguides containing DNG materials. The emphasis on these waveguides will give a very detailed and thorough account of N-layer waveguides containing DNG materials. Although not every instance of a symmetrically-clad N-layer waveguide will be investigated, the ones presented here will provide a representative sample in terms of the behavior and characteristics of these waveguides. The N-layer formulation may easily be applied, however, to seven-layer or nine-layer (or more) DNG waveguides.

In order to complete the investigation, the frequency-domain results obtained for the N-layer waveguides shall be used to examine pulse propagation. The results from the five-layer waveguide will be used along with Fourier techniques in order to understand pulse propagation in the time domain. This is a matter not treated in the literature and is therefore of great value. The results obtained for this concluding portion of the analysis will support previous interpretations of results and will provide an understanding of the effect of including DNG materials in waveguides on the propagation of a Gaussian pulse.

Although this analysis treats planar dielectric waveguides exclusively, it can be expected that these results will provide a solid outline of the behavior of waveguides based on other coordinate systems, such as the circularly cylindrical dielectric waveguide (fiber). In spite of the fact that the subject of dielectric waveguides has been treated heavily and in depth, the possibility of including DNG materials, which have a host of unique characteristics, demands that the subject be revisited in light of recent developments in this area.

3 Electromagnetic Analysis of DNG Materials

Although double negative (DNG) metamaterials are a relatively new development, it is reasonable to assume that they obey the fundamental tenets of electromagnetic theory that have been so successful in other areas. As such, an analysis of DNG metamaterials may be undertaken with the assumption that their behavior is governed by Maxwell's equations. An investigation and review of basic electromagnetics in DNG materials will facilitate an understanding of the behavior of waveguides containing said materials.

The present mathematical review of DNG materials shall present the very simple case of a monochromatic plane wave incident on an interface. On either side of the interface shall be an arbitrary DNG or DPS medium that is isotropic, linear and homogeneous. This will allow for the derivation of all the requisite mathematical tools for analyzing DNG dielectric waveguides. Issues of dispersion and (concomitantly) loss may be neglected for the present and taken into consideration later in the context of waveguides.

3.1 Monochromatic plane wave incident on an arbitrary semi-infinite material

The present analysis may begin by solving Maxwell's equations for a monochromatic plane wave incident from an arbitrary (DNG or DPS) semi-infinite medium onto another arbitrary semi-infinite medium. This is the simplest case in two dimensions involving the interface of materials. It is noteworthy that arbitrary solutions in the time domain may be constructed by Fourier superposition of monochromatic solutions in the frequency domain. It is assumed that an incoming plane wave, upon incidence, will yield reflected and refracted waves as is typical with conventional materials. Figure 3-1 illustrates the scenario described here. After obtaining general

solutions, these results may be applied to the case where one of the media is a DNG material.

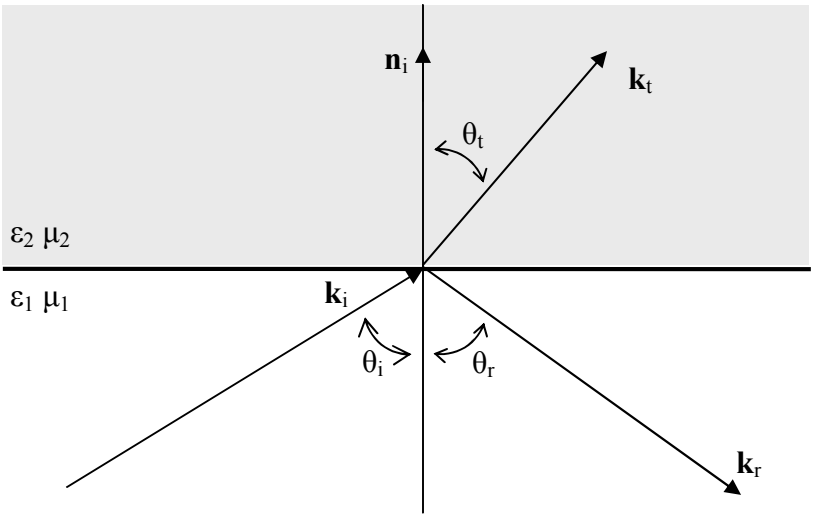


Figure 3-1. Ray diagram of a plane wave ($\mathbf{k}_i$) incident from a semi-infinite medium (ε_1,μ_1) onto another semi-infinite medium (ε_2,μ_2), resulting in reflected ($\mathbf{k}_r$) and (refracted) transmitted ($\mathbf{k}_t$) waves. $\mathbf{n}_i$ is the normal unit vector to the interface.

Maxwell's equations in the time domain for a source-free, non-conducting region are as follows:

$$\nabla \times \mathbf{E}(t) = -\frac{\partial \mathbf{B}(t)}{\partial t} \tag{3-1}$$

$$\nabla \times \mathbf{H}(t) = \frac{\partial \mathbf{D}(t)}{\partial t} \tag{3-2}$$

$$\nabla \cdot \mathbf{D}(t) = 0 \tag{3-3}$$

$$\nabla \cdot \mathbf{B}(t) = 0 \tag{3-4}$$

A monochromatic wave, having sinusoidal time dependence of frequency ω, may be represented as the real part of a corresponding phasor multiplied by $e^{j\omega t}$.

$$\mathbf{E}(t) = \mathrm{Re}\{\mathbf{E}(\omega)\, e^{j\omega t}\} \tag{3-5}$$

$$\mathbf{H}(t) = \mathrm{Re}\{\mathbf{H}(\omega)\, e^{j\omega t}\} \tag{3-6}$$

For simplicity, the only difference between the time domain and frequency domain forms of the fields will be their argument. For the time being, the frequency domain forms will be used exclusively unless explicitly stated otherwise. Substituting (3-5) and (3-6) into Maxwell's curl equations and canceling factors that appear on both sides yields:

$$\nabla \times \mathbf{E}(\omega) = -j\omega \mathbf{B}(\omega) = -j\omega\mu\, \mathbf{H}(\omega) \tag{3-7}$$

$$\nabla \times \mathbf{H}(\omega) = j\omega \mathbf{D}(\omega) = j\omega\varepsilon\, \mathbf{E}(\omega) \tag{3-8}$$

Taking the curl of both sides of (3-7) and (3-8), applying the vector identity involving the definition of the Laplacian operator and then combining the results leads to the Helmholtz wave equation in (3-9). The Helmholtz equation is valid for either **E** or **H** (dropping the angular frequency argument presently).

$$(\nabla^2 + \omega^2 \mu\varepsilon)\begin{Bmatrix}\mathbf{E}\\ \mathbf{H}\end{Bmatrix} = 0 \tag{3-9}$$

It is noteworthy that, thus far, the values of ε and μ are of no consequence to these results. Since both of these values are unaltered from their occurrence in Maxwell's equations, it is appropriate to consider (3-9) to be valid for DNG as well as DPS materials. Introducing k^2, defined as $\omega^2\mu\varepsilon$, yields the following:

$$k = \pm\omega\sqrt{\mu\varepsilon} \tag{3-10}$$

Typically, the positive square root is taken, but the choice of the sign of the square root will be treated later. It will be seen that this is not a trivial matter in the case of DNG materials. The term k is the wave number for a monochromatic wave and may be represented generally as a vector $\mathbf{k} = k\, \mathbf{n}_k$, where $\mathbf{n}_k$ is a unit vector. The solution of (3-9) for a forward-traveling plane wave is as follows, where **r** is the position vector.

$$\mathbf{E} = \mathbf{E}_0 \, e^{-j\mathbf{k}\cdot\mathbf{r}} \tag{3-11}$$

$$\mathbf{H} = \mathbf{H}_0 \, e^{-j\mathbf{k}\cdot\mathbf{r}} \tag{3-12}$$

It can be shown that, for solutions (3-11) and (3-12), the del operator in (3-7) and (3-8) reduces to -j**k**. This implies, upon substitution, that **E**, **H** and **k** form a mutually perpendicular triad with **k** being in the direction of propagation. The plane wave solution is then a transverse electromagnetic wave. These conclusions hold regardless of the medium being DPS or DNG. The wave number k may also be expressed as in (3-13).

$$k = \pm\omega\sqrt{\mu_0 \, \varepsilon_0}\,\sqrt{\mu_r \, \varepsilon_r} = \pm k_0 \sqrt{\mu_r \, \varepsilon_r} = k_0 \, n \tag{3-13}$$

Here, k_0 corresponds to the free space wave number, and n corresponds to the index of refraction which is the square root of the product of the relative permittivity (ε_r) and relative permeability (μ_r) of the medium. ε_0 and μ_0 are the free space permittivity and permeability, respectively. The refractive index n then contains the choice of the square root mentioned previously. A negative choice for the square root would correspond to a negative index of refraction.

Before tackling the issue of the choice of the square root, it is useful to present the time-averaged Poynting vector, **S**, which is given in (3-14). $\mathbf{S}_\omega$ for the monochromatic plane wave is calculated in (3-15).

$$\mathbf{S} = \tfrac{1}{2}\,\mathrm{Re}\left\{\mathbf{E} \times \mathbf{H}^*\right\} \tag{3-14}$$

$$\mathbf{S}_\omega = \tfrac{1}{2}\,\mathrm{Re}\left\{\left|\mathbf{E}_0\right|\left|\mathbf{H}_0\right|^* \frac{\mathbf{k}}{k}\right\} \tag{3-15}$$

Since it is assumed for the purposes of starting with a very simple case that there are no losses in the medium, E_0, H_0 and k are all real. Further, H_0 may be found in terms of E_0 by using (3-8). This yields the following result:

$$\mathbf{S}_\omega = \frac{|\mathbf{E}_0|^2}{2}\frac{\mathbf{k}}{\omega\mu} = \frac{|\mathbf{E}_0|^2}{2\eta}\mathbf{n}_k \tag{3-16}$$

In (3-16), η is defined as follows.

$$\eta = \frac{\omega\mu}{k} = \text{Sign(n) Sign}(\mu)\sqrt{\frac{\mu}{\varepsilon}} \tag{3-17}$$

In (3-17), it is crucial to note the signs involved. Since the square root for the refractive index has not yet been chosen, neither has the sign of the wave impedance, η, been determined. It is useful to note that in a DNG material, Sign(μ) is -1, and therefore the impedance is a positive value if the negative square root is chosen and is a negative value if the positive square root is chosen. In either case, it can be seen in (3-16) that the Poynting vector, $\mathbf{S}_\omega$, will be *necessarily* antiparallel to the wave vector, $\mathbf{k}$ (since $\mathbf{k}$ is in the direction of $\pm\,\mathbf{n}_k$ and $\mathbf{S}_\omega$ is in the direction of $\mp\,\mathbf{n}_k$). Mathematically, then, $\mathbf{S}_\omega \cdot \mathbf{k} < 0$ (or, more generally, $\mathbf{S}_\omega \cdot \text{Re}\{\mathbf{k}\} < 0$). In a DPS material, the positive square root is taken as usual, $\mathbf{k}$ is parallel with $\mathbf{S}_\omega$ and η is positive.

It is useful to determine the reflection and transmission coefficients of a plane wave incident on a material interface in the most general form before finally dealing with the matter of the choice of square root for the refractive index. These coefficients shall be determined by examining the electric field, $\mathbf{E}$. This problem can be divided into two basic cases with regard to polarization: $\mathbf{E}$ perpendicular to the plane of incidence and $\mathbf{E}$ parallel to the plane of incidence. Any arbitrary elliptical polarization may be constructed by superimposing these two polarizations with appropriate magnitudes and phases. Figures 3-2 and 3-3 depict the two cases.

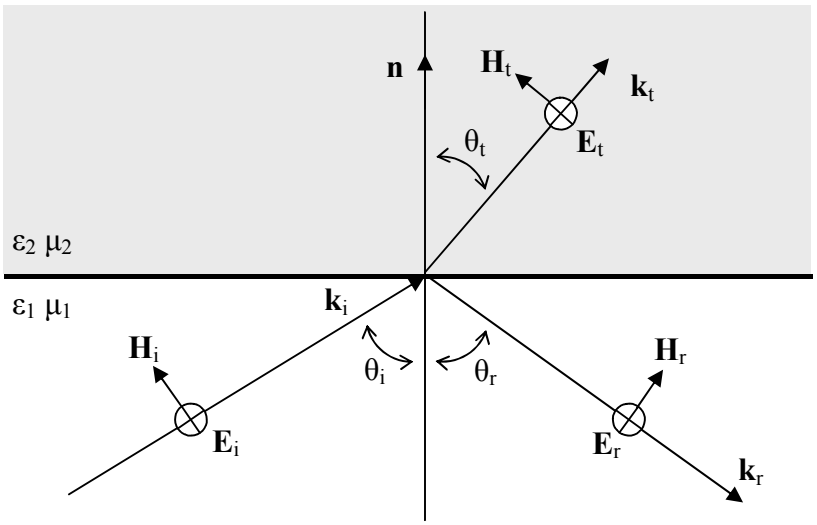


Figure 3-2. The case of E-field perpendicular to the plane of incidence.

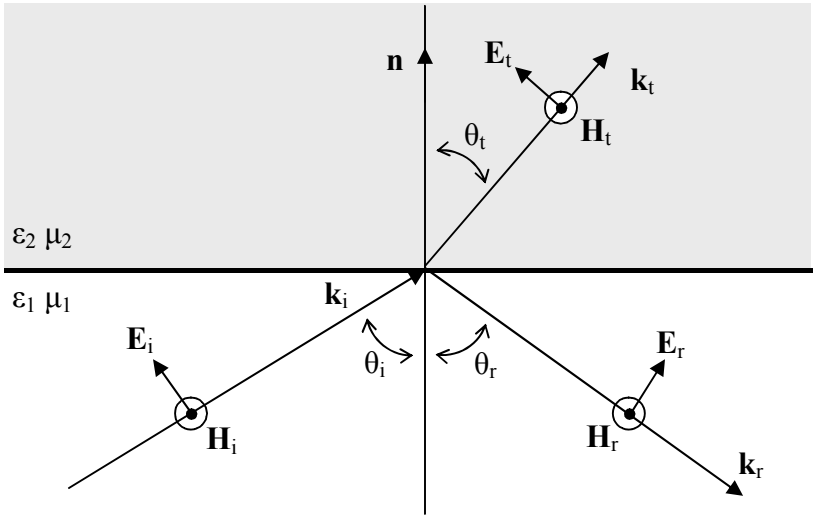


Figure 3-3. The case of E-field parallel to the plane of incidence.

It is appropriate, prior to deriving the transmission and reflection coefficients for the general case of DNG or DPS media, to establish the applicability of the boundary conditions. It is sufficient to show that these boundary conditions follow from Maxwell's equations and that the signs of the permeability and permittivity are inconsequential. Applying Stokes' theorem to (3-7) and (3-8) yields the following, where an arbitrary open surface S is bounded by C:

$$\oint_C \mathbf{E} \cdot \mathbf{dl} = -j\omega \iint_S \mathbf{B} \cdot \mathbf{dS} \tag{3-18}$$

$$\oint_C \mathbf{H} \cdot \mathbf{dl} = j\omega \iint_S \mathbf{D} \cdot \mathbf{dS} \tag{3-19}$$

If a rectangular surface is chosen and situated as shown in Figure 3-4, then as the limit of the length of the sides normal to the material interface goes to zero, the area of S goes to zero. The right hand side of (3-18) becomes zero since there is no flux through a vanishing area, and the left hand side becomes the sum of the tangential components of **E** on either side of the interface (by a line integral) in the limit as their mutual distance from the interface goes to zero. This means that the tangential component of **E** must be continuous across an interface of materials, and this result is irrespective of the signs of μ, ε and k.



Figure 3-4. The area S, centered on the material interface (shown in profile), is bounded by C. **n** is a unit vector normal to the interface.

The result of this argument may also be applied to **H**, yielding similar results from (3-19). Thus, in the source-free case, these boundary conditions may be expressed as follows:

$$\mathbf{n} \times (\mathbf{E}_2 - \mathbf{E}_1) = 0 \tag{3-20}$$

$$\mathbf{n} \times (\mathbf{H}_2 - \mathbf{H}_1) = 0 \tag{3-21}$$

Here, $\mathbf{E}_2$ and $\mathbf{H}_2$ are the fields in medium two (ε_2, μ_2), and $\mathbf{E}_1$ and $\mathbf{H}_1$ are the fields in medium one (ε_1, μ_1), all located at an arbitrary point on the interface.

It remains, then, to determine the boundary condition for the normal component of the fields. By applying the divergence theorem for an arbitrary volume V bounded by

surface S to the frequency domain forms of (3-3) and (3-4), equations (3-22) and (3-23) result.

$$\oiint_S \mathbf{D} \cdot \mathbf{dS} = 0 \tag{3-22}$$

$$\oiint_S \mathbf{B} \cdot \mathbf{dS} = 0 \tag{3-23}$$

By placing an imaginary 'pillbox,' centered on the interface as shown in Figure 3-5, and considering the limit as the height goes to zero, it is found that the normal component of the fluxes **D** and **B** must be continuous across the interface. This results from the fact that the infinitesimal height h of the pillbox precludes any flux through the sides. Although the fluxes themselves involve μ and ε, and therefore the signs come into play, there are no manipulations (such as square roots) which lead to ambiguity.

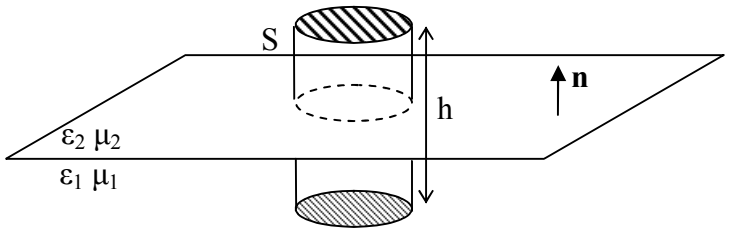


Figure 3-5. The area S is a 'pillbox' of height h centered on the interface. **n** is a unit vector normal to the interface surface.

The boundary condition for the normal component of the fields may be written as follows for the source-free case, noting that $\mathbf{D} = \varepsilon\mathbf{E}$ and $\mathbf{B} = \mu\mathbf{H}$.

$$\mathbf{n} \cdot \left(\varepsilon_2 \mathbf{E}_2 - \varepsilon_1 \mathbf{E}_1\right) = 0 \tag{3-24}$$

$$\mathbf{n} \cdot \left(\mu_2 \mathbf{H}_2 - \mu_1 \mathbf{H}_1\right) = 0 \tag{3-25}$$

It is clear, then, that if Maxwell's equations are assumed to be valid for DNG materials as they are for DPS materials, then all the tools are available for solving the

problem of a plane wave incident on an interface involving DNG materials. The only ambiguity that has thus far arisen is the choice of the square root in the index of refraction. Once the general solution for this problem has been found, the results may be analyzed in the hope of determining which sign corresponds with the physical reality.

It is crucial to determine the relationships among the angles of incidence (θ_i), reflection (θ_r) and refraction (θ_t). These relationships are well-known for DPS materials, but it is important to verify them for arbitrary DPS or DNG materials from first principles. In order for the boundary conditions (3-20), (3-21), (3-24) and (3-25) to be satisfied at all points on the interface and at all times, the spatial and temporal phase of all fields must be equal. This phase matching condition requires that the dot products of the wave vectors and the position vectors be equal at the interface. Mathematically (and recalling (3-11) and (3-12)):

$$\left(\mathbf{k}_i \cdot \mathbf{r}\right)_{\text{Interface}} = \left(\mathbf{k}_r \cdot \mathbf{r}\right)_{\text{Interface}} = \left(\mathbf{k}_t \cdot \mathbf{r}\right)_{\text{Interface}} \tag{3-26}$$

If $\mathbf{r}$ is chosen such that it is parallel to the interface and the plane of incidence, then it follows from (3-26) and Figure 3-1 that:

$$k_i \sin\theta_i = k_r \sin\theta_r = k_t \sin\theta_t \tag{3-27}$$

Since the wave number depends only on the material parameters (as frequency is the same for all waves in this problem) k_i and k_r are equal, and thus it follows from (3-27) that θ_i and θ_r are equal. This is the result regardless of the DNG or DPS status of either medium. Furthermore, it is clear that Snell's law applies with a slight modification for the as yet unchosen sign of the refractive index.

$$\frac{\sin\theta_i}{\sin\theta_t} = \frac{k_t}{k_i} = \frac{n_2}{n_1} \tag{3-28}$$

Here, n_1 and n_2 correspond to the respective indices of refraction in Figure 3-1. The preceding information may then be applied to the problem at hand.

For the case of perpendicular polarization (Figure 3-2), the appropriate boundary conditions may be written as follows, where (3-29) is an application of (3-20), and (3-30) is an application of (3-21) and (3-7). This is simply applying the continuity of the tangential electric and magnetic field components.

$$E_i + E_r = E_t \tag{3-29}$$

$$\frac{1}{\eta_1}(E_i - E_r)\cos\theta_i = \frac{1}{\eta_2} E_t \cos\theta_t \tag{3-30}$$

The transmission coefficient, T, is the ratio of E_t to E_i, and the reflection coefficient, Γ, is the ratio of E_r to E_i. These values may be calculated by algebraically solving (3-29) and (3-30). The results are summarized below.

$$T_\perp = \frac{E_t}{E_i} = \frac{2\eta_2 \cos\theta_i}{\eta_2 \cos\theta_i + \eta_1 \cos\theta_t} \tag{3-31}$$

$$\Gamma_\perp = \frac{E_r}{E_i} = \frac{\eta_2 \cos\theta_i - \eta_1 \cos\theta_t}{\eta_2 \cos\theta_i + \eta_1 \cos\theta_t} \tag{3-32}$$

The angle of refraction may be related to the angle of incidence, without loss of generality, as in (3-33).

$$\cos\theta_t = \sqrt{1 - \frac{n_1^2}{n_2^2}\sin^2\theta_i} \tag{3-33}$$

For normal incidence, the angles of incidence and refraction are zero, and the results in (3-31) and (3-32) reduce to the following well-known representations.

$$T_{\perp\,\text{normal}} = \frac{2\eta_2}{\eta_2 + \eta_1} = 1 + \Gamma \tag{3-34}$$

$$\Gamma_{\perp\,\text{normal}} = \frac{\eta_2 - \eta_1}{\eta_2 + \eta_1} \tag{3-35}$$

The case of parallel polarization (Figure 3-3) may now be treated. The boundary condition for the tangential fields implies the following expressions be valid at the interface:

$$\frac{1}{\eta_1}(E_i + E_r) = \frac{1}{\eta_2} E_t \tag{3-36}$$

$$(E_i - E_r)\cos\theta_i = E_t \cos\theta_t \tag{3-37}$$

Solving (3-36) and (3-37) for T and Γ in the case of parallel polarization yields:

$$T_{\parallel} = \frac{E_t}{E_i} = \frac{2\eta_2 \cos\theta_i}{\eta_1 \cos\theta_i + \eta_2 \cos\theta_t} \tag{3-38}$$

$$\Gamma_{\parallel} = \frac{E_r}{E_i} = \frac{\eta_1 \cos\theta_i - \eta_2 \cos\theta_t}{\eta_1 \cos\theta_i + \eta_2 \cos\theta_t} \tag{3-39}$$

Here, the θ_t and θ_i are once again related through (3-33). These results may be reduced, in the case of normal incidence, to the following, which are slightly different from the case of perpendicular polarization.

$$T_{\parallel \text{normal}} = \frac{2\eta_2}{\eta_2 + \eta_1} = 1 - \Gamma \tag{3-40}$$

$$\Gamma_{\parallel \text{normal}} = \frac{\eta_1 - \eta_2}{\eta_1 + \eta_2} \tag{3-41}$$

It is convenient to determine the Brewster angle, which corresponds to total transmission of the wave, and the critical angle, which corresponds to total reflection of the wave. Finding the Brewster angle involves setting the reflection coefficient, Γ, equal to zero and solving for the incident angle. The Brewster angles are shown below for both the perpendicular and parallel polarizations:

$$\theta_{B\perp} = \sin^{-1}\sqrt{\frac{\frac{\varepsilon_2}{\varepsilon_1} - \frac{\mu_2}{\mu_1}}{\frac{\mu_1}{\mu_2} - \frac{\mu_2}{\mu_1}}} \tag{3-42}$$

$$\theta_{B\parallel} = \sin^{-1}\sqrt{\frac{\frac{\varepsilon_2}{\varepsilon_1} - \frac{\mu_2}{\mu_1}}{\frac{\varepsilon_2}{\varepsilon_1} - \frac{\varepsilon_1}{\varepsilon_2}}} \tag{3-43}$$

These results for the Brewster angle for the general case of DPS or DNG materials are the same as for the specific case of DPS materials only. Obviously, the biggest difference will result from the fact that negative values will be used for the material parameters.

The critical angle is the same for both perpendicular and parallel polarizations and may be written as follows.

$$\theta_C = \sin^{-1}\sqrt{\frac{\mu_2\,\varepsilon_2}{\mu_1\,\varepsilon_1}} \tag{3-44}$$

Any incident angles greater than or equal to the critical angle result in a reflection coefficient of magnitude equal to unity. It is noteworthy that (3-44) may yield a negative angle if exactly one of the media is DNG. In such a case, however, the negative and positive angles are the same (as can be seen by the symmetry of the situation). Additionally, the expression for the reflection coefficient is not affected by negative angles greater than $\pi/4$ due to the presence of cosines and a squared sine term.

These results, then, provide a complete solution to the problem of a plane wave incident from one semi-infinite medium to a second semi-infinite medium, each of which may be arbitrarily a DPS or DNG material running the entire gamut of associated values for μ and ε. The only question that as yet remains unresolved is the choice of the sign for the refractive index. This choice will determine the nature of the wave impedance η in

DNG media; however, it is already well-established that η in a DPS material is positive. It is to this issue that the discussion shall now turn.

3.2 Sign choice for the index of refraction in DNG materials

There have been various arguments in the literature concerning the choice of the sign for the index of refraction in DNG materials, and both sides appear to have legitimate points. It would appear that, based upon experimental observations at least, negative refraction is a reality [4,36,39,46,78]. Additionally, various papers have made the case, by more or less complicated arguments, for the negative square root choice on grounds of causality or other factors [1,12,58,79, *etc*.]. It will suffice for the time being, however, to present a simple argument concerning the Poynting vector, **S**.

If the positive square root is chosen, then the Poynting vector of a plane wave incident from a DPS material onto a DNG material will be towards the interface on both sides of the interface. This results from the fact that the Poynting vector is *always* antiparallel to the wave vector, **k**, in a DNG material. The choice of the negative square root implies that the wave vector in the DNG material will be directed away from the interface. Figure 3-6 shows a comparison of the relevant vectors in this case for each choice of the square root.

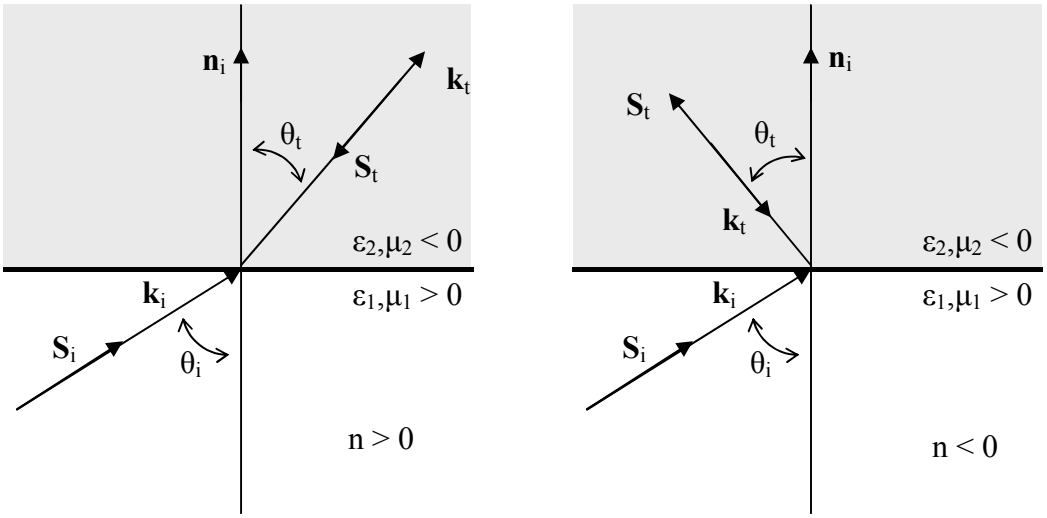


Figure 3-6. Comparison of the implications of a positive index of refraction (left) and a negative index of refraction (right) in a DNG medium. In both cases, a plane wave is incident from a DPS material onto a DNG material.

In the case of a positive index of refraction, as seen in Figure 3-6, all the power is directed (obliquely, perhaps) towards the interface. The results are more dramatic for normal incidence, in which case all power flows directly towards the interface and, apparently, is stored there. The difficulty with this choice is that the DNG medium is source-free (by assumption), and therefore power flowing towards the interface must result in negative energy density throughout the medium. This is, *prima facie*, a non-physical result which must be rejected. Additionally, this difficulty is seen from the fact that a positive choice of the square root results in a negative wave impedance, as dictated by (3-17). On these grounds at least, the positive choice for the square root in the index of refraction must be rejected. For a DNG medium, then, the following simplifications of previous equations result:

$$k_{DNG} = -\omega\sqrt{\mu\varepsilon} \tag{3-45}$$

$$n_{DNG} = -\sqrt{\mu_r \varepsilon_r} \tag{3-46}$$

$$\eta_{DNG} = \sqrt{\frac{\mu}{\varepsilon}} \tag{3-47}$$

These results come from the application of the chosen sign of the square root to (3-10), (3-13) and (3-17). Additionally, it is found as expected that the Poynting vector and wave vector are antiparallel.

$$\mathbf{S}_\omega \cdot \mathbf{k} = \left(\frac{|\mathbf{E}_0|^2}{2} \sqrt{\frac{\varepsilon}{\mu}}\, \mathbf{n}_k \right) \cdot \left(-\omega \sqrt{\mu\,\varepsilon}\, \mathbf{n}_k \right) < 0 \tag{3-48}$$

Probably the most interesting case of an incident plane wave on a material boundary involves a DPS-DNG interface. The above results, with the choice of the square root, may be applied. For a plane wave in a semi-infinite DPS medium incident on a semi-infinite DNG medium (3-31), (3-32), (3-38) and (3-39) are valid as they are. The angle of refraction, θ_t, may be found using (3-28):

$$\theta_t = \sin^{-1}\left(-\sqrt{\frac{\mu_1\,\varepsilon_1}{\mu_2\,\varepsilon_2}} \sin\theta_i \right) = -\sin^{-1}\left(\sqrt{\left|\frac{n_1}{n_2}\right|} \sin\theta_i \right) \tag{3-49}$$

The angle of refraction, in this case, is negative. Figure 3-1 may then be redrawn as Figure 3-7 to illustrate this situation. It can also be seen that if two DNG media meet at an interface, the angle of refraction in (3-49) will be positive as with two DPS media.

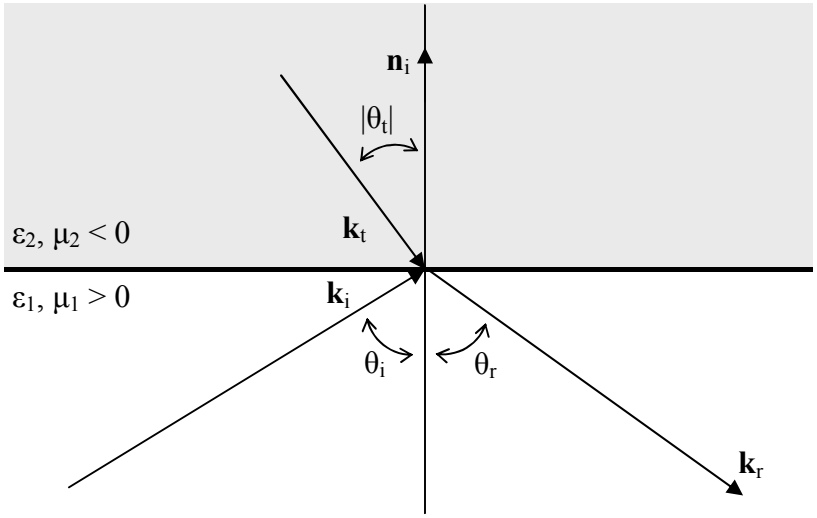


Figure 3-7. An incident plane wave ($\mathbf{k}_i$) from a DPS material refracts negatively in a DNG material ($\mathbf{k}_t$). The reflected wave ($\mathbf{k}_r$) acts as usual.

Additionally, it is noteworthy that the positive wave impedance, η, in a DNG medium means that it is conceivable that a DNG medium may be 'matched' to free space through material parameters that are the negation of the free space parameters. This implies that, ideally, negative refraction of waves may be exploited without reflection due to mismatched media.

4 Planar Dielectric Waveguides Containing DNG Materials

Dielectric waveguides have been widely used in fiber optic communication, electro-optic devices, sensing and instruments used for medical diagnostics. The optical fiber has proven to be an excellent technology for long-distance, large-bandwidth communication. It follows, then, that an investigation into the use of double negative (DNG) materials in dielectric waveguides could possibly yield some interesting, unique results that cannot be obtained using only conventional double positive (DPS) materials. The following discussion shall begin with a rigorous derivation from Maxwell's equations of some useful mathematical tools for the analysis of waveguides. A general formulation for planar waveguides shall be derived and applied to several cases including the three- and five-layer planar dielectric waveguides.

4.1 Mathematical foundations

Since waveguides generally involve at least one linear axis along which waves propagate, it is convenient to express the transverse fields in terms of the component of the fields along this axis of propagation. This may be done by first by recalling Maxwell's curl equations for a monochromatic wave:

$$\nabla \times \mathbf{E} = -j\omega\mu\mathbf{H} \tag{4-1}$$

$$\nabla \times \mathbf{H} = j\omega\varepsilon\mathbf{E} \tag{4-2}$$

The del operator may be broken into the axial and transverse components, where z shall represent the axis of propagation.

$$\nabla = \nabla_t + \mathbf{z}\frac{\partial}{\partial z} \tag{4-3}$$

The transverse del operator ∇_t involves either the partial derivatives with respect to x and y or the partial derivatives with respect to r and φ. These two cases represent, respectively, the Cartesian and cylindrical coordinate systems. The former is useful for such cases as slab waveguides, while the latter is useful for fibers and other circularly cylindrical guides. Other geometries are possible, but these two are the most common. Using (4-3) and expressing the fields as the sum of transverse and axial components, (4-1) and (4-2) yield:

$$\nabla \times \mathbf{E} = (\nabla_t + \mathbf{z}\frac{\partial}{\partial z}) \times (\mathbf{E}_t + \mathbf{z}E_z) \tag{4-4}$$

$$\nabla \times \mathbf{H} = (\nabla_t + \mathbf{z}\frac{\partial}{\partial z}) \times (\mathbf{H}_t + \mathbf{z}H_z) \tag{4-5}$$

If it is assumed that all field solutions have an axial (z) dependence of $e^{-j\beta z}$, where β is the wave number in the guide (or the axial propagation constant), then the partial derivative with respect to z simply becomes -jβ. This form of z-dependence ensures propagation along the z-axis. Expanding (4-4) and (4-5) and eliminating terms of value zero yields:

$$\nabla \times \mathbf{E} = \nabla_t \times \mathbf{E}_t + \nabla_t \times (\mathbf{z}E_z) - j\beta(\mathbf{z} \times \mathbf{E}_t) \tag{4-6}$$

$$\nabla \times \mathbf{H} = \nabla_t \times \mathbf{H}_t + \nabla_t \times (\mathbf{z}H_z) - j\beta(\mathbf{z} \times \mathbf{H}_t) \tag{4-7}$$

By utilizing (4-6) and (4-7) in (4-1) and (4-2) and solving for the transverse component, the following results are obtained:

$$\mathbf{H}_t = \frac{j}{\omega\mu}\left(\nabla_t \times (\mathbf{z}E_z) - j\beta\mathbf{z} \times \mathbf{E}_t\right) \tag{4-8}$$

$$\mathbf{E}_t = -\frac{j}{\omega\varepsilon}\left(\nabla_t \times (\mathbf{z}H_z) - j\beta\mathbf{z} \times \mathbf{H}_t\right) \tag{4-9}$$

Since all fields are assumed to have exponential z-dependence, the $e^{-j\beta z}$ factor may be eliminated for simplicity. The new fields **e** and **h** shall be **E** and **H,** respectively, in which the exponential z-dependence has been dropped. By substituting (4-8) into (4-9) and vice versa, the following two results may be found:

$$\mathbf{h}_t = -\frac{j}{k_0^2 n^2 - \beta^2}(\omega\varepsilon \mathbf{z} \times \nabla e_z + \beta \nabla_t h_z) \tag{4-10}$$

$$\mathbf{e}_t = \frac{j}{k_0^2 n^2 - \beta^2}(\omega\mu \mathbf{z} \times \nabla h_z - \beta \nabla_t e_z) \tag{4-11}$$

Here, k_0 is the free space wave number, defined as $\omega\sqrt{\varepsilon_0 \mu_0}$. The index of refraction, n, is the same as that discussed previously in Chapter 3. These equations are completely general for both DNG and DPS materials as well as for Cartesian or cylindrical coordinate systems. Since the transverse field components are expressed in terms of the fields in the z direction, it suffices to solve any axially uniform waveguide for the z component of the fields only.

Next, the most general form of the wave equation may be found using vector identities. By taking the curl of both sides of (4-1) and (4-2) and combining the results into one expression for simplicity, the following results are obtained:

$$\nabla \times (\nabla \times \begin{Bmatrix} \mathbf{E} \\ \mathbf{H} \end{Bmatrix}) = j\omega \nabla \times \begin{Bmatrix} -\mu \mathbf{H} \\ \varepsilon \mathbf{E} \end{Bmatrix} \tag{4-12}$$

The use of vector/curl identities allows for the simplification of (4-12). For clarity, this form shall be written as two separate equations.

$$\nabla(\nabla \cdot \mathbf{E}) - \nabla^2 \mathbf{E} = -j\omega\left[(\nabla\mu) \times \mathbf{H} + \mu \nabla \times \mathbf{H}\right] \tag{4-13}$$

$$\nabla(\nabla \cdot \mathbf{H}) - \nabla^2 \mathbf{H} = j\omega\left[(\nabla\varepsilon) \times \mathbf{E} + \varepsilon \nabla \times \mathbf{E}\right] \tag{4-14}$$

The first term in each of (4-13) and (4-14) may be rewritten and the curls of the fields may be substituted using (4-1) and (4-2).

$$\nabla\left(\frac{(\nabla\varepsilon)\cdot\mathbf{E}}{\varepsilon}\right)-\nabla^2\mathbf{E}=-j\omega\left[(\nabla\mu)\times\mathbf{H}+j\omega\mu\varepsilon\mathbf{E}\right] \tag{4-15}$$

$$\nabla\left(\frac{(\nabla\mu)\cdot\mathbf{H}}{\mu}\right)-\nabla^2\mathbf{H}=j\omega\left[(\nabla\varepsilon)\times\mathbf{E}-j\omega\mu\varepsilon\mathbf{H}\right] \tag{4-16}$$

Equations (4-15) and (4-16) are the most general form of the wave equation in inhomogeneous media. Although **E** and **H** are not completely decoupled, certain assumptions about the nature of the material parameters in the waveguide usually resolve this difficulty. Further simplifying by the use of (4-3) yields:

$$(\nabla_t^2+k_0^2n^2-\beta^2)\mathbf{E}=\nabla\left(\frac{(\nabla\varepsilon)\cdot\mathbf{E}}{\varepsilon}\right)+j\omega(\nabla\mu)\times\mathbf{H} \tag{4-17}$$

$$(\nabla_t^2+k_0^2n^2-\beta^2)\mathbf{H}=\nabla\left(\frac{(\nabla\mu)\cdot\mathbf{H}}{\mu}\right)-j\omega(\nabla\varepsilon)\times\mathbf{E} \tag{4-18}$$

Based on the above derivations, all the mathematical machinery is in place to begin solving specific problems involving dielectric waveguides.

4.2 Planar dielectric waveguide

The two-dimensional (or planar) dielectric waveguide is the simplest geometry and is the focus of this investigation. Cylindrical geometries, although more mathematically complicated, may be understood to a certain extent by examining the planar geometry, as the solutions are similar. Another simplifying assumption for the planar waveguide is that there is a central core surrounded by some arbitrary number of symmetrically placed cladding layers. The three-layer (or slab) waveguide has been examined [60-63], and the five-layer waveguide has been used in time domain

simulations [70] but has not yet been fully investigated. A general formulation for an N-layer (where N is odd) planar waveguide shall be presented below and the solutions analyzed numerically for several cases. The geometry and parameters of the N-layer waveguide are shown in Cartesian coordinates in Figure 4-1.

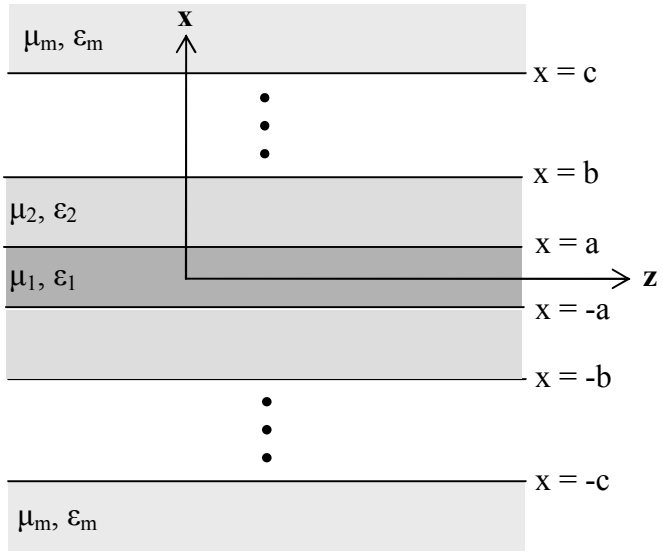


Figure 4-1. Geometry and parameters for a two-dimensional dielectric waveguide with N layers, where $m = {}^{N+1}\!/_{2}$.

In order to solve this problem, it is convenient to first determine the transverse field relations in the Cartesian coordinate system and the wave equation for this configuration. It is important to assume that in each region the material is homogeneous, and therefore the spatial derivatives of the permittivity and permeability become zero. The only thing that remains is to apply the boundary conditions. Additionally, since this is a two-dimensional waveguide, it may be assumed that all quantities are constant in the y direction, and therefore all y derivatives are zero. Then equations (4-10) and (4-11) simplify greatly, and recognizing the following allows for the determination of the individual transverse field components:

$$\nabla_t = \mathbf{x}\frac{\partial}{\partial x} \tag{4-19}$$

The transverse field relations are:

$$\mathbf{h}_t = -\frac{j}{k_0^2 n^2 - \beta^2}\left(\omega\varepsilon \mathbf{y}\frac{\partial e_z}{\partial x} + \beta \mathbf{x}\frac{\partial h_z}{\partial x}\right) \tag{4-20}$$

$$\mathbf{e}_t = \frac{j}{k_0^2 n^2 - \beta^2}\left(\omega\mu \mathbf{y}\frac{\partial h_z}{\partial x} - \beta \mathbf{x}\frac{\partial e_z}{\partial x}\right) \tag{4-21}$$

Separating the vector components yields:

$$h_x = -\frac{j\beta}{k_0^2 n^2 - \beta^2}\frac{\partial h_z}{\partial x} \tag{4-22}$$

$$h_y = -\frac{j\omega\varepsilon}{k_0^2 n^2 - \beta^2}\frac{\partial e_z}{\partial x} \tag{4-23}$$

$$e_x = -\frac{j\beta}{k_0^2 n^2 - \beta^2}\frac{\partial e_z}{\partial x} \tag{4-24}$$

$$e_y = \frac{j\omega\mu}{k_0^2 n^2 - \beta^2}\frac{\partial h_z}{\partial x} \tag{4-25}$$

By examining (4-22) through (4-25) it is seen that independent solutions exist for either h_z or e_z equal to zero. These cases may then be considered separately, and shall be named the transverse electric (TE) and transverse magnetic (TM) modes, respectively. The principle of superposition suggests that these modes can coexist in the same waveguide.

The wave equations (4-17) and (4-18) simplify to the following, where only the z component of the fields is considered:

$$\left(\frac{\partial^2}{\partial x^2} + k_0^2 n^2 - \beta^2\right) e_z = 0 \tag{4-26}$$

$$\left(\frac{\partial^2}{\partial x^2} + k_0^2 n^2 - \beta^2\right) h_z = 0 \tag{4-27}$$

In each case n is the refractive index defined in terms of the relative material parameters:

$$n = \begin{cases} n_1 = \pm\sqrt{\mu_{1r}\,\varepsilon_{1r}} & |x| < a \\ n_2 = \pm\sqrt{\mu_{2r}\,\varepsilon_{2r}} & a < |x| < b \\ \vdots & \vdots \\ n_m = \pm\sqrt{\mu_{mr}\,\varepsilon_{mr}} & |x| > c \end{cases} \tag{4-28}$$

Here, the sign choice depends on whether the particular layer is DNG or DPS. In order to derive a formulation that is general for N layers, it is helpful to define the following quantities, where the normalized propagation constant $\overline{\beta}$ is equal to β / k_0.

$$\nu_i = \begin{cases} 1 & n_i^2 > \overline{\beta}^2 \\ -1 & n_i^2 < \overline{\beta}^2 \end{cases} \tag{4-29}$$

$$q_i = k_0\sqrt{\nu_i\left(n_i^2 - \overline{\beta}^2\right)} \tag{4-30}$$

The subscript i corresponds to the layer of interest and is the same as the subscript for μ and ε for that layer. It is also noteworthy that the solutions to (4-26) and (4-27) are sines and cosines (including hyperbolic) or exponential functions, depending on the sign of the term $k_0^2\, n^2 - \beta^2$. The following functions may be defined as the most general solutions.

$$Z_i(x) = \begin{cases} \sin(x) & n_i^2 > \overline{\beta}^2 \\ \sinh(x) & n_i^2 < \overline{\beta}^2 \end{cases} \tag{4-31}$$

$$\overline{Z}_i(x) = \begin{cases} \cos(x) & n_i^2 > \overline{\beta}^2 \\ \cosh(x) & n_i^2 < \overline{\beta}^2 \end{cases} \tag{4-32}$$

Using the preceding definitions, a general solution to (4-26) and (4-27) may be presented, where ψ_z corresponds to either e_z or h_z as appropriate. Due to the symmetry of the problem, the solution is presented for the half space $x > 0$ only. Field distributions may either be symmetric or anti-symmetric about $x = 0$, corresponding to the so-called 'odd' and 'even' solutions, respectively. The derivatives, which appear in the transverse

field distributions, are symmetric for even solutions and anti-symmetric for odd solutions. In order to impose the physical restriction of finite source energy, the solution must decay to zero as x goes to infinity. This leads to the solution in the outer layer being exponentially decaying. All other layers utilize the functions (4-31) and (4-32).

$$\psi_z(x) = \begin{cases} A_1 Z_1(q_1 x) + B_1 \overline{Z}_1(q_1 x) & x < a \\ A_2 Z_2(q_2 x) + B_2 \overline{Z}_2(q_2 x) & a < x < b \\ \vdots & \vdots \\ A_N e^{-q_N x} & x > z \end{cases} \tag{4-33}$$

For even solutions, B_1 is set to zero while for odd solutions A_1 is set to zero.

The transverse fields may be expressed in terms of the axial field (4-33) by substitution into (4-22) through (4-25).

$$h_{xi} = -\frac{j\beta\nu_i}{q_i} h_{zi}' \tag{4-34}$$

$$h_{yi} = -\frac{j\omega\varepsilon_i\nu_i}{q_i} e_{zi}' \tag{4-35}$$

$$e_{xi} = -\frac{j\beta\nu_i}{q_i} e_{zi}' \tag{4-36}$$

$$e_{yi} = \frac{j\omega\mu_i\nu_i}{q_i} h_{zi}' \tag{4-37}$$

Here, the primed axial fields may be expressed as follows, where the prime on the Z functions represents the total derivative with respect to the argument.

$$\psi_{zi}' = \begin{cases} A_i Z_i'(q_i x) + B_i \overline{Z}_i'(q_i x) & i < \frac{N+1}{2} \\ -A_i e^{-q_i x} & i = \frac{N+1}{2} \end{cases} \tag{4-38}$$

It is emphasized that in (4-33) and (4-38) A_1 is zero for odd modes and B_1 is zero for even modes. These results are completely general and may be applied to any

combination of DPS and/or DNG materials. All that remains is to impose the boundary conditions to determine the field coefficients A_i and B_i and the relationship between the frequency ω and the propagation constant β. This completes the general analysis of N-layer dielectric waveguides, and the investigation shall now turn to specific cases for analytical and numerical analysis.

4.3 Three-layer dielectric waveguide

The simplest case of planar dielectric waveguides is the three-layer (slab) waveguide. In this case, N = 3 and there is only a core region and a cladding region on either side of the core. The geometry is shown in Figure 4-2.

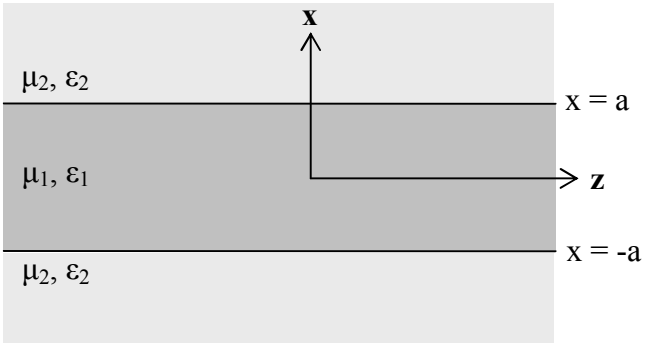


Figure 4-2. The three-layer (slab) waveguide.

The boundary conditions for dielectric waveguides are that the tangential fields at the material interfaces are equal. This process yields expressions for A_1, B_1 and A_2, as well as the so-called characteristic equation which relates the solution β to the frequency ω. The characteristic equation yields a set of discrete curves which are known as modes. These modes each have the feature that the numbers of nodes in the transverse field distributions are always equal for any particular solution in the mode. As mentioned previously, there are both TE and TM solutions, as well as symmetric (even) and anti-symmetric (odd) solutions. This yields four possible combinations: even TE, odd TE, even TM and odd TM. Each of these possibilities has its own unique characteristic

equation and field coefficients. It must again be noted that A_1 is zero for odd modes and B_1 is zero for even modes. Also, it is convenient to define a new function T_i for the purpose of simplifying the expressions.

$$T_i(x) = \begin{cases} \tan(x) & n_i^2 > \overline{\beta}^2 \\ \tanh(x) & n_i^2 < \overline{\beta}^2 \end{cases} \tag{4-39}$$

Also, two new parameters are defined: $U = q_1 a$ and $W = q_2 a$.

4.3.1 Even TE modes

After equating the tangential fields h_z and e_y at x = a, the field coefficients and characteristic equation are determined for the even TE case. These are given below, respectively, where (4-39) is used to simplify the results.

$$A_2 = A_1 Z_1(U) e^W \tag{4-40}$$

$$U T_1(U) = -\frac{\nu_1 \mu_1}{\nu_2 \mu_2} W \tag{4-41}$$

4.3.2 Odd TE modes

The same procedure is applicable to odd TE modes. The expressions for this case are given below.

$$A_2 = B_1 \overline{Z}_1(U) e^W \tag{4-42}$$

$$\frac{U}{T_1(U)} = \frac{\mu_1}{\nu_2 \mu_2} W \tag{4-43}$$

4.3.3 Even TM modes

Similarly, boundary conditions may be applied in the TM case. In this case, the tangential fields e_z and h_y are set equal at x = a. For even TM modes the relevant expressions are listed below.

$$A_2 = A_1 Z_1(U) e^W \tag{4-44}$$

$$U T_1(U) = -\frac{\nu_1 \varepsilon_1}{\nu_2 \varepsilon_2} W \tag{4-45}$$

4.3.4 Odd TM modes

Finally, the expressions for odd TM modes are given below.

$$A_2 = B_1 \bar{Z}_1(U) e^W \tag{4-46}$$

$$\frac{U}{T_1(U)} = \frac{\varepsilon_1}{\nu_2 \varepsilon_2} W \tag{4-47}$$

In review, it can be seen that there are some simple transformation rules which can be applied to these results. That is, in order to go from TE to TM expressions, the substitution $\mu_i \rightarrow \varepsilon_i$ for all i is required. The transformation from even to odd modes requires $T_1(U) \rightarrow -\upsilon_1/T_1(U)$. (It is noteworthy that $\upsilon_i = 1/\upsilon_i$.) The reverse transformations also are valid. Also, it may be seen that these results continue to be valid regardless of the nature of the materials used, whether they be DNG or DPS. No ambiguities have yet arisen. Consequently, all the necessary information has been acquired for the numerical analysis of the slab waveguide.

4.3.5 Limits on the propagation constant β

It may be shown that, whether DNG or DPS materials are used, the propagation constant β may not assume any value without restriction. This is seen by examining

several cases, which shall be looked at in light of even TE modes but are similar for odd and TM modes as well. For convenience, it is necessary to examine a slightly different formulation for the characteristic equations. This involves solving (4-26) and (4-27) without dividing the problem by cases (*i.e.*, by the relationship of n_i and $\overline{\beta}$). For this approach, ψ_z is shown below, where q_i is also defined.

$$\psi_z = \begin{cases} A_1 \sin(q_1 x) + B_1 \cos(q_1 x) \\ A_2 e^{-q_2 x} \end{cases} \tag{4-48}$$

$$q_i = k_0 \sqrt{n_i^2 - \overline{\beta}^2} \tag{4-49}$$

Again, for odd modes A_1 is equal to zero and for even modes B_1 is equal to zero. Applying (4-22) through (4-25), the characteristic equations may be found for this formulation by setting the tangential fields (y- and z-directed fields, respectively) equal at x = a. For the even TE case, this yields the equation below, where $U = q_1 a$, $W = q_2 a$, and q_i is defined by (4-49).

$$U \tan U = \frac{\mu_1}{\mu_2} W \tag{4-50}$$

Several cases may now be examined for the relative value $\overline{\beta}$. The first case is for $\overline{\beta}^2 < n_2^2$. In this case, $W = j\hat{W}$ where $\hat{W} = \hat{q}_2 a$ and $\hat{q}_i$ is defined below.

$$\hat{q}_i = k_0 \sqrt{\overline{\beta}^2 - n_i^2} \tag{4-51}$$

If $\overline{\beta}^2 < n_1^2$, U tan U remains unchanged, but if $\overline{\beta}^2 > n_1^2$ U tan U becomes $-\hat{U} \tanh \hat{U}$. In either case, the left-hand side of (4-50) is purely real while the right-hand side is purely imaginary (in the lossless case). As a result, there is no real solution to (4-50) when $\overline{\beta}^2 < n_2^2$ and therefore no propagating modes. It may then be stated generally that

for propagating modes $\bar{\beta}^2 > n_2^2$. This is true regardless of the DNG/DPS composition of the waveguide.

The other case of interest involves $\bar{\beta}^2 > n_1^2$. As mentioned previously, the left-hand side of (4-50) becomes $-\hat{U}\tanh\hat{U}$. Since $\hat{U}$ is positive, and therefore the left-hand side of (4-50) is negative, real solutions only exist when the right-hand side is also negative. Since W is positive, however, there can only be a real (propagating) solution when exactly one of the permeabilities μ_1 and μ_2 is negative. This only occurs, in the context of this investigation, when exactly one of the materials in the waveguide is DNG. If both are DNG or both DPS then $\bar{\beta}^2 < n_1^2$. Otherwise, the only restriction on the solutions is that $\bar{\beta}^2 < n_2^2$. These restrictions may then be applied to the previous general formulation.

One other item of interest is that the propagation constant β (and, consequently, $\bar{\beta}$) only appears in the characteristic equation as a squared term. As a result, both $+\beta$ and $-\beta$ are mathematically valid solutions. The choice of the appropriate sign must take into consideration the physical constraints of the problem. At this point, it is helpful to introduce phase velocity (v_p) and group velocity (v_g). These are defined below.

$$v_p = \frac{\omega}{\beta} \tag{4-52}$$

$$v_g = \frac{\partial\omega}{\partial\beta} = \left(\frac{\partial\beta}{\partial\omega}\right)^{-1} \tag{4-53}$$

It may be shown that the group velocity is equivalent to the energy velocity in the lossless case [80]. Although the phase velocity may be positive or negative without any apparent physical implications, the energy velocity must be directed away from the source. If it is assumed that there is only one source in the waveguide, located at $z = -\infty$ (or in the negative axial direction), then the energy velocity must be in the positive z-direction. This implies that (4-53) must be positive, since energy must travel away from the source in light of the fact that no reflecting mechanism exists in the uniform, lossless waveguide.

Also, it may be noted that for DPS waveguides the magnitude of the propagation constant β is always less than the magnitude of n_1, and therefore the phase velocity is always greater in the waveguide than it would be in an infinite space of material with refractive index n_1. These are the so-called 'fast-wave' solutions [60]. On the other hand, for DNG waveguides there is no such restriction on β, and therefore the magnitude of β may exceed the magnitude of both n_1 and n_2. This implies that the phase velocity of a solution in the slab may in fact be less than that in an infinite space of either material. These are 'slow-wave' solutions [60]. For DPS waveguides, then, only fast-wave modes exist, while for DNG waveguides both fast-wave and slow-wave modes are allowed.

4.4 Cutoff conditions

Also of interest are the cutoff conditions for the modes in a slab waveguide, which describe the frequencies above or below which the mode may exist. In the general case which includes both DPS and DNG waveguides, two sets of cutoff conditions exist: one for fast-wave modes and one for slow-wave modes. The cutoff condition for fast-wave modes is that $\overline{\beta}$ goes to n_2. For slow-wave modes, the condition is that $\overline{\beta}$ goes to n_1. By applying these to the characteristic equations, new expressions result which can be used to calculate the frequencies of interest. It is helpful to define the normalized frequency V in the most general case.

$$V = k_0 a \sqrt{\left| n_1^2 - n_2^2 \right|} \tag{4-54}$$

4.4.1 Fast-wave modes

For even fast-wave modes, W becomes zero and the following cutoff expression applies to both the TE and TM cases:

$$\tan V = 0 \tag{4-55}$$

For this condition, the tangent function has infinite zeroes, corresponding to an infinite number of possible even modes at V equal to integer multiples of π.

For odd fast-wave modes, a similar analysis yields the following:

$$\cot V = 0 \tag{4-56}$$

In this case, there are also an infinite number of solutions corresponding to an infinite number of possible odd modes. These solutions occur at V equal to integer multiples of π/2.

4.4.2 Slow-wave modes

For slow-wave modes, the cutoff condition requires that U go to zero. When treated carefully, this leads to the following for even modes:

$$\omega\sqrt{n_1^2 - n_2^2} = 0 \tag{4-57}$$

This expression means that there can be at most two solutions: one for ω = 0 and one for $n_1^2 = n_2^2$. Typically, however, this will mean that there is only one allowable solution (as the DNG range seldom includes zero frequency).

For odd TE and odd TM modes, the following expressions apply respectively, where c is the speed of light in vacuum:

$$\omega\sqrt{n_1^2 - n_2^2} = -\frac{\mu_2}{\mu_1}c \tag{4-58}$$

$$\omega\sqrt{n_1^2 - n_2^2} = -\frac{\varepsilon_2}{\varepsilon_1}c \tag{4-59}$$

These expressions are slightly more obtuse, and specific information about the number of possible solutions is difficult to obtain without knowing precisely the material models being used. However, these are useful for determining cutoff frequencies. The right-hand side of both (4-58) and (4-59) is positive, and since slow-wave modes only exist for the case of one DNG and one DPS material, these equations do in fact have solutions.

4.5 Numerical analysis of a DPS waveguide

Now that a complete analytical solution has been given for the three-layer (slab) dielectric waveguide, numerical results may be calculated for specific cases. It is helpful, before looking at cases which include DNG materials, to examine a typical case with DPS materials only. This may be done by using two normalized parameters, b and V. The normalized propagation constant b and a simplified version of the normalized frequency V are defined below, noting that $\upsilon_1 = 1$ and $\upsilon_2 = -1$.

$$b = \frac{\overline{\beta}^2 - n_2^2}{n_1^2 - n_2^2} \tag{4-60}$$

$$V = \sqrt{U^2 + W^2} = k_0 a \sqrt{n_1^2 - n_2^2} \tag{4-61}$$

For DPS materials, b ranges from zero to unity, and V is proportional to the frequency ω. The characteristic equations may be solved numerically and the results plotted as seen in Figure 4-3 for TE modes. The dispersion characteristics for TM modes are similar. Modes are labeled according to the number of nodes in their transverse field distributions. This method of mode classification gives TE_0, TE_1, TE_2 *etc*. Similar classification applies to TM modes. The results in Figure 4-3 give a general illustration of the modal behavior of the DPS slab waveguide.

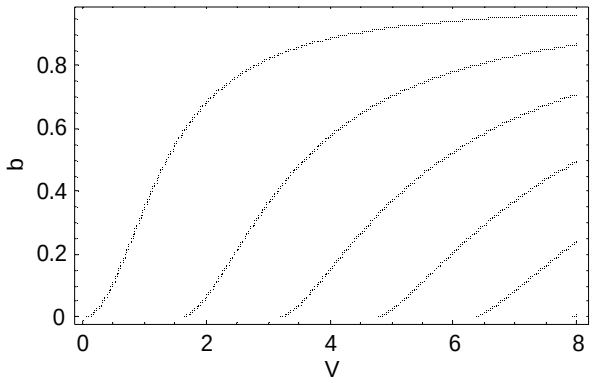


Figure 4-3. The TE dispersion characteristics for a simple slab waveguide. Both even and odd modes are shown, where starting from the left the modes are designated TE_0, TE_1, TE_2, etc.

Also of interest are the field distributions in the guide. These are shown in Figure 4-4 for the first TE mode (TE_0, an even mode) at a normalized frequency V = 2.21.

These numerical results provide a general understanding of the behavior of guided modes in DPS waveguides. Of interest to this investigation are DNG waveguides, to which the discussion will now turn.

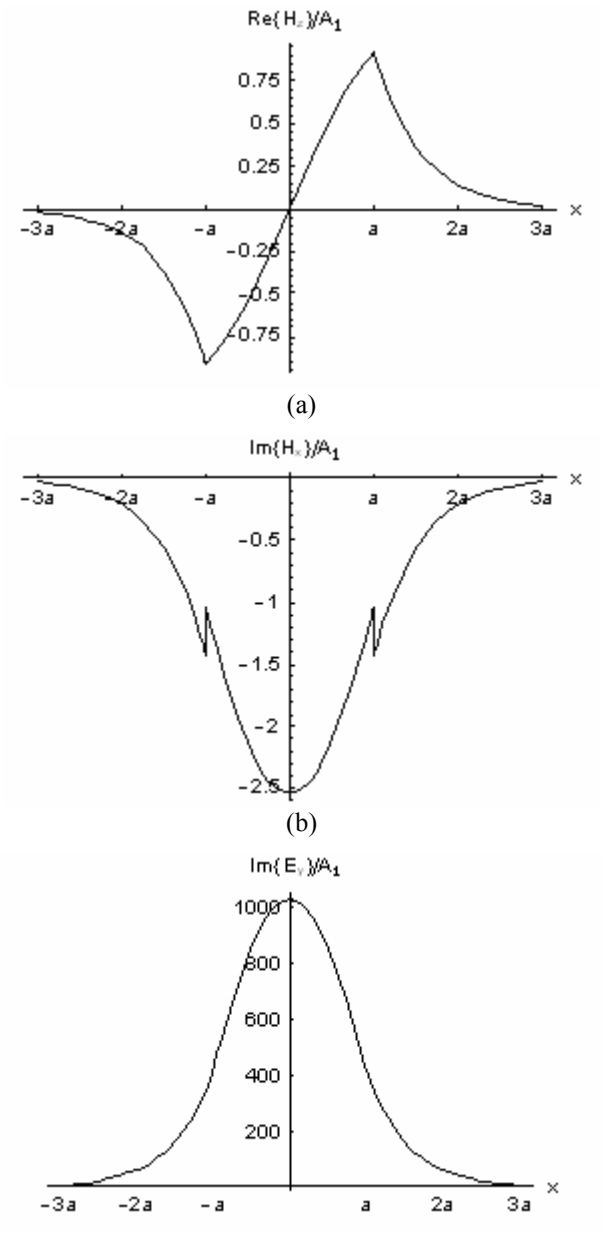


Figure 4-4. Normalized field distributions for the TE_0 mode at a normalized frequency of V = 2.21. The factor A_1 is the initial amplitude of the z-component of the magnetic field, and *a* is half the width of the slab.

4.6 DNG material models

Since DNG materials are inherently dispersive [1], it behooves the investigation to consider appropriate material models such that the results obtained are realistic. One

possible approach is to use a model based on measurements of an actual metamaterial. Although other materials may be developed, or may already exist, which have better characteristics, the use of a known metamaterial model allows for the presentation of results which are firmly based in reality.

Dispersion and loss are related by the Kramers-Kronig relationships, and therefore DNG materials are also inherently lossy. This complicates the analysis, as an exact solution to the problem involves finding complex propagation constants. However, if the loss is sufficiently small (*i.e.*, if the imaginary parts of the material parameters are small compared to the real parts) then the problem may be solved for the lossless case and loss may be considered via perturbation theory.

Shadrivov *et al*. [60] used the following DNG material parameter functional forms in their analysis of the slab waveguide:

$$\varepsilon_r(\omega) = 1 - \frac{\omega_p^2}{\omega^2} \tag{4-62}$$

$$\mu_r(\omega) = 1 - \frac{F\omega^2}{\omega^2 - \omega_0^2} \tag{4-63}$$

These forms correspond to a model of the metamaterial developed by Smith *et al.* [2]. Specifically, the relative permeability in (4-63) is essentially the analytical model expounded by Pendry *et al.* [19], less the part involving losses. The permittivity in (4-62) is a Drude model which suffices for structures involving three-dimensional wire grids. The terms ω_p, ω_0 and F are determined by the specific geometry and dimensions of the constituent elements in the metamaterial. A slight modification to (4-63), ignoring loss for the moment, is used by Smith and Kroll [3]:

$$\mu_r(\omega) = 1 - \frac{F\omega_0^2}{\omega^2 - \omega_0^2} \tag{4-64}$$

This ensures the physical requirement that as the frequency goes to infinity, the permeability approaches unity. An even more realistic model includes the aspect of loss,

such as the following model which is available in the literature. This model is a very symmetric set of material parameter forms:

$$\varepsilon_r(\omega) = 1 - \frac{\omega_{ep}^2 - \omega_{eo}^2}{\omega^2 - \omega_{eo}^2 - j\gamma\omega} \tag{4-65}$$

$$\mu_r(\omega) = 1 - \frac{\omega_{mp}^2 - \omega_{mo}^2}{\omega^2 - \omega_{mo}^2 - j\gamma\omega} \tag{4-66}$$

Specific values for the parameters in these forms are given in [4] and [5] for models of actual metamaterials.

The model defined by (4-65) and (4-66), along with the moderately low-loss parameters from [4], will be used to analyze waveguide configurations with loss as well as dispersion. These parameters are f_{ep} = 12.8 GHz, f_{eo} = 10.3 GHz, f_{mp} = 10.95 GHz, f_{m0} = 10.05 GHz and γ = 10 MHz. Multiplying the frequencies f by 2π gives the angular frequencies ω. The real and imaginary parts of these material parameters are plotted below in Figures 4-5a and 4-5b, where:

$$\varepsilon_r = \frac{\varepsilon}{\varepsilon_0} = \varepsilon_r' - j\varepsilon_r'' \tag{4-67}$$

$$\mu_r = \frac{\mu}{\mu_0} = \mu_r' - j\mu_r'' \tag{4-68}$$

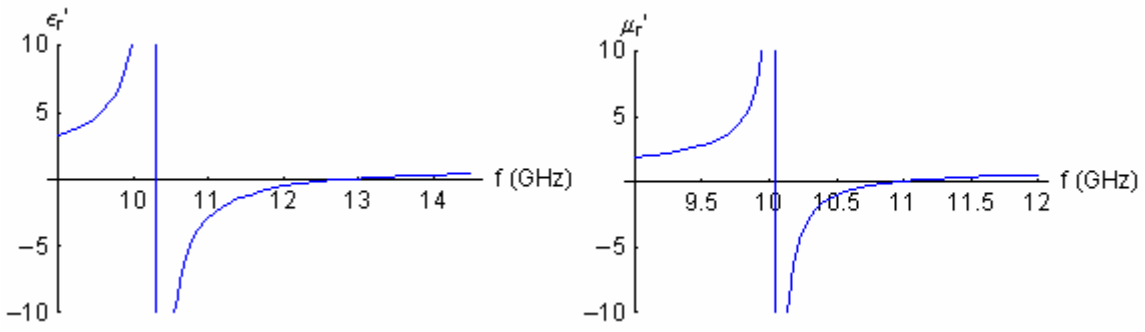
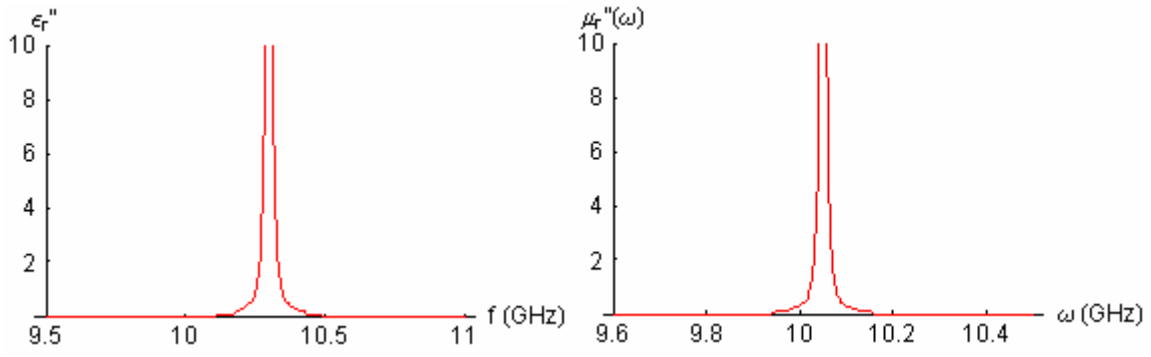


Figure 4-5a. The material parameters ε_r' (left) and μ_r' (right) as a function of frequency f.



(1) (2)

Figure 4-5b. The material parameters ε_r'' (left) and μ_r'' (right) as a function of frequency f.

As can be seen from the above, this DNG metamaterial is highly lossy near the resonance and, in fact, only maintains its DNG characteristics over a small bandwidth, approximately 10.3 to 10.95 GHz in this case. Although this severely limits the useful range of frequencies, it is possible to get a sense of what is happening by examining even this small bandwidth. In order for a perturbation approach of loss evaluation to be acceptable, the imaginary parts of the material parameters must be small compared to the real parts. This limits the perturbation method to frequencies in the middle of the DNG band. The ratios of the real to imaginary parts of the material parameters are plotted in Figure 4-6. This gives an indication as to the frequency range over which the perturbation method is appropriate.

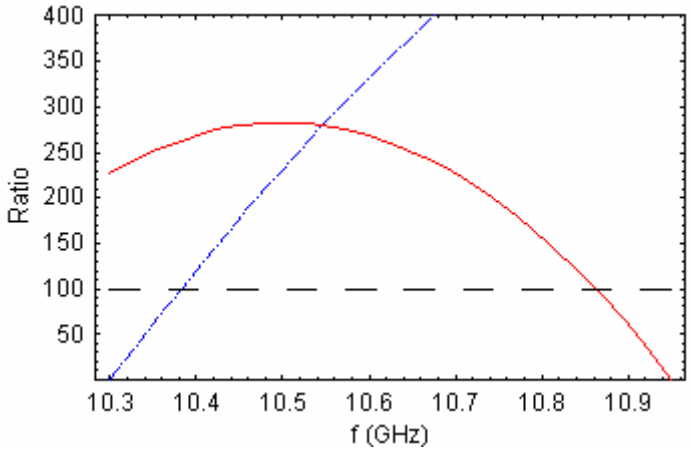


Figure 4-6. The ratio of ε_r'/ ε_r" (dot-dashed blue) and μ_r'/ μ_r" (solid red). The level of 100 is marked with the broken line as an approximate reference above which the perturbation method is valid.

Only about ¾ of the DNG band can be analyzed using the perturbation method, assuming that the real material parameter component must be at least 100 times the imaginary component. Some leeway may be available, however, depending on the accuracy of the results. The analysis of the waveguide at specific frequencies, in terms of such things as solutions and field distributions, is the same as above when using the perturbation method. The only added factor is calculating the effect of loss, which shall be treated next.

4.7 Calculation of Loss

Attenuation for low-loss materials may be calculated using a perturbation method, which simply assumes that losses will not have a significant impact on the rest of the analysis. Therefore, for the range of frequencies for which the real part of the material parameters are much larger than the imaginary part, a loss-free analysis may be undertaken for the waveguide containing the material, after which time the losses may be calculated separately. The approach generally follows that outlined in [80] for lossy transmission lines. The other option is an exact calculation, which is more difficult but helpful in verifying the results of the perturbation method.

The attenuation coefficient α, together with the propagation constant β, forms the complex propagation constant γ given below.

$$\gamma = \alpha + j\beta \tag{4-69}$$

The total power flow along the guide is proportional to an exponential factor, $e^{-2\alpha z}$, where the number 2 results from the power being related to the square of the fields. Then the rate of power loss along the guide is as follows:

$$P_l = -\frac{\partial P}{\partial z} = 2\alpha P_0 e^{-2\alpha z} = 2\alpha P \tag{4-70}$$

Here, P_0 is the initial power at z = 0, and P_l is the power loss rate. So, the attenuation constant is given below:

$$\alpha = \frac{P_l}{2P} \tag{4-71}$$

The specific form of α may be found by using the time-harmonic Poynting theorem in a source-free environment [81], where here only the real parts are considered.

$$-\mathrm{Re}\left\{\int_S \mathbf{E}\times\mathbf{H}^*\cdot\mathbf{dS}\right\} = \omega\int_v\left(\varepsilon''|\mathbf{E}|^2 + \mu''|\mathbf{H}|^2\right)dv \tag{4-72}$$

S is, in this case, the cross section of the waveguide. Since it is known that the power dependence along the z-direction is exponential, as in (4-70), then the z-component of the volume integral in (4-72) may be taken independently.

$$\omega\int_v\left(\varepsilon''|\mathbf{E}|^2 + \mu''|\mathbf{H}|^2\right)dv = \omega\int_S\left(\varepsilon''|\mathbf{E}|^2 + \mu''|\mathbf{H}|^2\right)dS\int e^{-2\alpha z}dz \tag{4-73}$$

The integral for the z-component is cast in terms of a per-unit-distance form. Evaluating this integral and then performing some algebra, (4-71) is expressed fully in terms of the fields in the guide.

$$\alpha = \frac{1}{2}\frac{\omega\int_S\left(\mu''|\mathbf{H}|^2 + \varepsilon''|\mathbf{E}|^2\right)dS}{\mathrm{Re}\int_S \mathbf{E}\times\mathbf{H}^*\cdot\mathbf{dS}} = \frac{P_l}{2P} \tag{4-74}$$

This result allows for the calculation of losses based on the known fields **E** and **H**. Here, the requirement that the fields must not be affected appreciably by loss is clearly seen, thus justifying the assumption that the imaginary (loss) part of the material parameters be much less than the real part in order for the perturbation method to be applicable.

The exact formulation simply involves finding the complex roots of the characteristic equation when complex material parameters are used. If an exponential

loss is assumed, then this exact formulation may be obtained simply by converting the z-dependence of the fields from $e^{-j\beta z}$ to $e^{-\gamma z}$. It can be seen here that for this conversion β becomes $-j\gamma$. Then, if the characteristic equations are solved as they are with the only difference being that the complex forms of the permittivity and permeability are used, the solution $\overline{\beta}_{solution}$ may be converted to γ by the following algebraic manipulation.

$$\gamma = -jk_0\overline{\beta}_{solution} = -jk_0\left(\overline{\beta} - j\overline{\alpha}\right) = \alpha + j\beta \tag{4-75}$$

This allows for finding the exact solution of the characteristic equation in the presence of loss. The actual process of finding the solution must be done numerically and is not a simple matter. *Mathematica* employs a complex root search algorithm which usually converges to the appropriate solution, although avoidance of spurious solutions is by no means trivial or guaranteed. Regardless of that shortcoming, this allows for a sufficient confirmation of the perturbation method. All the mathematical machinery is then in place to analyze dispersive, lossy DNG waveguides.

4.8 Solutions for a DNG slab

Although the characteristic equations (4-41), (4-43), (4-45) and (4-47) have no real solutions when $\overline{\beta}^2 > n_1^2$ for DPS materials, when a DNG material is used in the core real solutions become available. In the case of these solutions, the propagation constant β is larger than the free-space wave number for the slab material. As a result, these solutions have a phase velocity smaller than that of an infinite medium of the slab material and are therefore called 'slow-wave' solutions [60]. Using the material model (4-65) and (4-66) whose characteristics are plotted in Figures 4-5a and 4-5b, the dispersion characteristics for a DNG slab waveguide may be plotted. These results are shown in Figures 4-7 and 4-8 for a waveguide with a = 2.5mm, $\mu_2 = \mu_0$, $\varepsilon_2 = \varepsilon_0$ and with μ_1 and ε_1 governed by the before-mentioned material model. In this case, however, loss

is considered negligible and is thus ignored. It shall be considered later as a perturbation of the lossless results.

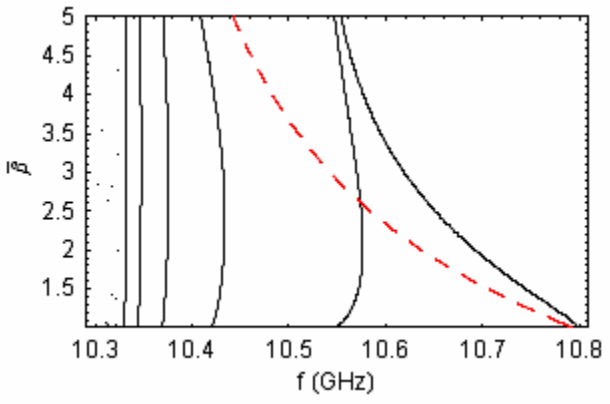


Figure 4-7. The TE dispersion characteristics of a DNG slab waveguide (solid black). The absolute value of n_1 (dashed red) is also plotted for reference. Modes below approximately 10.33 GHz are segmented or unseen due to limited numerical sampling and an infinite density of modes in the neighborhood of 10.3 GHz.

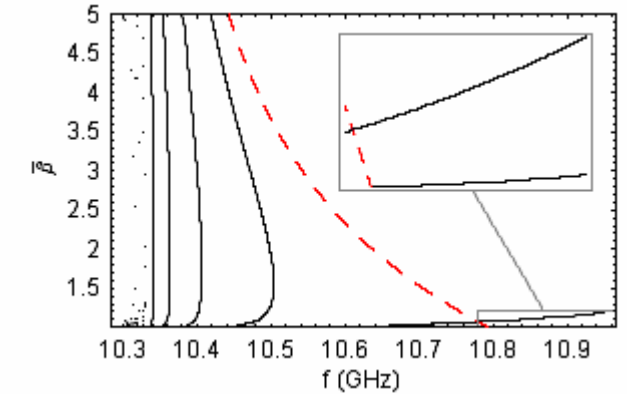


Figure 4-8. The TM dispersion characteristics of a DNG slab waveguide (solid black). The absolute value of n_1 (dashed red) is plotted for reference. A close-up of the lower right-hand portion of the plot is inset. Modes below approximately 10.33 GHz are segmented or unseen due to limited numerical sampling and an infinite density of modes in the neighborhood of 10.3 GHz.

These results present several interesting properties. The solutions are shown only over the DNG range of 10.3 to 10.95 GHz. The modes are in fact 'reversed' in order from conventional waveguides, with the fundamental mode being the right-most (highest frequency) mode and higher-order modes appearing as the frequency decreases. This is due to the fact that n_1 is decreasing with increasing frequency. Also, since n_1 goes to infinity at 10.3 GHz, the density of modes increases as this frequency is approached.

There are an infinite number of modes at the lower-frequency end of the DNG range. Also, double intramodal degeneracy is seen for most of the modes.

The cutoffs for the slow-wave modes are as expected. The TE_0 and TM_0 slow-wave modes both have cutoffs at $n_1^2 = n_2^2 = 1$. The cutoffs for the higher-order slow wave modes (TE_1 and TM_1) are both at slightly lower frequencies. These are the only slow-wave modes. It is also noteworthy that the fundamental modes are purely slow-wave, while the TE_1 and TM_1 modes are a mixture of slow-wave and fast-wave solutions. All other higher-order modes are purely fast-wave. Furthermore, as can be seen by examining the cutoff conditions in Section 4.4 and the above results, the fundamental fast-wave mode is always absent for the three-layer DNG waveguide. This may be further proven by virtue of the fact that for a DNG slab the right-hand sides of (4-41) and (4-45) are negative. As a result, the only available solutions for U are greater than $\pi/2$, but this excludes the fundamental mode which requires $0 \leq U \leq \pi/2$. This disturbs the typical hierarchy of fast-wave modes which are seen in conventional waveguides. The slow-wave modal hierarchy includes only the zeroth and first (fundamental and first-order) modes. It is also seen in the plots that the slow-wave modes may have arbitrarily small phase velocities.

Also of interest are the field distributions for this waveguide. Shown in Figure 4-9 are the fields for the fundamental TE_0 mode at 10.7 GHz as shown in Figure 4-7. These plots reveal some distinct differences from the DPS field distributions of Figure 4-4. One of the most conspicuous distinctions is the huge discontinuity in plot (b). This results from the change of sign of the material parameters μ and ε from the slab to the cladding layers. Also, rather than having energy focused in the center of the guide in the transverse field distributions ((b) and (c)), the energy is rather focused at the interfaces of the slab and the cladding layers. This suggests that slow-wave propagating modes act more as surface waves in the waveguide.

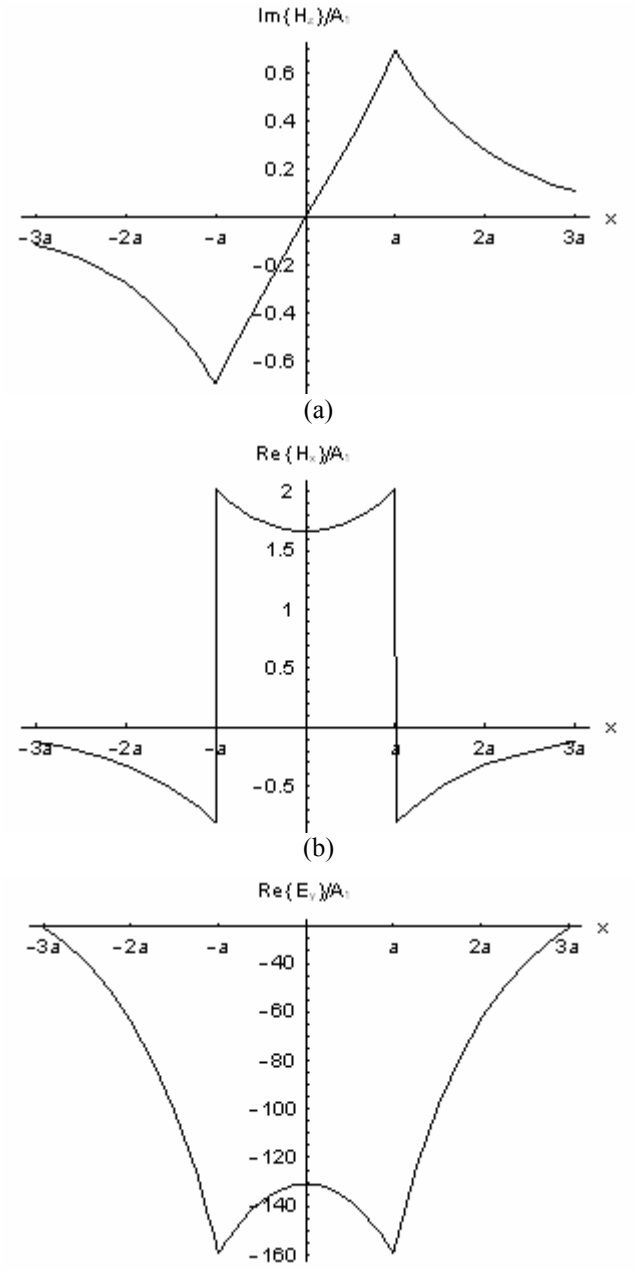


Figure 4-9. Normalized field distributions for the TE_0 mode of a DNG slab waveguide at a frequency of f = 10.7 GHz. The factor A_1 is the initial amplitude of the z-component of the magnetic field, and *a* is half the width of the slab.

4.8.1 Group and phase velocities

It must further be noted that the above plots are for the absolute value of $\overline{\beta}$, but both the negative and positive values are mathematically acceptable solutions to the characteristic equations. With DPS-only waveguides, the positive values of $\overline{\beta}$ were chosen since this choice ensured that the energy velocity v_e was always positive and thus away from the source. A similar approach may be taken in this case, albeit with different results.

It was seen in Chapter 3 that plane waves in DNG materials display a negative phase velocity but positive energy velocity. It is therefore not unthinkable that such a phenomenon could occur in a DNG waveguide as well. Since the problem is being considered in the lossless case, the energy velocity and group velocity are identical in the waveguide. Furthermore, there is nothing in the problem that would allow for reflection of energy, and therefore, in order to have a causal solution, energy must be directed away from the source. For this analysis, the source is considered to be at $z = -\infty$ (or at some distance to the left of the waveguide). As a result, guided energy must travel in the right (positive z) direction. This would require that only positive slopes for β versus ω be allowable, since positive slope corresponds to positive energy velocity. Hence, any mathematical solutions which have a negative slope (energy velocity) must be discarded as non-causal solutions, since there is no energy source from which negative z-directed waves may originate. Figure 4-10 illustrates this by showing all the mathematically valid solutions to the even TE characteristic equation with the causally valid ones as solid lines and the non-causal ones as dashed lines. Only several modes are shown, but the same principle applies to all modes. The waveguide parameters are the same as those for the preceding two figures.

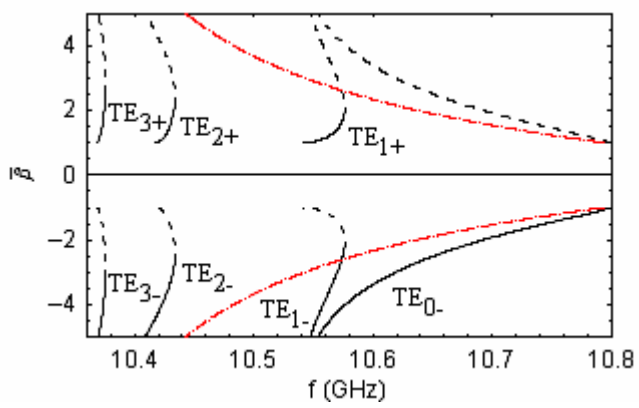


Figure 4-10. The actual TE dispersion characteristics for a DNG waveguide. The causally valid solutions (solid black) and the causally invalid solutions (dashed black) are both shown. Both positive and negative values of n_1 (dot-dashed red) are plotted for reference.

Although β has not been used in the above plot, it is sufficient to examine $\bar{\beta}$ since the "turning point," where the modes go from negative to positive slope (or vice versa), is the same for both the β versus ω plot and the $\bar{\beta}$ versus ω plot. Also, a new notation for classifying the modes has been used in the figure. Since both the positive and negative solutions of the mode propagation constant yield the same number of nodes in the transverse field distributions, the only distinguishing factor is the phase velocity. Therefore, a '+' or '–' sign has been added to the subscript to denote the sense of the phase velocity. This new notation allows for unambiguous reference to the various modes that have emerged from this analysis. It can be seen, then, that the DNG waveguide permits new slow-wave modes as well as new negative-phase-velocity modes.

Also of interest is the power flow density which may be calculated using the Poynting vector **S** as defined in equation (3-14). The difference between a fast-wave and slow-wave solution may be seen in Figure 4-11. As expected, power flow is concentrated at the center of a DPS slab, while it is focused more at the boundaries of a DNG slab. A fast-wave mode is depicted for the DPS slab and a slow-wave mode depicted for the DNG slab.

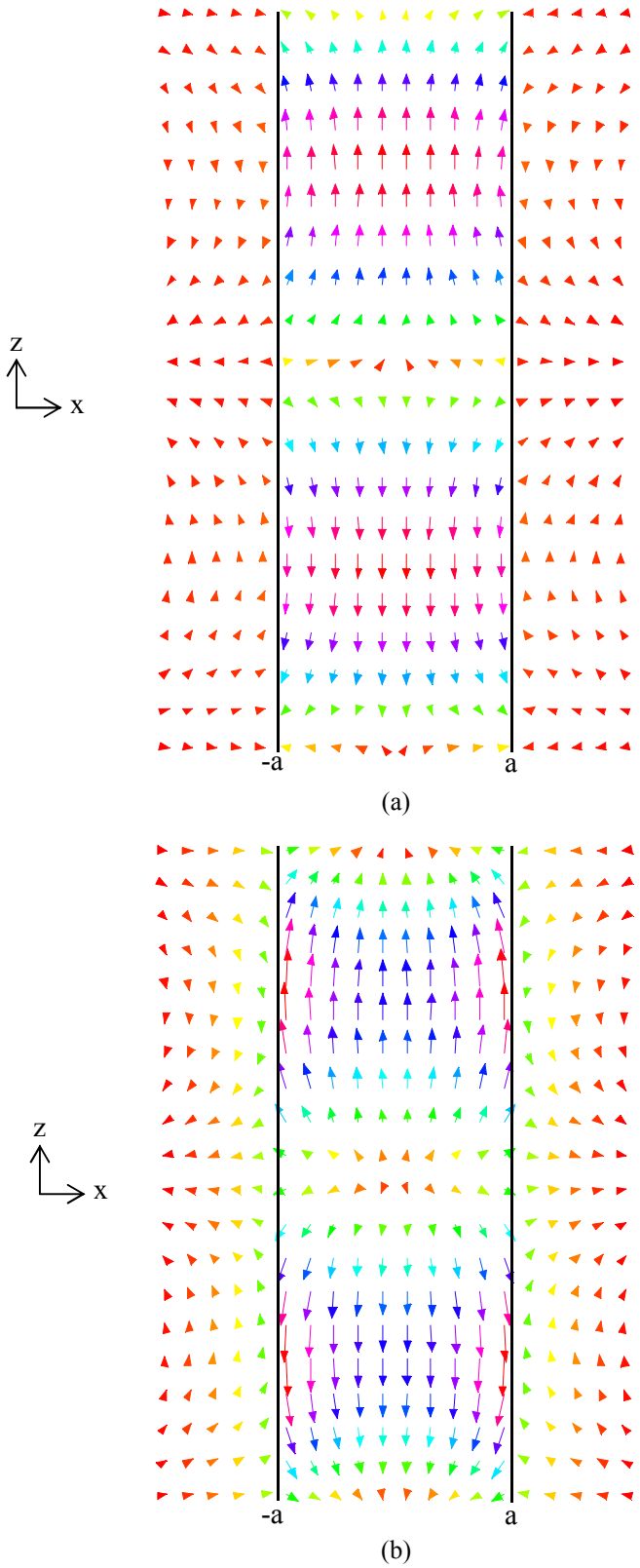


Figure 4-11. The power flow density (Poynting vector) for a fast-wave mode in a DPS slab waveguide (a) and a slow-wave mode in a DNG slab waveguide (b). Magnitude is depicted by arrow length in the first order and by arrow color in the second order.

4.8.2 Loss calculation

The analysis of the DNG slab thus far has ignored loss by neglecting the imaginary parts of the materials parameters μ and ε. As mentioned previously, however, loss may in fact be dealt with using perturbation theory over about ¾ of the DNG frequency range for the material model used in this investigation. Since the field distributions are known in the lossless case, (4-74) may be invoked to calculate the loss parameter α to a very close approximation anywhere in the low-loss portion of the DNG frequency range. This range, in fact, includes almost all the modes of interest (the lower-order modes). Although the manipulations are straightforward, the full equation for α shall not be given here due to its length.

In order to test the validity of the perturbation method approach, an exact method of calculating the complex propagation constant γ is helpful. For this, *Mathematica* may be used to perform a complex root search of the characteristic equation when the complex forms of the permittivity ε and permeability μ are used. A comparison of the results for these two methods is shown in Figure 4-12 for the fundamental TE_0- mode from Figure 4-10.

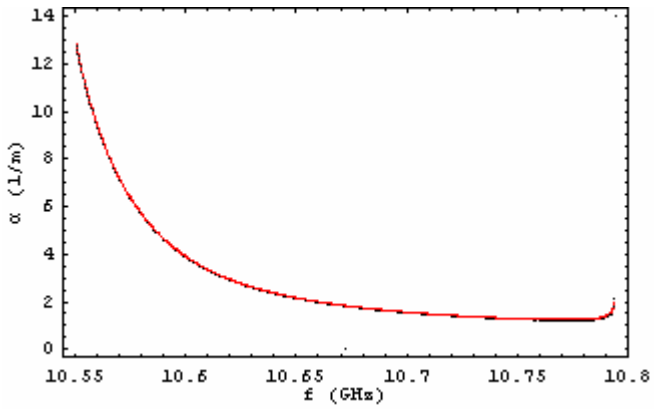


Figure 4-12. The loss parameter α for the fundamental TE_0 mode from Figure 4-7. The results from both the perturbation method (black) and an exact method (red) are shown. The results are in close agreement.

As can be seen in the figure above, there is very good agreement between the exact results and the results from the perturbation method. The waveguide appears to be

moderately lossy, as expected. This method has then been shown to be valid in this case, and confidence in it is strengthened for use in other cases as well.

Another interesting point about this figure is that the TE_{0-} mode contains negative values for β. This leads to positive values for α, meaning that the solution decays exponentially as it travels in the z-direction. If the *positive* value of β were used, then α would in fact be *negative* for this mode, implying that solutions would amplify exponentially in the positive z-direction. Since, again, it is assumed that the source is at negative infinity on the z-axis (or, at least, at or somewhere to the left of zero on the z-axis) then this would lead to an unphysical solution with the energy increasing as the solution traveled. Rejecting this scenario, the necessity of negative β for this mode, and thus positive energy velocity, is the only acceptable interpretation. This further buttresses the previous argument for negating the phase velocity for some portions of some modes.

4.9 Summary

This chapter has presented the foundations for studying N-layer dielectric waveguides containing DNG materials. A thorough analysis of the DNG slab waveguide was presented, building on the results from [60] and presenting some new results, including a new interpretation of the apparent presence of negative energy velocity of some solutions in the guide. The following chapters shall present new geometries which have not yet been discussed in the literature.

5 Five-Layer Dielectric Waveguide

The preceding chapter presented all the necessary elements to study N-layer waveguides containing either DPS materials, DNG materials or a combination thereof. Although the three-layer (slab) geometry has been investigated to a good extent [60-62], some new results and interpretations were presented. The next logical step in this investigation is to examine a slab with additional claddings. This chapter focuses on the five-layer (quadruple-clad) dielectric waveguide. The geometry of this structure is depicted in Figure 5-1. Although this seems as though it may not present any new results, there are possible geometries excluded from the three-layer structure, such as a "DNG tube" which is comprised of a DPS core and outer cladding but with a DNG inner cladding. Other unique possibilities exist which are worth investigating and shall be developed in the following discussion.

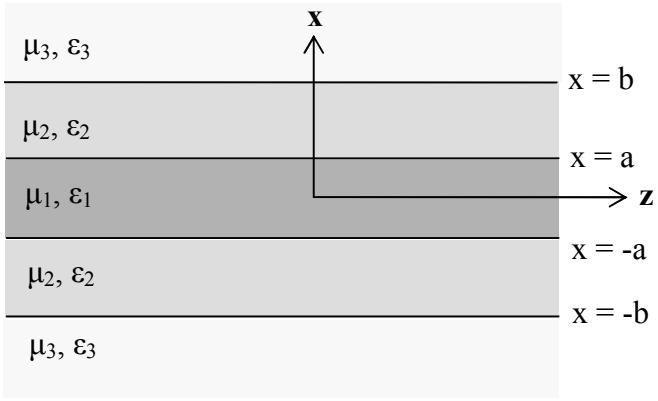


Figure 5-1. A two-dimensional five-layer (quadruple-clad) dielectric waveguide.

5.1 Characteristic equations

Using (4-33) through (4-39) along with all the required definitions of terms in these equations, the five-layer waveguide may be analyzed. The same boundary

conditions as were used for the three-layer waveguide apply to the five-layer waveguide as well: namely, the tangential fields (y- and z-components) must be equal at the material boundaries. Applying these boundary conditions allows for the determination of the characteristic equation for both the even and the odd TE and TM cases as well as the field coefficients A_2, B_2 and A_3 in terms of A_1 for even cases or B_1 for odd cases. The algebra is similar to the three-layer case but is more complicated. The results are tabulated in the following subsections, where several new terms have been defined as $U = q_1 a$, $X = q_2 a$, $Y = q_2 b$ and $W = q_3 b$. Also, κ and Q are defined as follows:

$$\kappa = \begin{cases} \dfrac{\nu_2 \mu_2}{\mu_3}\dfrac{W}{Y} & \text{TE} \\ \dfrac{\nu_2 \varepsilon_2}{\varepsilon_3}\dfrac{W}{Y} & \text{TM} \end{cases} \tag{5-1}$$

$$Q = \begin{cases} T_2^{-1}(\kappa) & \kappa < 1 \\ \coth^{-1}(\kappa) & \kappa > 1 \end{cases} \tag{5-2}$$

The function T_i^{-1} is simply the inverse of T_i. The function $\hat{T}_i$ and the term χ are defined below to simplify the results.

$$\hat{T}_i(x) = \begin{cases} \tan(x) & \nu_i = 1 \\ \tanh(x) & \nu_i = -1, |\kappa| < 1 \\ \coth(x) & \nu_i = -1, |\kappa| > 1 \end{cases} \tag{5-3}$$

$$\chi = \begin{cases} \dfrac{\nu_1 \mu_1}{\nu_2 \mu_2}\dfrac{X}{U} & \text{TE} \\ \dfrac{\nu_1 \varepsilon_1}{\nu_2 \varepsilon_2}\dfrac{X}{U} & \text{TM} \end{cases} \tag{5-4}$$

5.1.1 Even TE modes

For the even TE case, B_1 is equal to zero and A_1 corresponds to the initial field magnitude. Below are the field coefficients and the characteristic equation.

$$A_2 = A_1\left[\chi Z_1'(U)\bar{Z}_2(X) - Z_1(U)\bar{Z}_2'(X)\right] \tag{5-5}$$

$$B_2 = A_1\left[Z_1(U)Z_2'(X) - \chi Z_1'(U)Z_2(X)\right] \tag{5-6}$$

$$A_3 = A_1 e^{W}\left[\chi Z_1'(U)Z_2(Y-X) + Z_1(U)Z_2'(Y-X)\right] \tag{5-7}$$

$$U\,T_1(U) = \frac{\nu_1\mu_1}{\nu_2\mu_2} X\hat{T}_2(Q+X-Y) \tag{5-8}$$

The field coefficients are written in terms of A_1 and are the same for the even TM case, noting that χ varies between the TE and TM cases.

The characteristic equation is written in a very compact form and may be tested in the limits of $\varepsilon_3 \rightarrow \varepsilon_2$, $\upsilon_3 \rightarrow \upsilon_2$ and $b \rightarrow a$. In these limits, the five-layer waveguide becomes a three-layer waveguide and should have the same characteristic equation as written in (4-41). It may be seen that the left-hand side of (5-8) remains unchanged, while for the right-hand side X, Y and W become equal. This means that the $\hat{T}$ function becomes -1 and (5-8) becomes equal to (4-41) as expected. This lends credence to the results.

5.1.2 Odd TE modes

A similar procedure may be undertaken for the odd TE case. This yields the following results for the field coefficients and the characteristic equation, respectively.

$$A_2 = B_1\left[\chi\bar{Z}_1'(U)\bar{Z}_2(X) - \bar{Z}_1(U)\bar{Z}_2'(X)\right] \tag{5-9}$$

$$B_2 = B_1\left[\bar{Z}_1(U)Z_2'(X) - \chi\bar{Z}_1'(U)Z_2(X)\right] \tag{5-10}$$

$$A_3 = B_1 e^{W}\left[\chi\bar{Z}_1'(U)Z_2(Y-X) + \bar{Z}_1(U)Z_2'(Y-X)\right] \tag{5-11}$$

$$\frac{U}{T_1(U)} = -\frac{\mu_1}{\nu_2\mu_2} X\hat{T}_2(Q+X-Y) \tag{5-12}$$

The field coefficients are written in terms of B_1 in this case and are the same as those for the odd TM case. The characteristic equation of (5-12) may once again be shown to reduce to the three-layer characteristic equation (4-43) when the same limits are applied as were used in the even case. This results in the $\hat{T}$ function becoming -1, X becoming W and (5-12) revealing itself to be equal to (4-43).

5.1.3 Even TM modes

The field coefficients for the even TM case are the same as those for the even TE case. The factor χ is different for the TM case, but the expressions (5-5) through (5-7) are still valid. The characteristic equation, expressed below, is likewise similar, with the difference that the permeabilities μ_i are replaced by the permittivities ε_i.

$$U\,T_1(U) = \frac{\nu_1\,\varepsilon_1}{\nu_2\,\varepsilon_2}\,X\,\hat{T}_2(Q+X-Y) \tag{5-13}$$

The same test of validity, being the reduction to the slab characteristic equation under certain conditions, may be applied successfully here as well.

5.1.4 Odd TM modes

Finally, the field coefficients for the odd TM case are expressed in (5-9) through (5-11). The characteristic equation is expressed below, and may, like the other cases, be shown to reduce to the slab equation under the appropriate limits.

$$\frac{U}{T_1(U)} = -\frac{\varepsilon_1}{\nu_2\,\varepsilon_2}\,X\,\hat{T}_2(Q+X-Y) \tag{5-14}$$

It may be noted that for the characteristic equations, conversion from TE to TM modes (or vice versa) may be accomplished by changing μ_i to ε_i for all i (or vice versa). To convert from even to odd modes (or vice versa), it is sufficient to let $T_1(U)$ go to

$-\upsilon_1/T_1(U)$. These conversion rules are then applicable to anything derived from the characteristic equations as well (such as cutoff conditions).

All the information necessary to characterize the five-layer waveguide is now in place. The characteristic equation may be solved numerically and the field distributions found for particular solutions. Additionally, the loss parameter may be calculated, given a particular material model.

5.1.5 Limits on the propagation constant β

Similarly to Section 4.3.5, it may be argued that there are certain limitations on the propagation constant β in a planar dielectric waveguide. Although the entire argument will not be repeated in detail here, it will suffice to say that $\overline{\beta}^2$ must be greater than the square of the refractive index of the outermost layer, thus ensuring decay of the fields outside the waveguide, and that $\overline{\beta}^2$ must be less than the square of the maximum refractive index in the waveguide, thus limiting the solutions to fast-wave modes only. This applies to DPS-only waveguides. When DNG materials are mixed with DPS materials in the waveguide, the latter restriction is eliminated, thus allowing slow-wave modes as well. Thus, for DPS-only (or DNG-only) waveguides, $n_{outer}^2 < \overline{\beta}^2 < n_{maximum}^2$, while for mixed-material waveguides, $n_{outer}^2 < \overline{\beta}^2$. This implicitly assumes that fast-wave solutions are defined as any solution for which $\overline{\beta}^2 < n_{maximum}^2$, while slow-wave solutions are defined as any solution for which $\overline{\beta}^2 > n_{maximum}^2$. These restrictions and definitions are in fact general for any symmetric N-layer waveguide. For the five-layer waveguide, n_{outer} is the same as n_3.

5.2 Cutoff conditions

The cutoff conditions may be found in order to help determine what modes may exist in the waveguide as well as their minimum (or maximum) frequencies. In the case

of the five-layer waveguide, the characteristic equations are more complicated than for the slab and the algebra must be approached more carefully.

5.2.1 Fast-wave modes

For fast-wave modes, the cutoff condition is that $\overline{\beta}^2$ goes to n_3^2. This is the case only when $|n_1|$ and/or $|n_2|$ are greater than $|n_3|$. Otherwise, in the mixed-material case, this is in fact the cutoff for slow-wave modes. This latter case shall be treated in the following subsection. For the fast-wave cutoff condition, W becomes equal to zero, thus leading to both κ and Q becoming zero as well. The $\hat{T}_2$ function then simply becomes a T_2 function, and the cutoff condition is expressed below for even TE and TM modes, respectively.

$$U T_1(U) = \frac{\nu_1 \mu_1}{\nu_2 \mu_2} X T_2(X - Y) \tag{5-15}$$

$$U T_1(U) = \frac{\nu_1 \varepsilon_1}{\nu_2 \varepsilon_2} X T_2(X - Y) \tag{5-16}$$

Of particular interest here is determining whether or not a fundamental fast-wave mode may exist. It was seen in the case of the DNG slab waveguide that only the fundamental slow-wave mode could be found, while the fundamental fast-wave mode never exists. Here, however, it may be shown that the fundamental mode may in fact exist, depending on the parameters of the waveguide. This is seen partially by considering small values of ω, which leads to small values for U, X, Y and W. This allows the characteristic equation to be reduced to the following for the TE case by the use of some small argument approximations:

$$U^2 = \frac{\nu_1 \mu_1}{\nu_2 \mu_2} X \left(\frac{\nu_2 \mu_2}{\mu_3} \frac{W}{Y} + X - Y \right) \tag{5-17}$$

As can be seen, the left-hand side of (5-17) is positive. The term X-Y is negative, while X is positive. The sign of the right-hand side of the equation is then determined by the signs of the material parameters μ_1 and μ_2 and the factors υ_1 and υ_2 which depend on the relationship of the refractive indices n_1 and n_2 and the propagation constant $\bar{\beta}$. It is seen that real solutions to (5-17) may exist under certain conditions. For example, if at the frequency of interest $\left|\bar{\beta}\right|$ is less than both $|n_2|$ and $|n_1|$ and the core is DNG, it can be shown that solutions only exist if the following criterion, given in the equation below, is met. If this criterion is not met, no real solutions exist and it is concluded that the fundamental mode cannot exist in that case.

$$\frac{\mu_2}{\mu_3}\frac{W}{Y} < Y - X \tag{5-18}$$

The conditions for the other cases may be derived similarly. Generally, then, the fundamental mode may exist for this waveguide under certain conditions. The same argument made here for the fundamental TE_0 mode may also be made for the fundamental TM_0 mode. Furthermore, although this argument is for a small value of ω which may not be included in the DNG frequency range, the argument still stands. It may in fact be seen that the argument still applies to high DNG frequency ranges, as the use of a normalized frequency both for this argument and in studying the DNG range may in fact be more useful. In such a case, the argument above would be valid more directly.

In the odd case, the following equations apply for TE and TM modes, respectively:

$$\frac{U}{T_1(U)} = -\frac{\mu_1}{\nu_2 \mu_2} X T_2(X - Y) \tag{5-19}$$

$$\frac{U}{T_1(U)} = -\frac{\varepsilon_1}{\nu_2 \varepsilon_2} X T_2(X - Y) \tag{5-20}$$

For fast-wave modes, either T_1 or T_2 (or both) must be a tangent function. Due to the periodic nature of the tangent function, it is therefore expected that there are an

infinite number of solutions to (5-15), (5-16), (5-19) and (5-20). As a result, it is expected that there are an infinite number of fast-wave modes in a five-layer waveguide which may or may not contain DNG materials

5.2.2 Slow-wave modes

For slow-wave modes, the cutoff condition varies depending on the refractive index profile of the waveguide. Slow-wave modes may have cutoffs for $\left|\overline{\beta}\right|$ equal to either $|n_1|$, $|n_2|$ or $|n_3|$ depending on which of these refractive index magnitudes is the maximum. Each of these cases must be treated separately, and the results vary. For the first case where $\overline{\beta}^2$ goes to n_1^2, U becomes zero resulting in the left-hand side of the characteristic equations (5-8) and (5-12) through (5-14) becoming zero for even modes and unity for odd modes. Manipulating the right-hand side of the characteristic equations yields the following cutoff equations for even TE and even TM modes:

$$\hat{T}_2^{-1}\left(\frac{\mu_2}{\mu_3}\frac{W}{Y}\right) = X - Y \tag{5-21}$$

$$\hat{T}_2^{-1}\left(\frac{\varepsilon_2}{\varepsilon_3}\frac{W}{Y}\right) = X - Y \tag{5-22}$$

In these cases, since $Y = \frac{b}{a}X$, the right hand side of both (5-21) and (5-22) is always negative. The left-hand side is only negative when exactly one of the inner or outer claddings is DNG (*i.e.*, either the two inner cladding layers must be DNG or the two outer cladding layers must be DNG). Realistically, then, there is only a solution in this case when the inner cladding layers are DNG. This may include a DNG core, but this condition is not necessary for a real solution to these cutoff equations. The $\hat{T}_2^{-1}$ function is then either a $\tanh^{-1}$ or a $\coth^{-1}$ function. In either case, there is then only one solution to (5-21) and (5-22) since the $\tanh^{-1}$ and $\coth^{-1}$ functions are non-periodic.

For the odd TE and TM cases, the following cutoff conditions apply:

$$\mu_1 X \hat{T}_2 (Q + X - Y) - \mu_2 = 0 \tag{5-23}$$

$$\varepsilon_1 X \hat{T}_2 (Q + X - Y) - \varepsilon_2 = 0 \tag{5-24}$$

Following a similar argument to what was made for the even case, it may be shown that there can be only one solution to (5-23) and one solution to (5-24) due to the non-periodic nature of hyperbolic tangent and cotangent functions. It may then be seen that there can be a maximum of two slow-wave TE modes and two slow-wave TM modes with cutoffs at $|n_1|$.

The next possibility is that $|n_2|$ is the maximum refractive index magnitude, but this case must be treated very carefully. Both X and Y become zero in this situation, but it is necessary to consider the small and large argument approximations of some hyperbolic functions in order to find a non-trivial result. When this is done, the cutoff conditions for even TE and TM modes, respectively, are found to be the following:

$$U \tanh(U) + \frac{\varepsilon_1}{\frac{b}{a}\left(\varepsilon_2 + \varepsilon_3 \frac{1}{W}\right) - \varepsilon_3} = 0 \tag{5-25}$$

$$U \tanh(U) + \frac{\mu_1}{\frac{b}{a}\left(\mu_2 + \mu_3 \frac{1}{W}\right) - \mu_3} = 0 \tag{5-26}$$

In the case of odd TE and TM modes, the results are:

$$U \coth(U) + \frac{\varepsilon_1}{\frac{b}{a}\left(\varepsilon_2 + \varepsilon_3 \frac{1}{W}\right) - \varepsilon_3} = 0 \tag{5-27}$$

$$U \coth(U) + \frac{\mu_1}{\frac{b}{a}\left(\mu_2 + \mu_3 \frac{1}{W}\right) - \mu_3} = 0 \tag{5-28}$$

Once again in these cases, as in the cases of the maximum refractive index being $|n_1|$, hyperbolic tangent and cotangent functions appear in the cutoff conditions. Since

these functions are, unlike regular tangent and cotangent functions, non-periodic, there can be only one solution to each of the cutoff equations (5-25) through (5-28). There can then be a maximum of two slow-wave modes for each of the TE and TM cases. The exact number of existing modes for both this case and the previous case is determined by the parameters of the waveguide.

Finally, the case of $|n_3|$ being the maximum refractive index may be considered. This case is the same as was considered for fast modes, and so the results in (5-15), (5-16), (5-19) and (5-20) are valid here as well. The only difference is that in the fast-wave cutoff case, $|n_3|$ is necessarily less than either (or both) $|n_1|$ or $|n_2|$.

5.3 Numerical analysis

Now that the characteristic equations, field coefficients and cutoff conditions have been determined, it is appropriate to begin numerical analysis of the five-layer waveguide. It is convenient to first look at a conventional DPS-only five-layer waveguide for the purposes of comparison. Only one refractive index profile will be chosen, as this waveguide has been widely studied and is just needed in one case to highlight the unique features when DNG materials are included.

5.3.1 DPS waveguide

All the characteristic equations, field coefficients and cutoff conditions derived thus far are valid both for waveguides that contain DNG materials as well as those that do not. Solving the characteristic equations numerically, as was done in the case of the slab waveguide, yields the results depicted in Figures 5-2 and 5-3 for TE and TM modes, respectively. For this case, a = 1m and b = 2m, and all permeabilities μ_i are equal to μ_0. The refractive indices are $n_1 = 1.2$, $n_2 = 1.1$ and $n_3 = 1.0$.

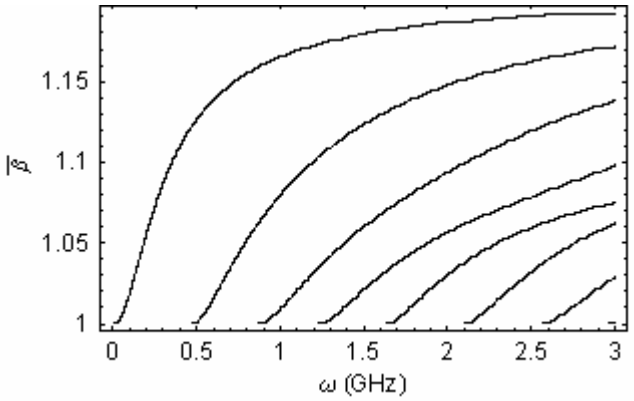


Figure 5-2. The TE dispersion characteristics for a five-layer waveguide with a = 1m, b = 2m, all permeabilities equal to μ_0, $n_1 = 1.2$, $n_2 = 1.1$ and $n_3 = 1.0$.

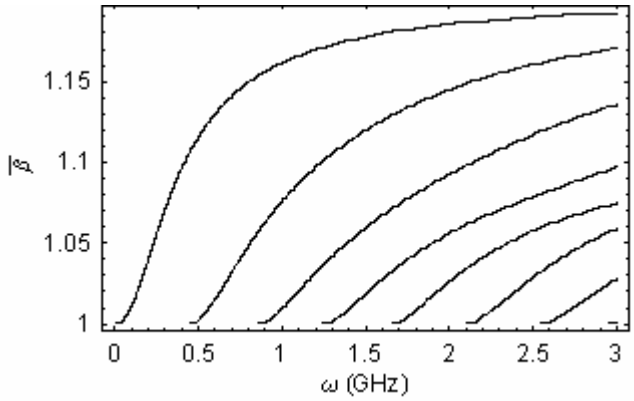


Figure 5-3. The TM dispersion characteristics for a five-layer waveguide with a = 1m, b = 2m, all permeabilities equal to μ_0, $n_1 = 1.2$, $n_2 = 1.1$ and $n_3 = 1.0$.

The results seen in the two figures above are rather similar to the results for the slab waveguide. There are some differences resulting from the addition of a pair of inner cladding layers, mainly manifested as a distortion of the shape of the curves at higher frequencies. As expected, there are only fast-wave modes with $\bar{\beta}$ less than n_1. The fast-wave modes are sometimes identified as core modes and cladding modes, where in this case the core modes correspond to $n_2 < \bar{\beta} < n_1$ and the cladding modes correspond to $n_3 < \bar{\beta} < n_2$.

It may be seen in Figure 5-4 that the field distributions are likewise similar to the case of the slab, albeit with some minor differences owing to the inclusion of a pair of inner cladding layers. These distributions are shown for the TE_0 mode at a frequency of 500 MHz.

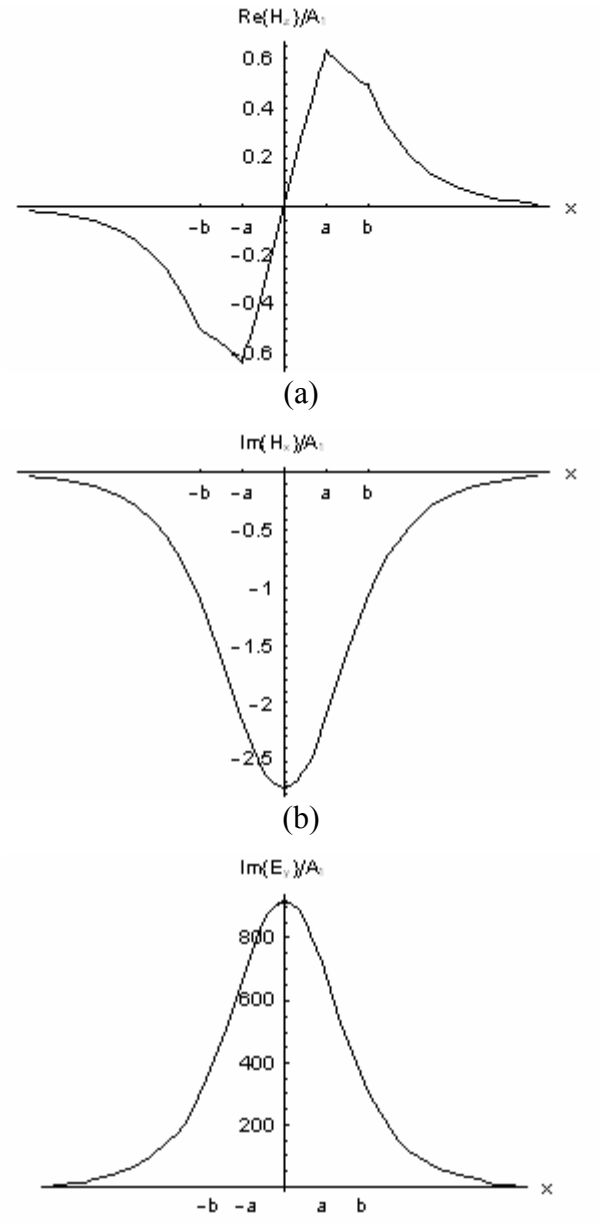


Figure 5-4. The field distributions for the TE_0 mode of the five-layer waveguide from Figure 5-2 at 500 MHz.

Again, these distributions are similar to the slab, but some differences can be seen especially in plot (a) of the figure where the inner claddings are located. These results may then be used as a standard of comparison for the five-layer waveguide containing DNG materials.

5.3.2 Refractive index profiles

It is helpful in the analysis to first consider what refractive index profiles are possible for the five-layer waveguide when DNG materials are used, as the addition of an extra set of cladding layers beyond the simple slab waveguide allows for more variations. The case which includes the outer cladding layers as DNG shall be ignored as this is an unphysical geometry. The various profiles are shown in Figure 5-5 where the refractive indices of DNG layers vary with frequency. Furthermore, the absolute values of the refractive indices are plotted for clarity, and only cases with either the core being DNG or the inner cladding layers being DNG are included. Cases with two sets of DNG layers and one set of DPS layers are in fact analogous to two DPS and one DNG and are therefore somewhat redundant.

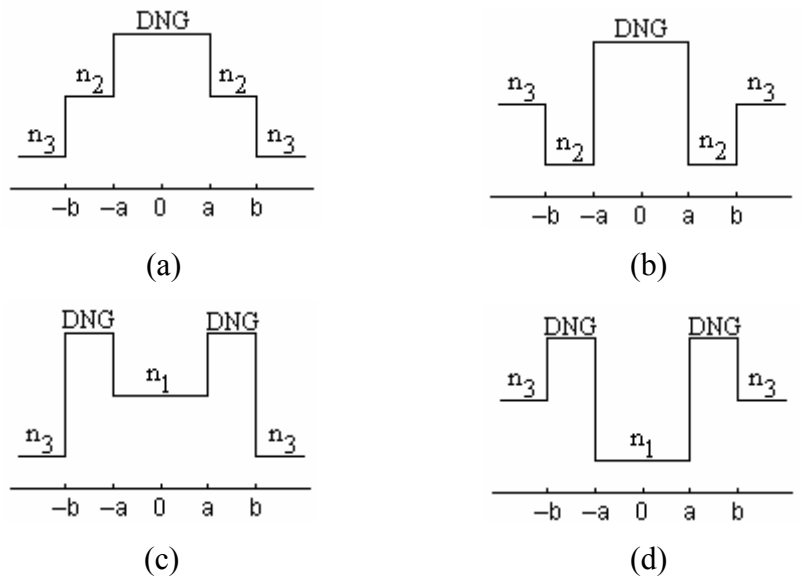
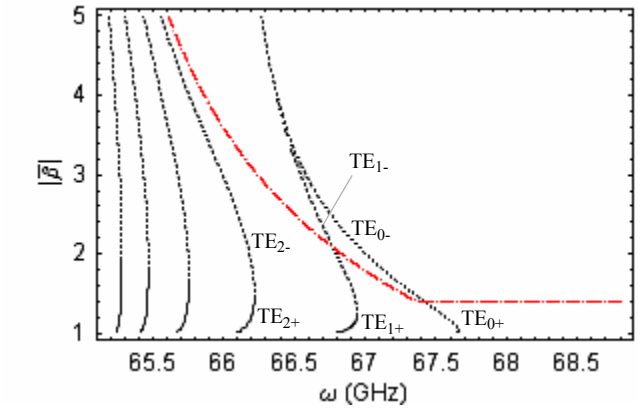


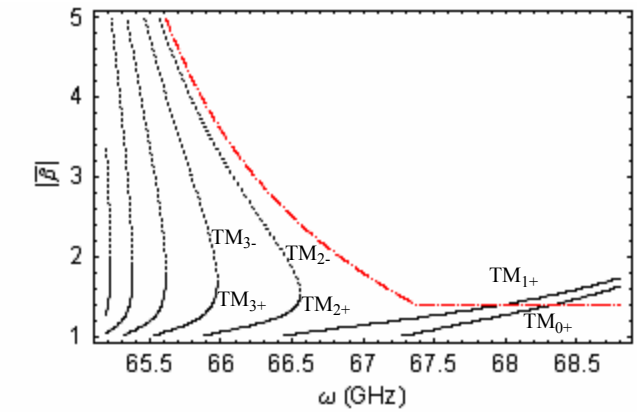
Figure 5-5. The four possible refractive index magnitude profiles containing one set of DNG layers (core or inner cladding). The DNG layers vary from zero to negative infinity with frequency. The profiles are not necessarily to scale.

These refractive index profiles may be studied individually in terms of the dispersion characteristics and cutoff conditions. Both the TE and TM cases are included in the following dispersion figures, where for all DPS materials the permeability μ is equal to μ_0. The dimensions have been selected as a = 0.5cm and b = 1cm. The DNG material model used previously for the slab waveguide shall be used here as well, where

the governing equations are (4-65) and (4-66), and the material parameters are based on experimental results in [4] for an actual DNG metamaterial. Furthermore, only the first few lower-order modes are shown, and some are labeled appropriately in the figures. There are an infinite number of higher-order modes in the DNG frequency range below 65.2 GHz, but these become infinitely dense and begin to clutter the results, and therefore they are omitted here. The absolute values of the solutions shall be plotted, but the positive $\overline{\beta}$ values shall be plotted as solid black lines while the negative $\overline{\beta}$ values shall be dashed black lines.

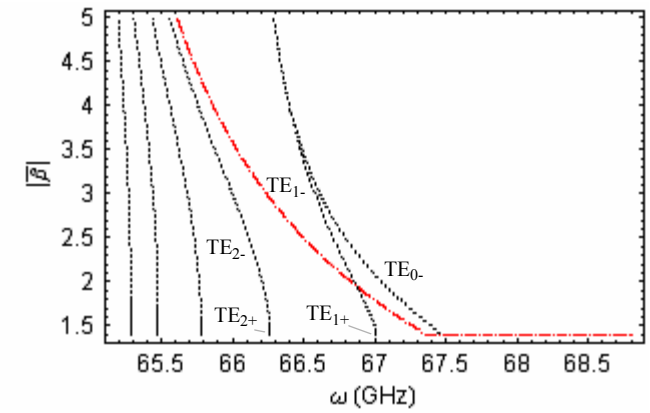


(a)

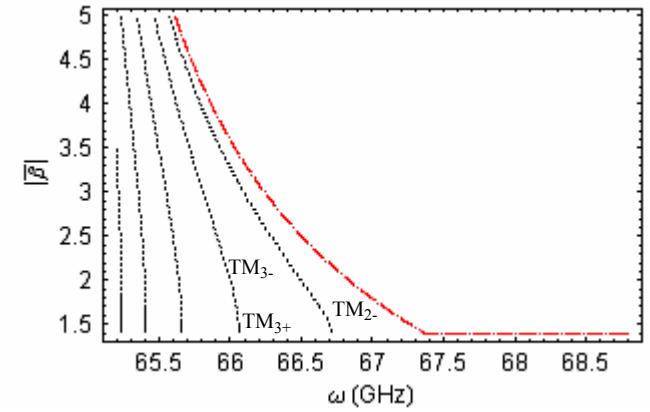


(b)

Figure 5-6. The TE (a) and TM (b) dispersion characteristics for a five-layer waveguide with the refractive index profile of Figure 5-5(a). Both the positive (solid black) solutions and negative (dashed black) solutions are shown. The first few modes are labeled with the appropriate notation. The guide parameters are a = 0.5cm, b = 1cm, $n_3 = 1.0$, $n_2 = 1.4$ and n_1 is governed by the material model of (4-65) and (4-66) and the parameters given in [4]. The maximum refractive index (dot-dashed red) is also shown.

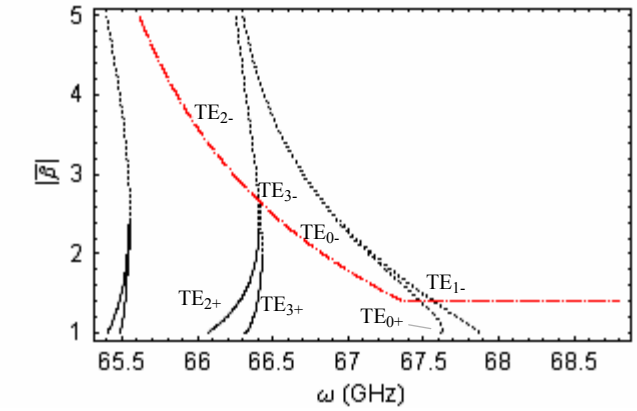


(a)

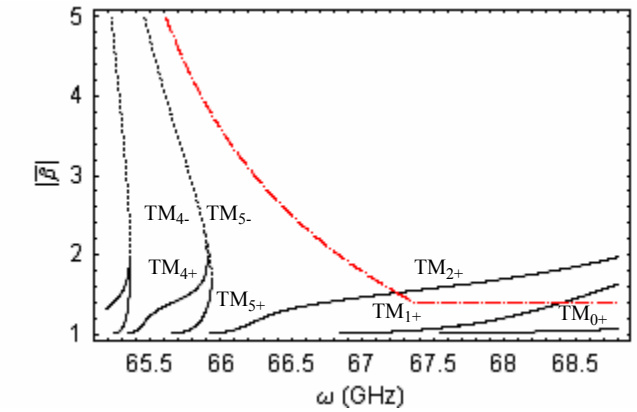


(b)

Figure 5-7. The TE (a) and TM (b) dispersion characteristics for a five-layer waveguide with the refractive index profile of Figure 5-5(b). Both the positive (solid black) solutions and negative (dashed black) solutions are shown. The first few modes are labeled with the appropriate notation. The guide parameters are a = 0.5cm, b = 1cm, $n_3 = 1.4$, $n_2 = 1.0$ and n_1 is governed by the material model of (4-65) and (4-66) and the parameters given in [4]. The maximum refractive index (dot-dashed red) is also shown.

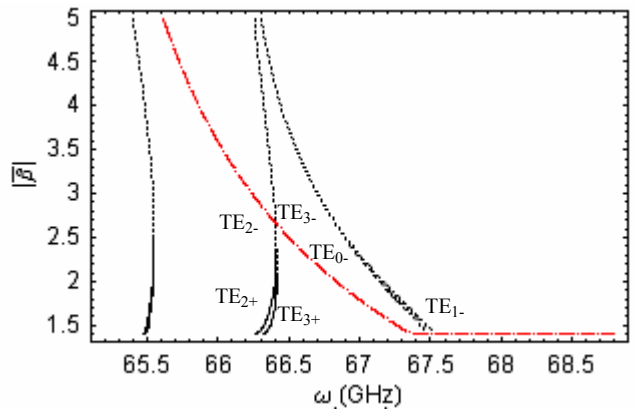


(a)

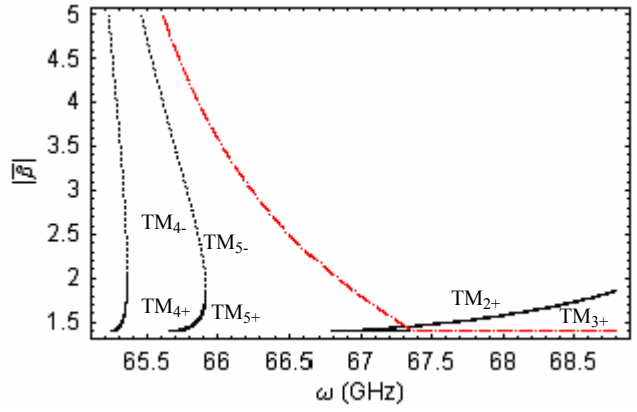


(b)

Figure 5-8. The TE (a) and TM (b) dispersion characteristics for a five-layer waveguide with the refractive index profile of Figure 5-5(c). Both the positive (solid black) solutions and negative (dashed black) solutions are shown. The first few modes are labeled with the appropriate notation. The guide parameters are a = 0.5cm, b = 1cm, $n_3 = 1.0$, $n_1 = 1.4$ and n_2 is governed by the material model of (4-65) and (4-66) and the parameters given in [4]. The maximum refractive index (dot-dashed red) is also shown.



(a)



(b)

Figure 5-9. The TE (a) and TM (b) dispersion characteristics for a five-layer waveguide with the refractive index profile of Figure 5-5(d). Both the positive (solid black) solutions and negative (dashed black) solutions are shown. The first few modes are labeled with the appropriate notation. The guide parameters are a = 0.5cm, b = 1cm, $n_3 = 14$, $n_1 = 1.0$ and n_2 is governed by the material model of (4-65) and (4-66) and the parameters given in [4]. The maximum refractive index (dot-dashed red) is also shown.

There are a number of unique features in the dispersion characteristics for the five-layer waveguide, as seen in the above figures, over those of the three-layer waveguide. In the first case, depicted in Figure 5-6 and corresponding to the refractive index profile of Figure 5-5(a), it can be seen that the fundamental fast-wave mode exists in both the TE and TM cases. Interestingly, in the TE case there exist both the TE_{0-} and TE_{0+} modes, while for the TM case there exists only the TE_{0+} mode. The same is true for the first mode as well. For the slow-wave TE modes, the cutoff of the fundamental mode is n_2, while the cutoff of the first-order mode is $|n_1|$. In the TM case, the cutoff for both the slow-wave modes is n_2.

For the second case corresponding to the refractive index profile of Figure 5-5(b), the dispersion characteristics in Figure 5-7 are similar to the previous case with the most

notable exception being that there is no fundamental fast-wave mode for either the TE or TM data. The cutoffs for the TE slow-wave modes are similar in both this and the previous case. Another striking feature of these results is the fact that the first two modes (TM_0 and TM_1) are entirely absent. This is a curious result which is not typically seen in standard waveguides, but has emerged when DNG materials are used here. Both this case and the previous case involved a DNG core.

The last two cases, corresponding to Figures 5-8 and 5-9, involve a set of DNG inner cladding layers. This waveguide acts, in effect, like a "DNG tube." This type of geometry is wholly unavailable in the three-layer waveguide, and as expected presents some fascinating and unique features unseen even in other DNG waveguides. In the case of the dispersion characteristics of Figure 5-8 which corresponds to the refractive index profile of Figure 5-5(c), the TE data reveals that the modes are in fact out of the typical order. As the frequency is decreased in the DNG range, it is seen that the odd modes appear *before* the even modes, resulting in the first-order TE_1 mode occurring at higher frequencies than the fundamental TE_0 mode. The sequence continues with TE_3, TE_2, TE_5, TE_4, *et cetera*. These numerical subscripts are again determined by the number of nodes in the transverse field distribution. Specifically, the y-component of the fields (e_y in the TE case and h_y in the TM case) is what is of interest when DNG materials are used, as the x-component of the fields (h_x in the TE case and e_x in the TM case) shows discontinuities which may appear to be nodes but in fact are not. Furthermore, there exist a total of four slow-wave TE modes, two of which have cutoffs of $|n_2|$ and two of which have cutoffs of $|n_1|$. It may additionally be seen that the modes appear in 'pairs' in all cases, whereas for previous results only the slow-wave modes appear 'paired.' This is another interesting feature of this waveguide, as for purely DPS five-layer waveguides modes appear to be individual and ungrouped as seen in Figures 5-2 and 5-3.

In the TM case, the results are even more complicated with the first three modes appearing in the expected order, followed by a completely absent third-order TM_3 mode and then a return to the reversed order seen in the TE case. These results are, again, unique to this type of waveguide. Another interesting feature is that the fundamental TM_0 mode is purely fast-wave, a result not seen in previous refractive index profiles for this waveguide. There exist only two slow-wave modes, and these like the fundamental

mode are purely positive-phase-velocity modes. The other modes are a mix of positive- and negative-phase-velocity modes.

The final case, corresponding to the refractive index profile of Figure 5-5(d), reveals a combination of the results already seen. The TE case shows results similar to those seen in Figure 5-8, with the exception that the fundamental fast-wave mode is missing. In the TM case, the first two lower-order modes are entirely absent. In both the TE and TM cases, the mode order reversal is seen, and there are a total of four slow-wave TE modes and two slow-wave TM modes.

5.3.3 Appearance of new modes

In addition to the unique features seen thus far, it may be shown that by properly adjusting the parameters of the five-layer waveguide in some cases, *new* modes can begin to appear. Rather than being an increase in mode density, which may also be effected by adjusting the waveguide parameters, this is in fact a matter of new instances of already existing modes (such as TE_3) appearing at the high-frequency end of the DNG range. This behavior may be seen by varying the inner cladding widths, that is the parameter b, for the same waveguide as was studied in Figure 5-6. Figure 5-10 depicts the dispersion characteristics for several values of b.

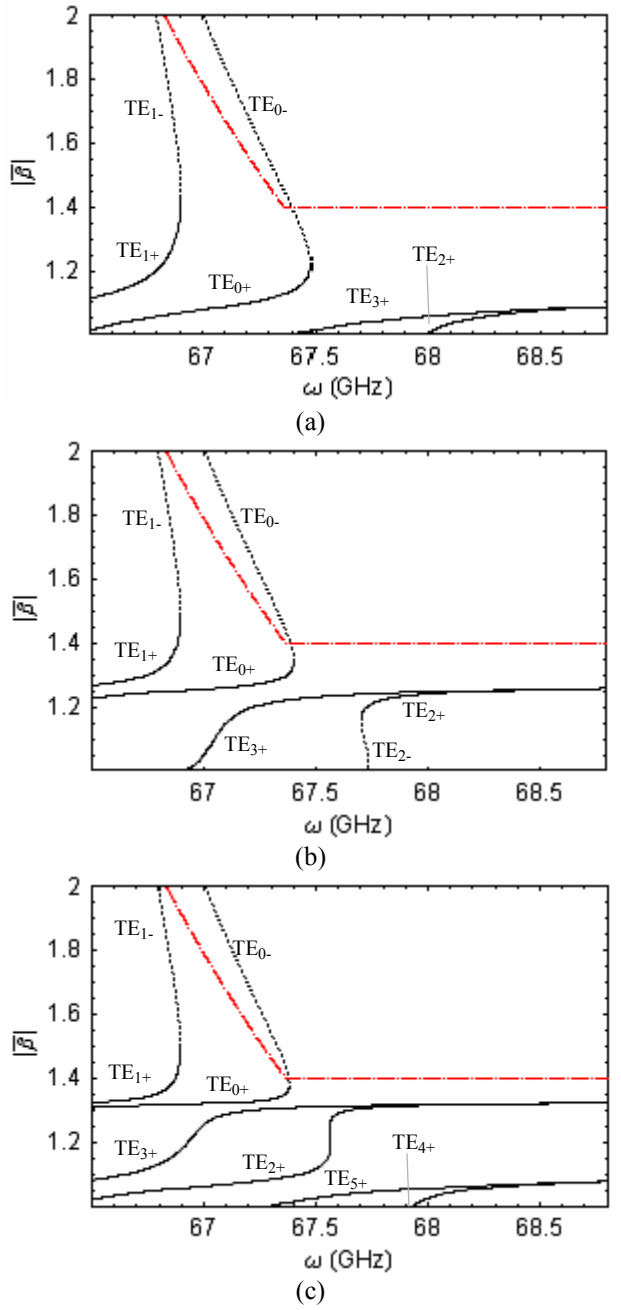


Figure 5-10. The TE dispersion characteristics for a five-layer waveguide also examined in Figure 5-6, but for b = 1.5cm (a), b = 2.25cm (b) and b = 3cm (c). The maximum refractive index (dot-dashed red) is shown for reference. Positive phase velocity solutions (solid black) are shown along with negative phase velocity solutions (dashed black)

As can be seen in the above figure, new modes begin to appear at higher frequencies in the DNG range and extend further into the lower-frequency portion as b increases. These new modes appear out of the expected order once again, with odd modes appearing prior to the corresponding lower-order even modes. Furthermore, these

new modes do not include the fundamental TE_0 mode or the first-order TE_1 mode. This is another unique result which is not seen in DPS waveguides and which is not seen even in three-layer DNG waveguides. These new modes are in fact entirely new instances of already existing modes which occur at lower frequencies. For example, the TE_3 mode already exists in the waveguide, but a new instance of this mode appears at higher frequencies in the DNG range.

5.3.4 Field distributions

Also of interest are the field distributions for these waveguides. A TE_0 e_y field distribution for each of the four waveguides in Figures 5-6 through 5-9 are shown in Figure 5-11. These distributions show once again that when DNG materials are included, the fields are focused at the material interfaces.

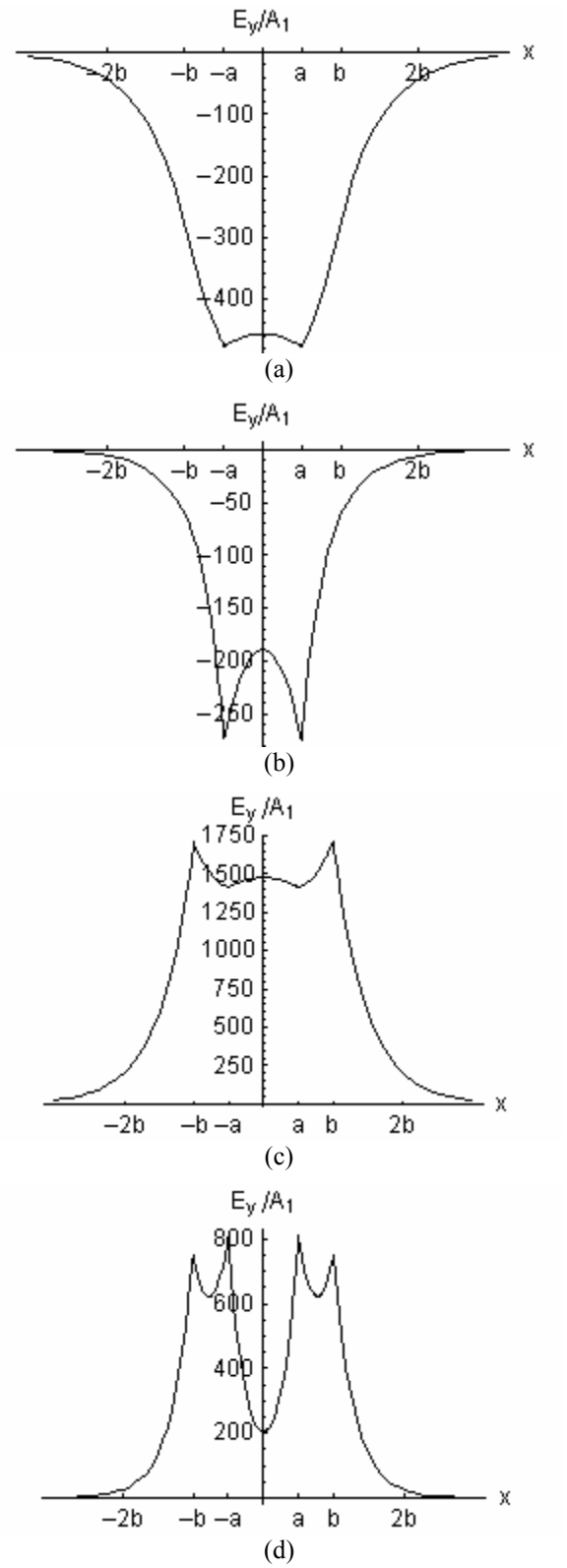


Figure 5-11. The normalized field distributions for the TE_0 mode for the waveguide in Figure 5-6 at 67.5 GHz (a), Figure 5-7 at 67.1 GHz (b), Figure 5-8 at 67.5 GHz (c) and Figure 5-9 at 67.1 GHz (d).

5.4 Summary

The five-layer waveguide has been shown to yield some very fascinating and unique results not seen in either DPS waveguides or the three-layer DNG waveguide. These results have included modes that appear out of order, absent modes, the return of the fundamental mode in some cases and the existence of new instances of already-existing modes for some configurations. The most fascinating results have been seen with the "DNG tube" waveguide, where the inner cladding layers only are DNG. Although this investigation has not considered the use of many DNG materials, it has been exhaustive enough to cover the main points of interest.

6 Photonic Crystal Waveguide

The photonic crystal waveguide consists of an infinite number of periodic cladding layers placed symmetrically about a core region and thus serves as a limiting case for multi-layer planar dielectric waveguides. The analysis of this geometry may be approached using two different methods: a field (matrix) method and a ray method. The field method is largely an extension of the approach taken for analyzing previously discussed geometries. The ray method is a different technique but one which, as it turns out, is equivalent to the field approach. Although, as will be seen, the ray approach yields a closed-form solution to the slab with an infinite number of symmetrically placed periodic claddings, there is no apparent way to acquire the same solution with a full field approach. However, the results may be compared later by applying the field approach to a slab with a large, finite number of claddings. It is expected that for a large enough number of layers the guide with finite number of claddings should yield results very close to the guide with infinite number of claddings.

6.1 Ray analysis

The photonic crystal waveguide of interest here shall have two alternating cladding layers, as shown by the refractive index profile in Figure 6-1. The use of more refractive indices is possible, but the analysis is more complicated and the present case shall suffice as a canonical example.

The ray analysis of the planar photonic crystal waveguide presented here is based on a novel impedance approach used in [82]. This method may be validated by first examining a simpler case involving three planar layers. Figure 6-2 illustrates the geometry of the three-layer structure. The above illustration may be specified for either TE or TM cases in exactly the same manner as Figures 3-2 and 3-3. Although the mathematical details are not included here, it will suffice to say that by writing the fields

in each of the three regions and imposing the appropriate boundary conditions, the reflection coefficient at the surface of the center slab may be found. The results are shown below for the TE and TM cases, respectively.

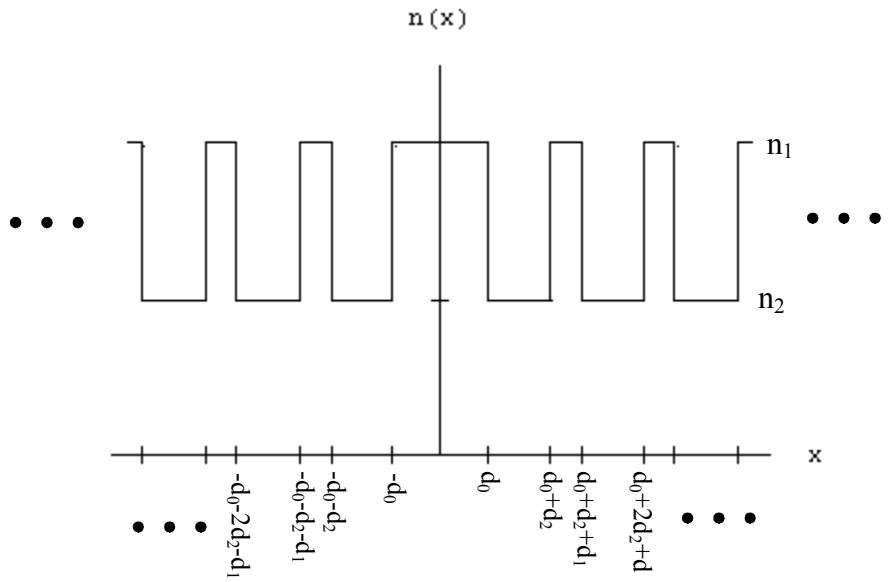


Figure 6-1. Refractive index profile of a photonic crystal waveguide.

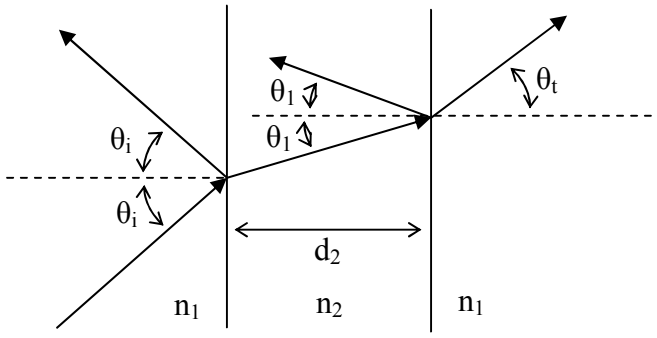


Figure 6-2. Three-layer planar structure with incident ray (plane wave).

$$\Gamma_{TE} = \frac{\left(\eta_2^2 \cos^2\theta_i - \eta_1^2 \cos^2\theta_1\right)\left(1 - e^{-\phi}\right)}{\left(\eta_2 \cos\theta_i + \eta_1 \cos\theta_1\right)^2 - \left(\eta_2 \cos\theta_i - \eta_1 \cos\theta_1\right)^2 e^{-\phi}} \tag{6-1}$$

$$\Gamma_{TM} = \frac{\left(\eta_2^2 \cos^2\theta_1 - \eta_1^2 \cos^2\theta_i\right)\left(1 - e^{-\phi}\right)}{\left(\eta_2 \cos\theta_1 + \eta_1 \cos\theta_i\right)^2 - \left(\eta_2 \cos\theta_1 - \eta_1 \cos\theta_i\right)^2 e^{-\phi}} \tag{6-2}$$

Here, $\varphi = j\ 2\ k_2\ d_2 \cos\theta_1$ where k_2 is the wave number in the center layer and $\cos\theta_1$ may be defined in terms of the incident angle as per (3-33). In terms of an impedance approach to this particular problem, Γ may be defined as follows using transmission line theory:

$$\Gamma = \frac{Z_{in} - Z_1}{Z_{in} + Z_1} \tag{6-3}$$

Here, Z_{in} is defined as follows:

$$Z_{in} = Z_2 \frac{Z_1 + jZ_2 \tan(\beta_2 d_2)}{Z_2 + jZ_1 \tan(\beta_2 d_2)} \tag{6-4}$$

In (6-4), Z_1 and Z_2 are the intrinsic impedances of the media with refractive indices n_1 and n_2, respectively, and are defined as the square root of the quantity permeability divided by permittivity. Performing the substitution of (6-4) into (6-3) yields the following expression:

$$\Gamma = \frac{(Z_2^2 - Z_1^2)(1 - e^{-\rho})}{(Z_2 + Z_1)^2 - (Z_2 - Z_1)^2 e^{-\rho}} \tag{6-5}$$

Here, $\rho = j\ 2\ \beta_2\ d_2$. It is noted that (6-5) has the same form as (6-1) and (6-2) if $\beta_2 = k_2 \cos\theta_1$ and the following definitions are used:

$$Z_1 = \begin{cases} \eta_1 \cos\theta_i & \text{TM} \\ \eta_1 / \cos\theta_i & \text{TE} \end{cases} \tag{6-6}$$

$$Z_2 = \begin{cases} \eta_2 \cos\theta_1 & \text{TM} \\ \eta_2 / \cos\theta_1 & \text{TE} \end{cases} \tag{6-7}$$

The definitions for the TE case may be seen by dividing both the numerator and denominator of (6-1) by the square of the product of the cosines of the angles. It is seen,

then, that with the appropriate definitions of impedances, oblique ray incidence on a planar structure may be modeled using impedance in the same manner as with transmission lines.

The analysis may now turn back to the case of an infinite number of periodically placed layers. Since the number of layers is both infinite and periodic, the input impedance should also be periodic since no matter how far into the structure it is observed, there are always an infinite number of layers remaining. This is illustrated in Figure 6-3.

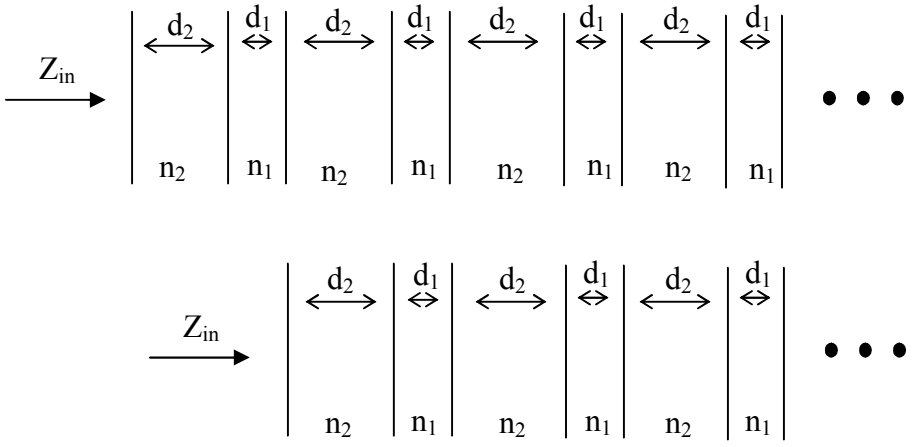


Figure 6-3. Input impedance for an infinitely layered cladding (top) is the same as that of the same cladding, less the first two layers (bottom).

It is therefore the case that the two scenarios depicted in Figure 6-4 must be equivalent. By the same logic, the scenarios in Figure 6-5 must likewise be the same.

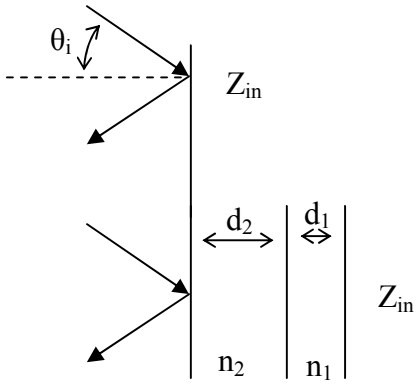


Figure 6-4. A ray incident on an infinitely layered structure. The input impedance is periodic, and therefore the top and bottom diagrams are equivalent.

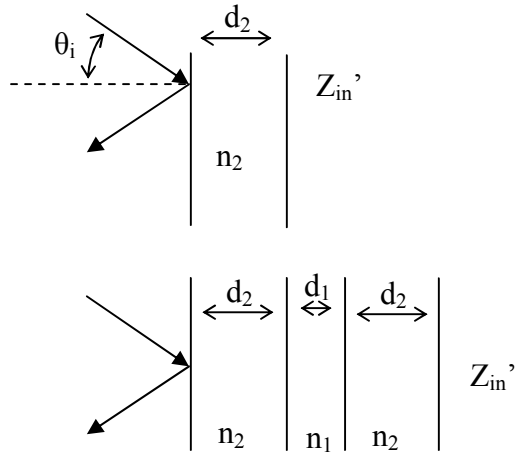


Figure 6-5. A ray incident on an infinitely layered structure. The input impedance is periodic, and therefore the top and bottom diagrams are equivalent.

The input impedances Z_{in} and Z_{in}' are in general different. However, the preceding figures illustrate a principle which may be used for calculating these impedances. In doing so, first the following definitions may be made. It must also be noted that θ_i is the angle of propagation in all n_1 layers and θ_1 is the (refracted) angle of propagation in all n_2 layers, and therefore (3-33) may be used to relate the two angles.

$$\phi_1 = k_1 d_1 \cos\theta_i = k_0 d_1 \sqrt{n_1^2 - \bar{\beta}^2} = k_0 d_1 u = U \tag{6-8}$$

$$\phi_2 = k_2 d_2 \cos\theta_1 = k_0 d_2 \sqrt{\bar{\beta}^2 - n_2^2} = j k_0 d_2 w = j W \tag{6-9}$$

It is important to note the distinction between the upper- and lower-case definitions for U and W, as the lower-case version does not involve the layer width d_i. The expressions for Z_1 and Z_2 may be likewise rewritten in terms of these definitions:

$$Z_1 = \begin{cases} \dfrac{u}{c\varepsilon_1} & \text{TM} \\ \dfrac{c\mu_1}{u} & \text{TE} \end{cases} \tag{6-10}$$

$$Z_2 = \begin{cases} j\dfrac{w}{c\varepsilon_2} & \text{TM} \\ j\dfrac{c\mu_2}{w} & \text{TE} \end{cases} \tag{6-11}$$

Here, c is the speed of light in a vacuum. Taking note of (6-6), (6-7) and the two preceding figures, the following expressions may now be written:

$$Z'_{in} = Z_1 \frac{Z_{in} + jZ_1 \tan\phi_1}{Z_1 + jZ_{in} \tan\phi_1} \tag{6-12}$$

$$Z_{in} = Z_2 \frac{Z'_{in} + jZ_2 \tan\phi_2}{Z_2 + jZ'_{in} \tan\phi_2} \tag{6-13}$$

By inserting (6-12) into (6-13) and rearranging the terms, a quadratic equation in terms of Z_{in} is obtained. This equation may be solved to yield Z_{in} in terms of known parameters of the structure. This solution takes the following form:

$$Z_{in} = j\frac{\bar{b}_0 \pm \sqrt{\bar{b}_0^2 - 4\bar{a}_0\,\bar{c}_0}}{2\bar{a}_0} \tag{6-14}$$

Here, a_0, b_0 and c_0 have been defined as follows, where it must be noted that their forms depend on whether the case under consideration is TE (lower lines) or TM (upper lines):

$$\bar{a}_0 = \begin{Bmatrix} \dfrac{w}{c\,\varepsilon_2} \\ -\dfrac{c\,\mu_2}{w} \end{Bmatrix} \tan U + \begin{Bmatrix} \dfrac{u}{c\,\varepsilon_1} \\ \dfrac{c\,\mu_1}{u} \end{Bmatrix} \tanh W \qquad \begin{matrix} \text{TM} \\ \\ \text{TE} \end{matrix} \tag{6-15}$$

$$\bar{b}_0 = \tan U \ \tanh W \left(\begin{Bmatrix} \dfrac{u^2}{c^2\,\varepsilon_1^2} \\ \dfrac{c^2\,\mu_1^2}{u^2} \end{Bmatrix} + \begin{Bmatrix} \dfrac{w^2}{c^2\,\varepsilon_2^2} \\ \dfrac{c^2\,\mu_2^2}{w^2} \end{Bmatrix} \right) \qquad \begin{matrix} \text{TM} \\ \\ \text{TE} \end{matrix} \tag{6-16}$$

$$\bar{c}_0 = \begin{Bmatrix} \dfrac{u\,w}{c^2\,\varepsilon_1\,\varepsilon_2} \\ -\dfrac{c^2\,\mu_1\,\mu_2}{u\,w} \end{Bmatrix} \left(\begin{Bmatrix} \dfrac{u}{c\,\varepsilon_1} \\ \dfrac{c\,\mu_1}{u} \end{Bmatrix} \tan U - \begin{Bmatrix} \dfrac{w}{c\,\varepsilon_2} \\ -\dfrac{c\,\mu_2}{w} \end{Bmatrix} \tanh W \right) \qquad \begin{matrix} \text{TM} \\ \\ \text{TE} \end{matrix} \tag{6-17}$$

Using these results along with the scenario depicted in the top portion of Figure 6-4 and assuming the material to the left of the structure has refractive index n_1, the reflection coefficient is found by way of (6-3). Rewriting Z_{in} as $-j\,\bar{Z}_{in}$ yields the following expression:

$$\Gamma = \frac{-j\bar{Z}_{in} - Z_1}{-j\bar{Z}_{in} + Z_1} \tag{6-18}$$

Of interest is the phase (or argument) of (6-18), which is expressed below:

$$\gamma_0 = -2\tan^{-1}\left(\frac{Z_1}{\bar{Z}_{in}}\right) \tag{6-19}$$

The two-dimensional photonic crystal waveguide may now be analyzed. The geometry of this waveguide is depicted in Figure 6-6.

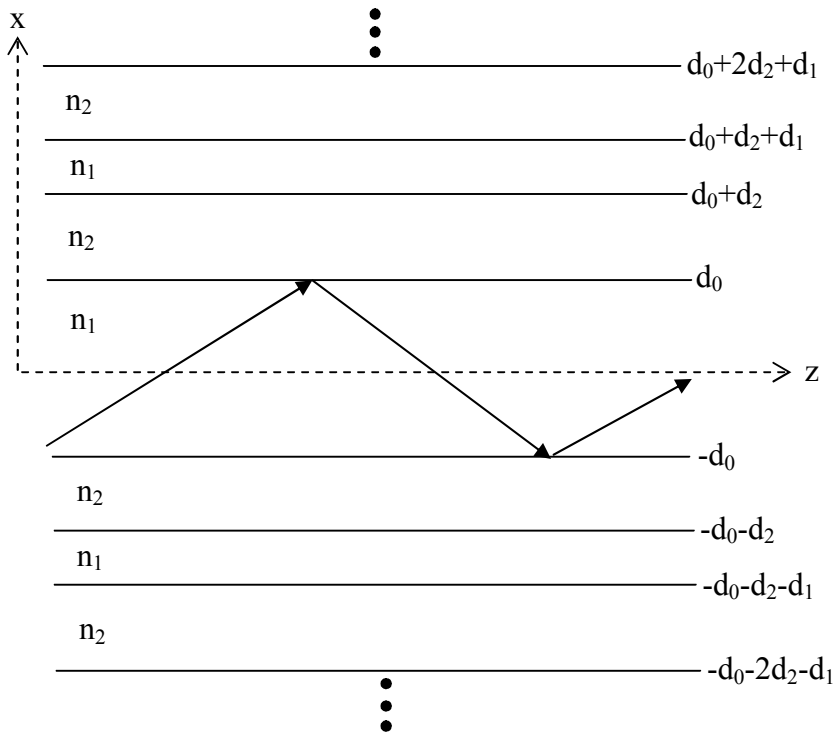


Figure 6-6. Geometry and parameters for a two-dimensional photonic crystal waveguide.

The propagation constant β must satisfy the transverse resonance condition in order for a pair of incident and reflected rays in the core region to constitute a guided mode. This condition means that the phase change in the transverse direction (x) through one full cycle must be equal to some integer multiple of 2π radians. This may be written mathematically as the following:

$$2k_0 \int_{-d_0}^{d_0} \sqrt{n_1^2 - \overline{\beta}^2}\, dx + 2\gamma_0 = -2u \int_{-d_0}^{d_0} dx + 2\gamma_0 = 2N\pi \tag{6-20}$$

Defining $U_0 = u\, d_0$, (6-20) may be rewritten as the following:

$$-\tan^{-1}\frac{Z_1}{\overline{Z}_{in}} = U_0 + \frac{N\pi}{2} \tag{6-21}$$

Taking the tangent of both sides of (6-21) and substituting (6-14) yields:

$$\frac{-2\,\bar{a}_0\,Z_1}{\tan\left(U_0+\dfrac{N\pi}{2}\right)}-\bar{b}_0=\pm\sqrt{\bar{b}_0^2-4\,\bar{a}_0\,\bar{c}_0} \tag{6-22}$$

In order to consider all possible solutions, (6-22) may be squared and reorganized. The new equation below contains all the solutions for either sign choice.

$$\bar{a}_0\,Z_1^2+\bar{b}_0\,Z_1\tan\left(U_0+\frac{N\pi}{2}\right)+\bar{c}_0\tan^2\left(U_0+\frac{N\pi}{2}\right)=0 \tag{6-23}$$

The propagation constant β may be obtained by solving this equation numerically for know values of waveguide parameters and the frequency.

6.2 Pseudo-photonic crystal waveguide

The preceding calculations are for an ideal photonic crystal waveguide with an infinite number of layers. The ray analysis was performed to calculate the modal propagation constant β, but also of interest is an analysis by way of fields. Although such an analysis yields no apparent solution in the case of an infinite number of claddings, it may be assumed that for a large number of layers the solutions should be very close to those of the actual photonic crystal waveguide.

The refractive index profile for the pseudo-photonic crystal waveguide is the same as in Figure 6-1 with the exception that it terminates with an outer cladding of index n_2 at some finite distance from the origin. The field approach taken here is very similar to that used in Chapters 4 and 5 for the N-layer waveguide. However, some slight modifications shall be made, but the formulation is essentially the same. Knowing that the solutions of the wave equations for the two-dimensional planar geometry, given in (4-26) and (4-27), are sinusoids or exponentials, the following general functions may be defined:

$$Z_i(x) = \begin{cases} \sin x & \text{i odd} \\ e^{-x} & \text{i even} \end{cases} \tag{6-24}$$

$$\overline{Z}_i(x) = \begin{cases} \cos x & \text{i odd} \\ e^{x} & \text{i even} \end{cases} \tag{6-251}$$

Although these functions are slightly different than (4-31) and (4-32), they act in essentially the same manner, as exponentials and hyperbolic sinusoids are related functions. Primed notation shall be the same as in preceding chapters, where the primed function represents the derivative with respect to the argument. The functions in (6-24) and (6-25) may be used to represent the solutions to the wave equation for the core or for either cladding. To facilitate the analysis the following terms are defined:

$$u_i = \sqrt{\nu_i \left(k_0^2 n_i^2 - \beta^2 \right)} \tag{6-26}$$

$$\nu_i = \begin{cases} 1 & \text{i odd} \\ -1 & \text{i even} \end{cases} \tag{6-27}$$

$$U_i = u_i x_i \tag{6-28}$$

$$W_i = u_{i+1} x_i \tag{6-29}$$

These definitions, including (6-24) and (6-25), are made where the core is considered the layer for which i = 1, the first cladding i = 2 and so on. Then, it is appropriate to state the following:

$$n_i = \begin{cases} n_1 & \text{i odd} \\ n_2 & \text{i even} \end{cases} \tag{6-30}$$

Further, it is noted that x_i is the value of x at the boundary between the i^{th} and the $(i+1)^{th}$ layer, as expressed below.

$$x_i = d_0 + \left\lfloor \frac{i}{2} \right\rfloor d_2 + \left\lfloor \frac{i-1}{2} \right\rfloor d_1 \tag{6-31}$$

Here the notation $\lfloor\ \rfloor$ signifies a floor function.

Using the preceding definitions and (4-22) through (4-25), the fields in the i^{th} layer are written as follows for TE and TM cases. The z-dependence of the fields is omitted and the lower case notation used as a result. For TE modes:

$$h_{zi}(x) = A_i\, Z_i(u_i\, x) + B_i\, \overline{Z}_i(u_i\, x) \qquad x_{i-1} < x < x_i \tag{6-32}$$

$$h_{xi}(x) = -\frac{j\beta\nu_i}{u_i}\left[A_i\, Z_i'(u_i\, x) + B_i\, \overline{Z}_i'(u_i\, x) \right] \qquad x_{i-1} < x < x_i \tag{6-33}$$

$$e_{yi}(x) = \frac{j\omega\mu_i\nu_i}{u_i}\left[A_i\, Z_i'(u_i\, x) + B_i\, \overline{Z}_i'(u_i\, x) \right] \qquad x_{i-1} < x < x_i \tag{6-34}$$

For TM modes:

$$e_{zi}(x) = A_i\, Z_i(u_i\, x) + B_i\, \overline{Z}_i(u_i\, x) \qquad x_{i-1} < x < x_i \tag{6-35}$$

$$e_{xi}(x) = -\frac{j\beta\nu_i}{u_i}\left[A_i\, Z_i'(u_i\, x) + B_i\, \overline{Z}_i'(u_i\, x) \right] \qquad x_{i-1} < x < x_i \tag{6-36}$$

$$h_{yi}(x) = -\frac{j\omega\varepsilon_i\nu_i}{u_i}\left[A_i\, Z_i'(u_i\, x) + B_i\, \overline{Z}_i'(u_i\, x) \right] \qquad x_{i-1} < x < x_i \tag{6-37}$$

Boundary conditions may now be applied by equating the tangential fields at the interfaces. The results are the following:

$$h_{zi}(x_i) = h_{zi+1}(x_i) \tag{6-38}$$

$$e_{yi}(x_i) = e_{yi+1}(x_i) \tag{6-39}$$

$$e_{zi}(x_i) = e_{zi+1}(x_i) \tag{6-40}$$

$$h_{yi}(x_i) = h_{yi+1}(x_i) \tag{6-41}$$

Using this approach, it is possible to find the field coefficients A and B of the $(i+1)^{th}$ layer in terms of the coefficients of the i^{th} layer. The algebra is lengthy but not complicated, and only the results shall be presented here. A matrix equation results which takes the following form for both TE and TM cases:

$$\begin{pmatrix} A_{i+1} \\ B_{i+1} \end{pmatrix} = \begin{pmatrix} a_{11}^{i} & a_{12}^{i} \\ a_{21}^{i} & a_{22}^{i} \end{pmatrix} \begin{pmatrix} A_{i} \\ B_{i} \end{pmatrix} \tag{6-42}$$

The matrix elements a^i for TE modes are expressed below.

$$a_{11}^{i} = \begin{cases} \frac{1}{2}\left[\sin U_i + \frac{w_i \mu_i}{U_i \mu_{i+1}} \cos U_i \right] e^{W_i} & \text{i odd} \\ \left[\sin W_i + \frac{w_i \mu_i}{U_i \mu_{i+1}} \cos W_i \right] e^{-U_i} & \text{i even} \end{cases} \tag{6-43}$$

$$a_{12}^{i} = \begin{cases} \frac{1}{2}\left[\cos U_i - \frac{w_i \mu_i}{U_i \mu_{i+1}} \sin U_i \right] e^{W_i} & \text{i odd} \\ \left[\sin W_i - \frac{w_i \mu_i}{U_i \mu_{i+1}} \cos W_i \right] e^{U_i} & \text{i even} \end{cases} \tag{6-44}$$

$$a_{21}^{i} = \begin{cases} \frac{1}{2}\left[\sin U_i - \frac{w_i \mu_i}{U_i \mu_{i+1}} \cos U_i \right] e^{-W_i} & \text{i odd} \\ \left[\cos W_i - \frac{w_i \mu_i}{U_i \mu_{i+1}} \sin W_i \right] e^{-U_i} & \text{i even} \end{cases} \tag{6-45}$$

$$a_{12}^{i} = \begin{cases} \frac{1}{2}\left[\cos U_i + \frac{w_i \mu_i}{U_i \mu_{i+1}} \sin U_i \right] e^{-W_i} & \text{i odd} \\ \left[\cos W_i + \frac{w_i \mu_i}{U_i \mu_{i+1}} \sin W_i \right] e^{U_i} & \text{i even} \end{cases} \tag{6-46}$$

For the TM case, the matrix elements a^i are as follows:

$$a_{11}^{i} = \begin{cases} \frac{1}{2}\left[\sin U_i + \frac{w_i \varepsilon_i}{U_i \varepsilon_{i+1}} \cos U_i\right] e^{W_i} & \text{i odd} \\ \left[\sin W_i + \frac{w_i \varepsilon_i}{U_i \varepsilon_{i+1}} \cos W_i\right] e^{-U_i} & \text{i even} \end{cases} \tag{6-47}$$

$$a_{12}^{i} = \begin{cases} \frac{1}{2}\left[\cos U_i - \frac{w_i \varepsilon_i}{U_i \varepsilon_{i+1}} \sin U_i\right] e^{W_i} & \text{i odd} \\ \left[\sin W_i - \frac{w_i \varepsilon_i}{U_i \varepsilon_{i+1}} \cos W_i\right] e^{U_i} & \text{i even} \end{cases} \tag{6-48}$$

$$a_{21}^{i} = \begin{cases} \frac{1}{2}\left[\sin U_i - \frac{w_i \varepsilon_i}{U_i \varepsilon_{i+1}} \cos U_i\right] e^{-W_i} & \text{i odd} \\ \left[\cos W_i - \frac{w_i \varepsilon_i}{U_i \varepsilon_{i+1}} \sin W_i\right] e^{-U_i} & \text{i even} \end{cases} \tag{6-49}$$

$$a_{12}^{i} = \begin{cases} \frac{1}{2}\left[\cos U_i + \frac{w_i \varepsilon_i}{U_i \varepsilon_{i+1}} \sin U_i\right] e^{-W_i} & \text{i odd} \\ \left[\cos W_i + \frac{w_i \varepsilon_i}{U_i \varepsilon_{i+1}} \sin W_i\right] e^{U_i} & \text{i even} \end{cases} \tag{6-50}$$

The field coefficients for the n+1th layer of the waveguide may be written in terms of the field coefficients in the core:

$$\begin{pmatrix} A_{n+1} \\ B_{n+1} \end{pmatrix} = \begin{pmatrix} b_{11} & b_{12} \\ b_{21} & b_{22} \end{pmatrix} \begin{pmatrix} A_1 \\ B_1 \end{pmatrix} \tag{6-51}$$

Here, the square matrix is defined as:

$$\begin{pmatrix} b_{11} & b_{12} \\ b_{21} & b_{22} \end{pmatrix} = \begin{pmatrix} a_{11}^{n} & a_{12}^{n} \\ a_{21}^{n} & a_{22}^{n} \end{pmatrix} \begin{pmatrix} a_{11}^{n-1} & a_{12}^{n-1} \\ a_{21}^{n-1} & a_{22}^{n-1} \end{pmatrix} \cdots \begin{pmatrix} a_{11}^{1} & a_{12}^{1} \\ a_{21}^{1} & a_{22}^{1} \end{pmatrix} \tag{6-52}$$

The above analysis gives a complete account of the pseudo-photonic waveguide. The results may be further qualified by considering even and odd cases in light of (6-32) and (6-35). For even solutions $B_1 = 0$, while for odd cases $A_1 = 0$. It is also known that

for guided modes the fields in the outer cladding must decay exponentially away from the interface. This means that the field coefficient B_n of the outer cladding must be zero. For even cases, (6-51) indicates that this condition is satisfied when $b_{21} = 0$. For odd cases, the condition is satisfied for $b_{22} = 0$. These expressions are in fact the characteristic equations for the waveguide from which the propagation constant β may be calculated. As mentioned earlier, there is no apparent way to determine the characteristic equation for the case when the number of layers goes to infinity, although it is conceivable that with the proper mathematical manipulations an equality with the results for the full photonic crystal waveguide may be established.

6.3 Unique features of the photonic crystal waveguide

One interesting feature of the photonic crystal waveguide is the lack of any definite "outer cladding." As a result, there is no specific point at which the requirement for exponential decay must be imposed. Unlike solutions of planar geometries with a finite number of claddings where the normalized propagation constant $\overline{\beta}$ must be greater than the refractive index of the outer cladding, this lack of a definite outer cladding suggests that $\overline{\beta}$ may take values anywhere from zero to the maximum refractive index. This is expressed as $0 < \overline{\beta} < n_{max}$. The modes between zero and the minimum refractive index are the so-called photonic crystal modes. Additionally, with the added presence of DNG materials, the possibility for $\overline{\beta}$ to be greater than n_{max} also becomes apparent. This can be seen by examining the characteristic equation (6-23) for the case where $\overline{\beta}$ is greater than n_{max}. U and U_0 may then be expressed as $j\hat{U}$ and $j\hat{U}_0$ respectively, where $\hat{U}$ and $\hat{U}_0$ are both real. Then, these factors are defined as $\hat{U} = k_0 d_1 \sqrt{\overline{\beta}^2 - n_1^2}$ and $\hat{U}_0 = k_0 d_0 \sqrt{\overline{\beta}^2 - n_1^2}$. Despite the presence of imaginary values, the imaginary factor j ultimately cancels out of the equation, leaving a purely real equation. This does not rule out solutions of this kind, and therefore it is expected that these solutions may in fact appear in the analysis. Therefore, at this stage of the analysis it may be stated that the

normalized propagation constant $\overline{\beta}$ may take any positive value. If, as with other planar geometries studied thus far, $\overline{\beta}$ may also be negative, then in fact there are no fundamental limits on the value of $\overline{\beta}$. That is, $-\infty < \overline{\beta} < \infty$.

The pseudo-photonic crystal waveguide, on the other hand, has a definite outer cladding, and therefore $\overline{\beta}$ cannot take values less than the refractive index of this outer cladding. However, presumably with DNG materials the limitation that $\overline{\beta}$ be less than n_{max} may be overcome.

6.4 Numerical analysis and Comparison

As with analyses of other planar geometries, the characteristic equation for the photonic or pseudo-photonic crystal waveguide must be solved numerically. Once this is accomplished, the results may be compared. Again, it is expected that the solutions for the ray method (photonic crystal waveguide) should be almost exactly the same as those for the field method (pseudo-photonic crystal waveguide) when a sufficiently large number of layers is used, and it does in fact turn out that this is the case [82]. Additionally, there are indeed solutions present for $\overline{\beta}$ less than n_2 for the photonic crystal waveguide. Of primary interest here shall be the case where DNG materials are included.

6.4.1 DPS photonic crystal waveguide

As with other geometries, it is helpful to briefly review the results for DPS-only waveguides as a standard of comparison when investigating waveguides containing DNG materials. Figure 6-7 depicts the TE dispersion characteristics for a waveguide with $d_0 = d_1 = d_2 = 1$cm, $n_1 = 1.5$ and $n_2 = 1$. All relative material parameters are equal to unity with the exception of $\varepsilon_{1r} = 2.25$. Figure 6-8 depicts the TM dispersion characteristics for the same waveguide.

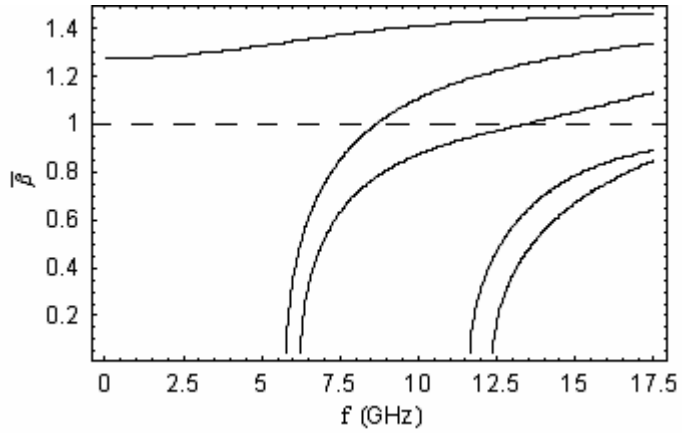


Figure 6-7. TE dispersion characteristics (solid) for the photonic crystal waveguide with $d_0 = d_1 = d_2 =$ 1cm, $\mu_1 = \mu_0$, $\mu_2 = \mu_0$, $\varepsilon_1 = 2.25\ \varepsilon_0$ and $\varepsilon_2 = \varepsilon_0$. The boundary between conventional modes and photonic crystal modes is denoted by a dashed line.

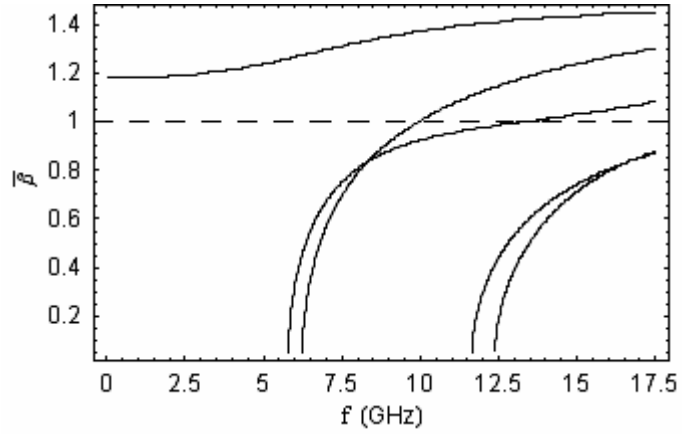


Figure 6-8. TM dispersion characteristics (solid) for the photonic crystal waveguide with $d_0 = d_1 = d_2 =$ 1cm, $\mu_1 = \mu_0$, $\mu_2 = \mu_0$, $\varepsilon_1 = 2.25\ \varepsilon_0$ and $\varepsilon_2 = \varepsilon_0$. The boundary between conventional modes and photonic crystal modes is denoted by a dashed line.

These results depict both the conventional modes with solutions for $\bar{\beta}$ between n_1 and n_2 as well as the so-called photonic crystal modes for which $\bar{\beta}$ is between zero and n_2 in this case. The modes are seen to be continuous across the boundary at $\bar{\beta} = n_2$. One curiosity is the crossings seen in the TM dispersion characteristics, where an odd and even mode cross each other at a point. This is a feature not seen in typical waveguides and may likely be an artifact of the infinite number of claddings used.

It is important to test the validity of the field approach to the pseudo-photonic crystal waveguide as well. This may be done by examining the solution for $\bar{\beta}$ at a particular frequency with various numbers of cladding layers as compared to the solution

for $\bar{\beta}$ for the photonic crystal waveguide at the same frequency. The results are shown in Figure 6-9 for the TE_0 mode at 2.5 GHz. These data show that as the number of layers in the pseudo-photonic crystal waveguide increases, the solution for $\bar{\beta}$ approaches the value in the photonic crystal waveguide.

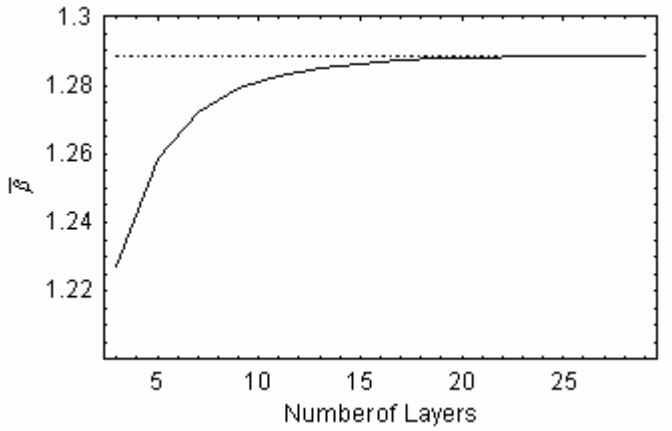
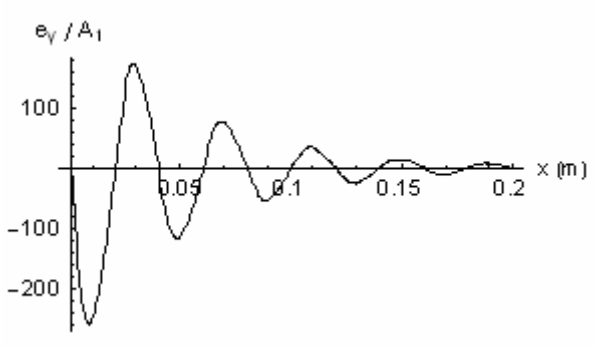
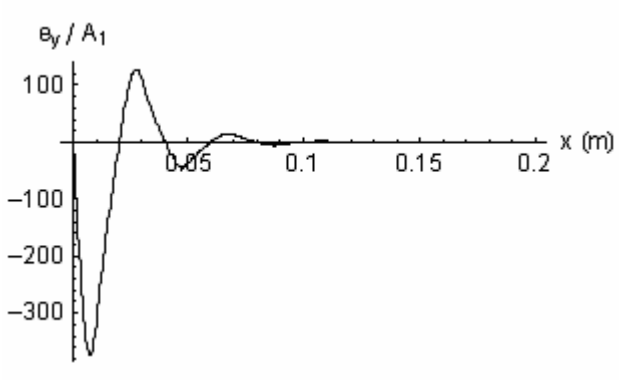


Figure 6-9. Comparison of the solution for the TE_0 mode at 2.5 GHz for the photonic crystal waveguide (broken) and the pseudo-photonic crystal waveguide with a varying number of layers (solid).

The field distributions for the solutions to the waveguide may now be examined. Figure 6-10 depicts the transverse electric field (e_y) distribution for the TE_1 mode for both a conventional solution ($\bar{\beta} > n_2$) and a photonic crystal solution ($\bar{\beta} < n_2$). Only one half of the space is shown, but since it is known that this is an odd mode, it is clear that it is anti-symmetric.



(a)



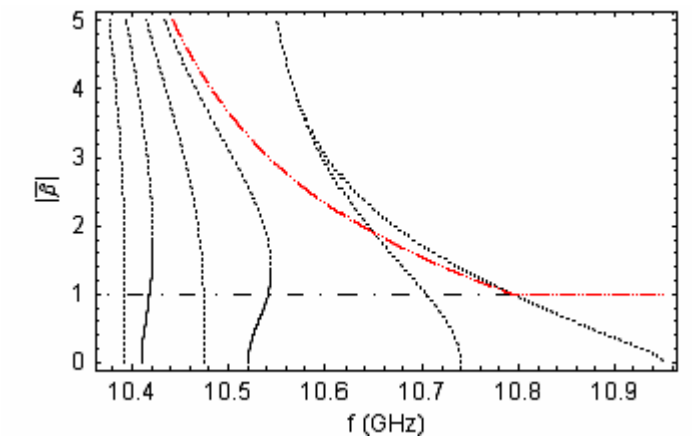
(b)

Figure 6-12. Normalized field distributions for the TE_1 mode at (a) 6 GHz ($\bar{\beta} = 0.355627$) and at (b) 10 GHz ($\bar{\beta} = 1.10629$).

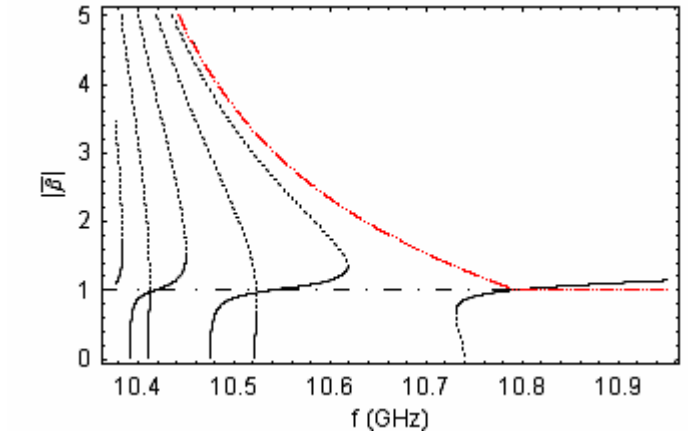
The above distributions show the necessary decay with distance from the core that is expected for physical solutions.

6.4.2 DNG photonic crystal waveguide

The photonic crystal waveguide becomes even more interesting when DNG materials are included. As in the analysis of previous configurations, the dispersive material model of (4-65) and (4-66) is used along with the parameters from [4]. The case of interest here are for n_1 being DNG and for n_2 being DPS. The DPS material shall simply be a vacuum for simplicity, and the layer widths d_0, d_1 and d_2 shall all be equal to 5mm. The results are shown in Figure 6-11.



(a)



(b)

Figure 6-11. TE (a) and TM (b) dispersion characteristics for the photonic crystal waveguide with n_1 (dot-dot-dashed red) being DNG and $n_2 = 1$. All layers have a width of 5mm. The positive-phase-velocity modes (solid black) and the negative-phase-velocity modes (dashed black) are expressed as absolute values. The dot-dashed line indicates the border between conventional solutions and photonic crystal solutions.

In the above results, the usual provisions are made for causality by reversing the sign of the solutions whose group velocity is negative. This creates causal solutions with positive group velocity and negative phase velocity. All the modes are plotted as positive absolute values but are differentiated by the style of the curves such that positive-phase-velocity modes are solid and negative-phase-velocity modes are dashed. The most striking feature of these results is that, as seen for the TE_{0-} mode, any value of $\bar{\beta}$ may be assumed. This fundamental mode alone, in fact, spans the entire range of solutions from zero to infinity.

For the TE dispersion characteristics, the modes are largely negative-phase-velocity modes, with the exception of small portions of the higher-order even modes.

The odd modes are purely negative-phase-velocity solutions. The TM dispersion characteristics display a bit more variety in the modes, but it is still seen that a large portion of the curves consists of negative-phase-velocity solutions. Furthermore, the TM results show mode crossings once again among the photonic crystal solutions. This phenomenon is mitigated slightly by the fact that the modes become split into positive- and negative-phase-velocity modes, meaning that some of the crossings do not take place. This is a result of the inclusion of DNG materials, but may not be due purely to the dispersive nature of these materials. However, still other crossings do in fact take place in spite of the mode splitting.

The field distributions for these results are also of interest. They may again be calculated by using the solutions obtained for the photonic crystal waveguide in the pseudo-photonic crystal waveguide field equations. This allows for a plot of the fields over a finite distance. The electric field distribution (e_y) is shown in Figure 6-12 for the TE_{0-} mode at 10.6 GHz and 10.7 GHz.

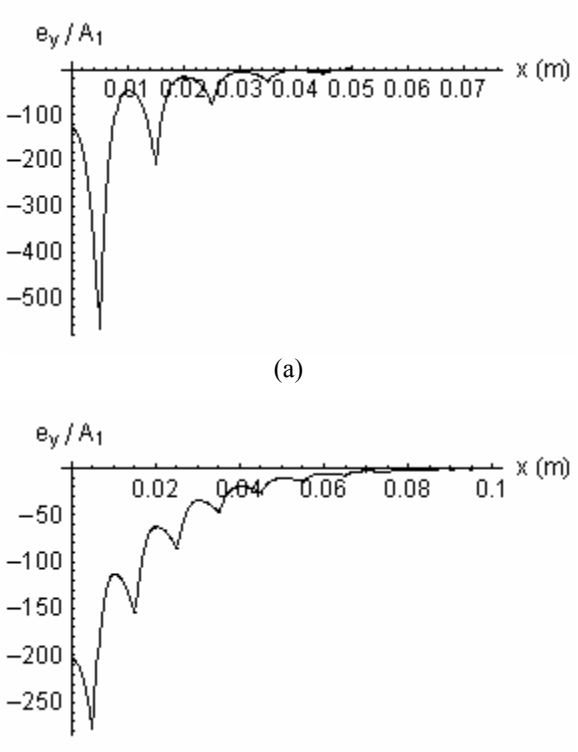


Figure 6-12. Electric field distribution (e_y) for the TE_{0-} mode of a photonic crystal waveguide whose dispersion characteristics are given in Figure 6-11(a). The field distribution is shown for solutions at 10.6 GHz (a) and 10.7 GHz (b).

The field distributions above reveal once again the surface-wave-like behavior seen with other DNG waveguides. This effect is manifested as very sharp field peaks around the core and cladding boundaries.

6.5 Summary

It has been shown that photonic crystal waveguides with DNG materials exhibit unique characteristics such as the elimination of any fundamental limitation on the propagation constant β. However, for the case of an ideal waveguide geometry a strange result was seen in the mode crossings which appear among the photonic crystal modes. The pseudo-photonic crystal waveguide has been shown to yield results very close to those of the full photonic crystal waveguide for a large number of layers. Although these results are only for conventional solutions rather than photonic crystal modes, this lends credence to the method of analysis used above.

7 Pulse Propagation in DNG Dielectric Waveguides

The previous chapters have dealt with various configurations of dielectric waveguides containing DNG metamaterials exclusively in the frequency domain. It behooves this investigation, however, not to neglect the time domain which provides a more pragmatic view of the behavior of these waveguides. The present discussion shall then focus on the propagation of pulses in a waveguide containing DNG metamaterials. A Fourier transform technique shall be used to convert the results obtained thus far into time domain data which will provide an understanding of the effect of DNG materials on the propagation of pulses in the waveguide.

7.1 Five-layer DNG waveguide

One of the most interesting aspects of the dispersion characteristics of DNG waveguides is the presence of double intramodal degeneracy. This degeneracy, as was seen in previous chapters, leads to the necessity of requiring a portion of the mode to have positive phase velocity and a portion to have negative phase velocity. This splits the mode into two distinct modes, but it ensures that both new modes have a causal positive group (energy) velocity. The effect that this has on the propagation of a pulse in the waveguide is of great interest and is one of the points of focus in this discussion. Additionally, the presence of both slow-wave and fast-wave modes adds another unique facet to the dispersion characteristics and which provides another point of interest for study in the time domain. Investigation of pulse propagation aids in understanding the consequences of these new characteristics.

It is helpful to examine a pulse which involves just a single mode in the waveguide. This limits the number of variable factors in the analysis and simplifies the

investigation. As a result, the fundamental mode is ideal since it alone exists over a certain range of frequencies, whereas modal degeneracy may exist at other frequencies. In order to examine a case where the fundamental mode involves both fast- and slow-wave solutions, the five-layer waveguide must be used. This allows for the excitation of a pulse with a frequency range that covers both fast- and slow-wave solutions as well as both positive- and negative-phase-velocity solutions, but all confined to the fundamental mode. A portion of the TE dispersion characteristics are shown in Figure 7-1 for a five-layer waveguide with a = 0.5cm, b = 1cm, $\mu 3 = \mu 0$, $\varepsilon 3 = \varepsilon 0$, $\mu 2 = \mu 0$, $\varepsilon 2 = 3.5\ \varepsilon 0$, and μ and ε governed by the DNG material parameters given in (4-65) and (4-66).

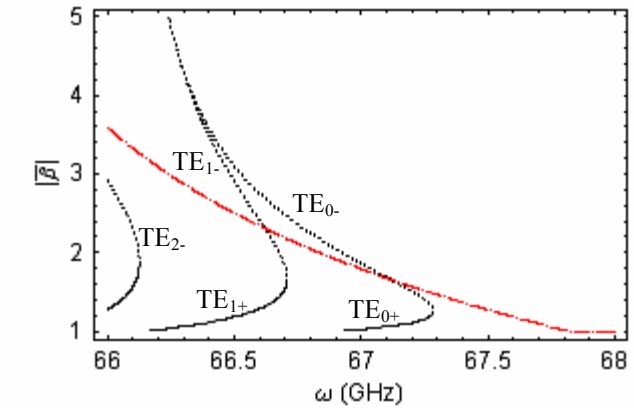


Figure 7-1. TE dispersion characteristics for a five-layer waveguide with both the positive-phase-velocity modes (solid black) and negative-phase-velocity modes (dashed black) shown as positive absolute values. The DNG refractive index n_1 (dot-dashed red) is shown for reference.

As can be seen in the above figure, there is a significant portion of the DNG range that includes only the fundamental TE_{0-} and TE_{0+} modes. This is an acceptable frequency range which meets the requirements specified earlier and shall then be used for this analysis.

7.2 Discrete Fourier analysis

Since the characteristic equations for planar dielectric waveguides must be solved numerically, in order to convert frequency domain results to time domain results a discrete Fourier transform technique must be used. This may simply involve a

discretized version of the Fourier transform integral. The continuous and discrete versions of the inverse Fourier integral are given below, respectively.

$$f(t) = \frac{1}{2\pi} \int_{-\infty}^{\infty} F(\omega) e^{j\omega t} \, d\omega \tag{7-1}$$

$$f(t) = \frac{1}{2\pi} \sum_{\omega} F(\omega) e^{j\omega t} \, \Delta\omega \tag{7-2}$$

Equation (7-2) allows for the use of discrete frequency domain data in determining the results in the time domain. In this case, the solutions β to the characteristic equation are actually functions of frequency $\beta(\omega)$. By converting these functions to the time domain using (7-2), the behavior of the waveguide may be examined in the time domain as well.

7.2.1 Gaussian pulse

A Gaussian pulse serves as a good pulse for analyzing propagation in a waveguide. Gaussian distributions are expressed mathematically as some amplitude multiplied by the exponential term $\exp[-(\zeta - \zeta_0)^2/\sigma^2]$, where ζ represents the frequency or time variable, ζ_0 is the location of the maximum of the curve and σ is a measure of the width thereof. A unique property of Gaussian distributions is that their Fourier transforms are also Gaussian. It then suffices to choose a Gaussian distribution in the frequency domain in order to obtain a Gaussian distribution in the time domain.

A Gaussian distribution of amplitude for the solutions with propagation constant β for the five-layer waveguide may be used to produce a Gaussian pulse in the time domain, since β is actually a function $\beta(\omega)$ with angular frequency ω. The mathematical expression for this amplitude distribution is given below, and its relationship with the dispersion characteristics is shown in Figure 7-2.

$$A(\omega) = \exp\left[-\frac{(\omega - 67.1\,\mathrm{GHz})^2}{0.002\,\mathrm{GHz}^2} \right] \tag{7-3}$$

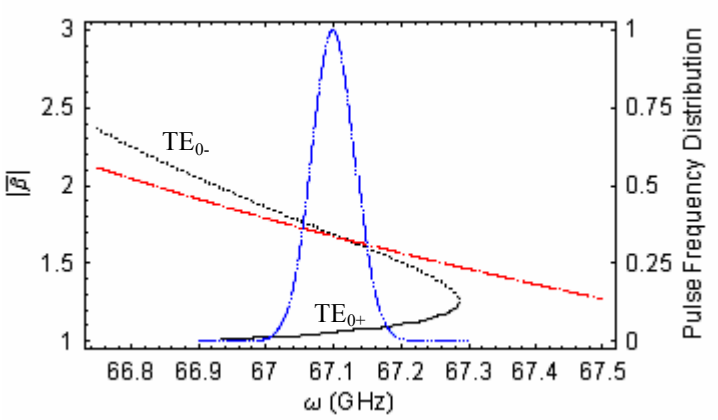


Figure 7-2. A magnification of the TE_{0+} (solid black) and TE_{0-} (dashed black) dispersion characteristics for the five-layer waveguide. The absolute value of the refractive index n_1 (dot-dashed red) is shown for reference. The pulse frequency amplitude distribution (dot-dot-dashed blue) is also shown.

Figure 7-2 shows that the amplitude distribution covers both positive- and negative-phase-velocity solutions along with both fast- and slow-wave solutions, all for only the fundamental TE mode. This Gaussian amplitude distribution may be shown to yield a Gaussian pulse in the time domain by using either (7-1) or (7-2) to perform the Fourier transform. A time domain plot of the results is shown in Figure 7-3.

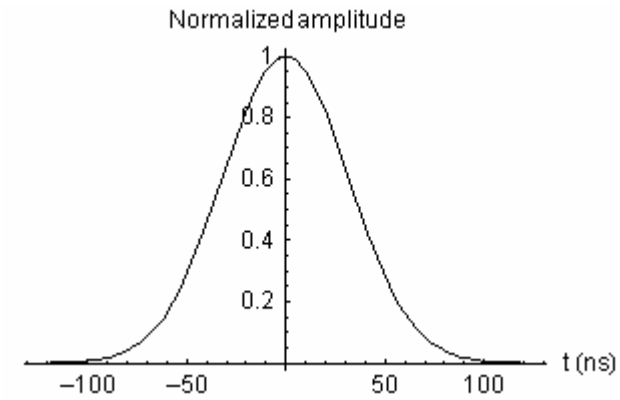


Figure 7-3. Absolute value of the normalized Fourier transform of (7-3) in the time domain.

It remains at this point only to treat the matter of the excitation of the modes.

7.3 Mode excitation

Modes may be excited in a waveguide by a number of different methods, but here the discussion shall focus on waves incident upon the end face of a waveguide. The analysis is most simple when plane waves are used, and since this portion of the analysis is more concerned with the actual propagation of the pulse in a waveguide and not so much on matters of mode excitation, plane waves only will be considered. The incident plane waves shall be considered from oblique angles in the x-z plane only, thus maintaining the two-dimensional nature of the analysis. This scenario is depicted in Figure 7-4.

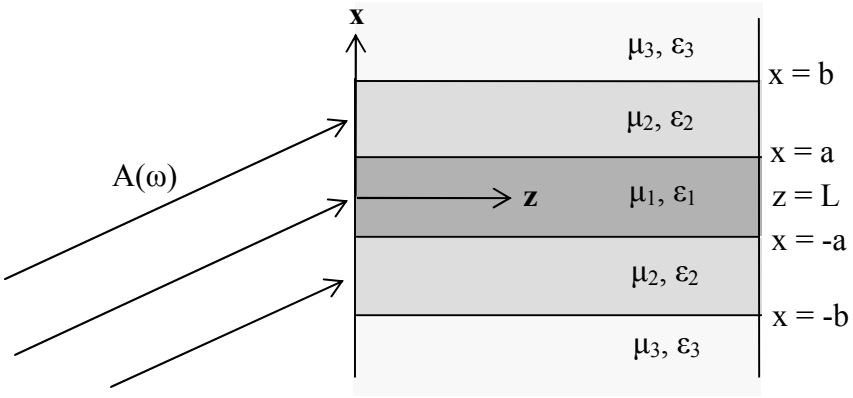


Figure 7-4. A plane wave with frequency distribution A(ω) incident on the face of a five-layer dielectric waveguide with length L.

The approach to solving this problem used here parallels that found in [83]. The total transverse fields $\mathbf{e}_{t\,tot}$ and $\mathbf{h}_{t\,tot}$ at the z = 0 end face in the waveguide may be expressed as sums of the fields in each mode j. This is expressed mathematically below for a single frequency, but for a spectrum of frequencies an additional superposition must be performed.

$$\mathbf{e}_{t\,tot}(x,y) = \sum_j a_j \mathbf{e}_{t\,j}(x,y) \tag{7-4}$$

$$\mathbf{h}_{t\,tot}(x,y) = \sum_j a_j \mathbf{h}_{t\,j}(x,y) \tag{7-5}$$

The modal amplitudes a_j are obtained from the following integral expression [83]:

$$a_j = \frac{1}{N_j}\int_S \mathbf{e}_{t\,tot} \times \mathbf{h}^*_{t\,j} \cdot \mathbf{z}\, dS = \frac{1}{N_j}\int_S \mathbf{e}^*_{t\,j} \times \mathbf{h}_{t\,tot} \cdot \mathbf{z}\, dS \tag{7-6}$$

Here, N_j is defined as follows:

$$N_j = \left|\int_S \mathbf{e}_{t\,j} \times \mathbf{h}^*_{t\,j} \cdot \mathbf{z}\, dS\right| = \left|\int_S \mathbf{e}^*_{t\,j} \times \mathbf{h}_{t\,j} \cdot \mathbf{z}\, dS\right| \tag{7-7}$$

Coupling of source fields into the waveguide may be treated by examining the transmitted fields just on the other side of the guide face ($z = 0^+$). These transmitted fields may be found through the use of (3-31) and (3-32) for perpendicular polarization or (3-38) and (3-39) for parallel polarization. These cases correspond to TE and TM polarization and couple only to either TE or TM modes in the waveguide, respectively. Each layer of the waveguide must be treated separately since the refractive indices may vary significantly. The amplitudes of the fields coupled into the j^{th} mode, a_j, may be determined using (7-6) and (7-7) where S is the surface area of the integral. Since there is uniformity in the y-direction and therefore no y-dependence for planar waveguides, the surface integrals become integrals over x with the integrals over y in the numerator and denominator canceling one another. The incident fields $\mathbf{E}_i$ and $\mathbf{H}_i$ at $z = 0$ are expressed below, where the wave vector $\mathbf{k}$ forms an angle θ with the z-axis, and the medium outside the waveguide is characterized by the refractive index n_i and the impedance η_i.

$$\mathbf{e}_i(x) = \mathbf{e}_0\, e^{-j\, n_i\, k_0\, x\, \sin\theta} \tag{7-8}$$

$$\mathbf{h}_i(x) = \frac{\hat{\mathbf{k}} \times \mathbf{e}_0}{\eta_i}\, e^{-j\, n_i\, k_0\, x \sin\theta} \tag{7-9}$$

Here, $\mathbf{e}_0$ is the amplitude of the electric field and $\hat{\mathbf{k}}$ is a unit vector in the direction of the wave vector $\mathbf{k}$.

7.4 Pulse propagation

All the necessary background is now in place for analyzing pulse propagation in the five-layer DNG dielectric waveguide. The even TE field distributions from (4-33) and (5-5) through (5-7) are needed for calculating the mode coupling amplitudes. Combining these fields, expressed as h_z, h_x and e_y, with the results of the preceding analysis allows the TE_0 mode amplitude a_0 to be calculated at an angular frequency ω according to the following expression.

$$a_0 = \frac{1}{N_0} \int_{-\infty}^{\infty} \left[e_0 \, T_{\perp in} \, T_{\perp out} \, e^{-j n_i k_0 x \sin\theta} \, \mathbf{y} \times \left(\mathbf{x} \, h_x^* + \mathbf{z} \, h_z^* \right) \right] \cdot \mathbf{z} \, dx \tag{7-10}$$

The term N_0 is given below.

$$N_0 = \left| \int_{-\infty}^{\infty} \left[e_y \, \mathbf{y} \times \left(\mathbf{x} \, h_x^* + \mathbf{z} \, h_z^* \right) \right] \cdot \mathbf{z} \, dx \right| \tag{7-11}$$

Here, $T_{\perp in}$ and $T_{\perp out}$ are expressed by (3-31) with θ_t defined by (3-33). The term $T_{\perp in}$ is the transmission coefficient for the end face of the waveguide at z = 0, and the term $T_{\perp out}$ is the transmission coefficient for the end face of the waveguide at z = L. This accounts for the entrance of the pulse at the front of the guide and the exit of the pulse at the end of the guide. Equation (7-10) may be further specified by assigning the Gaussian distribution A(ω) of (7-3) to e_0. Adding the spatial and frequency arguments in order to increase clarity, (7-10) and (7-11) may be rewritten below.

$$a_0(\omega) = \frac{1}{N_0(x,\omega)} \int_{-\infty}^{\infty} \left\{ A(\omega) \, T_{\perp in}(x,\omega) T_{\perp out}(x,\omega) \, e^{-j n_i k_0 x \sin\theta} \, \mathbf{y} \times \left[\mathbf{x} \, h_x^*(x,\omega) + \mathbf{z} \, h_z^*(x,\omega) \right] \right\} \cdot \mathbf{z} \, dx \tag{7-12}$$

$$N_0(x,\omega) = \left| \int_{-\infty}^{\infty} \left\{ e_y(x,\omega)\mathbf{y} \times \left[\mathbf{x}\, h_x^*(x,\omega) + \mathbf{z}\, h_z^*(x,\omega) \right] \right\} \cdot \mathbf{z}\, dx \right| \qquad (7\text{-}13)$$

The expressions in (7-12) and (7-13) rely only on the field distributions of the TE_0 mode, and the incident field distribution which in turn depends on the amplitude distribution A(ω) and the transmission coefficient distributions $T_{\perp in}(x,\omega)$ and $T_{\perp out}(x,\omega)$. The use of the transmission coefficients in this manner is an approximation. The fields and transmission coefficient vary depending on the layer of the waveguide. It remains only to calculate the relevant values of β at each frequency and perform the Fourier transform in (7-2). The discrete transform will be used since the fact that β must be calculated numerically implies that it can only be found at discrete values of the frequency ω.

7.4.1 Numerical results

Using the waveguide whose dispersion characteristics are shown in Figures 7-1 and 7-2, the propagation of a Gaussian pulse may now be studied. The β values over the relevant frequency range may be calculated numerically along with the field distributions for those solutions. Then performing the integrations (7-12) and (7-13), the coefficient $a_0(\omega)$ is the fraction of the power transmitted to the waveguide that is in the TE_0 mode. The initial field coefficient A_1 in (5-5) through (5-7) is assumed to be equal to this coefficient $a_0(\omega)$. The electric field at x = 0 shall be considered in the following analysis. Furthermore, the output from a length L of the waveguide will be of interest here.

The numerical results are shown in Figure 7-5 for the propagation of a Gaussian pulse in length L of the five-layer waveguide and with the pulse emanating from a plane wave source with the frequency spectrum in (7-3). The plane waves are assumed, for simplicity, to be normally incident upon the z = 0 face of the waveguide, meaning that in (7-41), θ = 0.

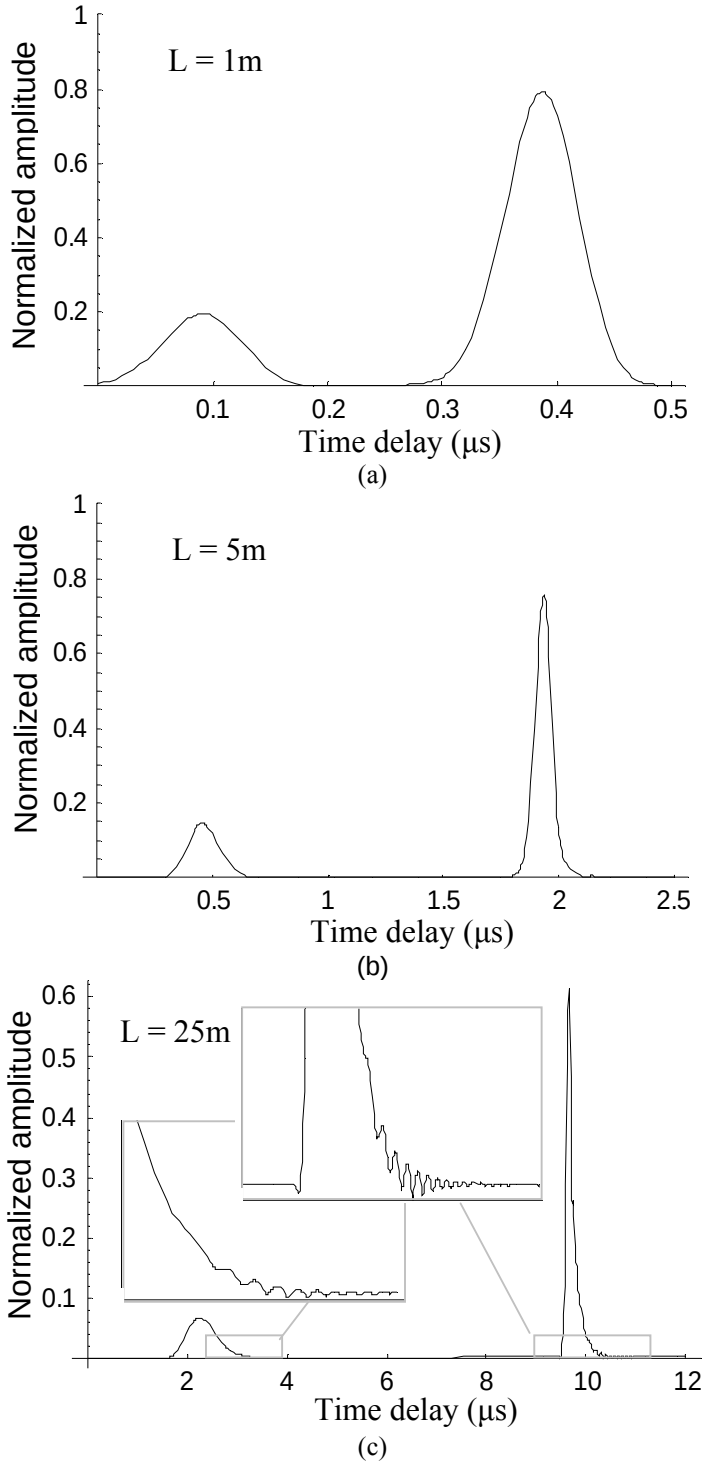


Figure 7-7. Absolute value of the normalized electric field output at x = 0 of a five-layer DNG waveguide of length L = 1m (a), L = 5m (b) and L = 25m (c), plotted in terms of the time delay. Insets in (c) show magnifications of the pulse tails.

As seen in the above figure, the splitting of the TE0 mode into the TE_{0+} and TE_{0-} modes results in the input pulse being split into two separate pulses, each with its own unique but positive group velocity corresponding to the slope of the dispersion curves in Figure 7-2 and its own amount of pulse dispersion corresponding to the change in the slope of those curves. The value of the energy (group) velocity at 67.1GHz for TE_{0+} is about 10.7m/μs whereas it is about 2.5m/μs for TE_{0-}, and these values are very close to the associated time delays for the pulses in various lengths of the guide. This lends credence to these numerical results.

The credibility of the interpretation of Chapter 4 requiring the degenerate dispersion curves to be split is hereby buttressed. Although the pulse is split, both new pulses have a causal positive energy velocity as would be expected since the source is located at $z = -\infty$. Furthermore, the dispersive effects of the inclusion of DNG materials are also seen in the figure as the pulses broaden and acquire ringing in their tails for long lengths of the waveguide.

7.5 Summary

This section has dealt with pulse propagation in a five-layer DNG dielectric waveguide by way of a Fourier transform technique. The numerical results are in agreement with the interpretation made in Chapter 4 concerning the splitting of intramodally degenerate modes into separate modes, each with positive group velocity. This resulted in the splitting of an input pulse into two separate pulses, each associated with either the positive- or negative-phase-velocity mode (TE_{0+} and TE_{0-} in this case). This analysis has served as a very realistic and helpful closing topic for the investigation into DNG dielectric waveguides.

8 Conclusion

This investigation has examined the inclusion of DNG metamaterials in various planar dielectric waveguide configurations. All the mathematical tools for the analysis have been derived directly and thoroughly from Maxwell's equations for the general case of either DNG or DPS materials. A formulation for symmetrically-clad N-layer waveguides was presented and applied to the three-layer, five-layer, photonic crystal and pseudo-photonic crystal waveguides containing DNG materials. The results obtained for the five-layer waveguide were used through Fourier analysis to examine pulse propagation in the guide.

8.1 Summary of results

Each geometry examined during this investigation has revealed new and interesting characteristics which have not yet been observed in DPS-only waveguides of similar type. Variations on the general N-layer formulation were used throughout to produce results in the frequency domain for waveguides containing DNG materials. The geometries analyzed in detail were the three-layer (slab) waveguide, the five-layer (quadruple-clad) waveguide, the photonic crystal waveguide and the pseudo-photonic crystal waveguide. A causal material model based on experimental results found in the literature for a DNG metamaterial was used. This model included both dispersion and loss, but loss was neglected for the first portion of the investigation but was treated later through perturbation theory. It was found that this approach was warranted by comparing the perturbation results with the results for an exact method.

8.1.1 Three-layer DNG waveguide

The three-layer DNG waveguide analysis presented in the literature was revisited by deriving the characteristic equations and cutoff conditions. Based on both the analytical and numerical results, the following key characteristics of this waveguide were re-emphasized:

- The presence of slow-wave modes in addition to fast-wave modes.
- The absence of the fundamental fast-wave mode.
- Double intramodal degeneracy.
- Surface-wave-like field distributions with energy focused at the slab boundaries.

Further completing the analysis, a new interpretation was given to the phenomenon of intramodal degeneracy. This led to the following new findings:

- All modes have positive group velocity and, thus, positive energy velocity.
- Degenerate modes actually exist as two separate modes, one with positive phase velocity and one with negative phase velocity, leading to the requirement for a new notation for classifying the modes which adds a '+' or '-' sign to the numeral subscript, such as the TE_{0+} and TE_{0-}, with the sign denoting the sense of the phase velocity.

8.1.2 Five-layer DNG waveguide

Applying the same N-layer formulation as was used for the three-layer waveguide, numerical results for the five-layer waveguide were also obtained. These results, along with the analytical results for the characteristic equations and cutoff conditions, led to the following characteristics which have not been seen elsewhere:

- Presence of the fundamental fast-wave mode for some configurations.
- Absence of some higher order modes.

- Reversal of conventional even/odd mode order when DNG inner cladding is used.
- Appearance of brand new modes (*i.e.*, new instances of particular modes) upon adjusting cladding widths.

In conventional waveguides, all modes are present and in the expected order (*e.g.*, TE_0, TE_1, TE_2, etc. for TE modes). It has been shown, however, that the inclusion of DNG materials leads to the unique modal characteristics listed above. These are new phenomena not seen in the conventional waveguides.

8.1.3 Photonic crystal DNG waveguides

The photonic crystal DNG waveguide was analyzed using ray analysis. The pseudo-photonic crystal DNG waveguide was analyzed using a slight variation of the N-layer formulation used for the three- and five-layer waveguides. The pseudo-photonic crystal waveguide was found to yield numerical results almost identical to those of the photonic crystal waveguide when a large number of layers were used. The main results found during the analysis are as follows:

- There exist no fundamental limitations on the value of the propagation constant β for the full photonic crystal waveguide.
- Mode crossings appear in the dispersion characteristics of the photonic crystal waveguide but may be eliminated in some cases by the use of DNG materials since degenerate modes must be split yielding some modes with positive values for the propagation constant and some modes with negative values for the propagation constant.

8.1.4 Pulse propagation in DNG waveguides

Finally, pulse propagation in the time domain was examined for a five-layer DNG waveguide. A plane wave with a Gaussian frequency distribution over the TE_{0+} and TE_{0-}

modes was incident upon the end face of the waveguide. Propagation of the pulse in the guide was studied. The following key results were presented:

- Due to the split mode resulting from intramodal degeneracy, input pulses are split into two new pulses, each with its own associated group velocity and dispersion corresponding to either the positive- or negative-phase-velocity mode.
- The causal behavior of the propagating pulses buttresses the interpretation of the dispersion characteristics requiring that intramodally degenerate modes be split into two new modes.

This investigation has produced many new results which have not been previously observed in DPS-only waveguides. Also, a more exhaustive examination of N-layer dielectric waveguides with DNG materials has been performed than was reported in the literature. Furthermore, the time domain results have provided the first look into pulse propagation in a waveguide where intramodal degeneracy has been dealt with in a causally acceptable fashion.

8.2 Suggestions for further study

There still remains many areas which have not yet been investigated. Couplers involving these waveguides is one area of application not treated in depth here. The presence of both positive- and negative-phase-velocity modes is a unique feature which may have significant repercussions on the coupling behavior of dielectric waveguides containing DNG materials. Furthermore, other geometries such as the circularly cylindrical fiber geometry have also been unmentioned and yet are worthy of investigation since fibers, for example, are a very important and highly used technology. New effects exclusive to other geometries may present themselves upon closer examination. The numerical study of waveguides with multiple types of DNG materials (*i.e.*, different material models) may also yield further interesting results, as this investigation only examined the use of one DNG material model, and this model was

only used for either the core or one single set of cladding layers. Also, the inclusion of other exotic materials in tandem with DNG materials may be another avenue to new phenomena not yet reported here or elsewhere in the literature.

References

[1] V.G. Veselago, "The electrodynamics of substances with simultaneously negative values of ε and μ," *Soviet Physics Uspekhi*, Vol. 10, No. 4, 1968.

[2] D.R. Smith, W.J. Padilla, D.C. Vier, S.C. Nemat-Nasser and S. Schultz, "Composite medium with simultaneously negative permeability and permittivity," *Physical Review Letters*, Vol. 84, No. 18, 2000.

[3] D.R. Smith and N. Kroll, "Negative refractive index in left-handed materials," *Physical Review Letters*, Vol. 85, No. 14, 2000.

[4] R.A. Shelby, D.R. Smith and S. Schultz, "Experimental verification of a negative index of refraction," *Science*, Vol. 292, 2001.

[5] R.A. Shelby, D.R. Smith, S.C. Nemat-Nasser and S. Schultz, "Microwave transmission through a two-dimensional, isotropic, left-handed metamaterial," *Applied Physics Letters*, Vol. 78, No. 4, 2001.

[6] J.B. Pendry, "Negative refraction makes a perfect lens," *Physical Review Letters*, Vol. 85, No. 18, 2000.

[7] A. Lakhtakia, "On perfect lenses and nihility," *International Journal of Infrared and Millimeter Waves*, Vol. 23, 2002.

[8] N. Garcia and M. Nieto-Vesperinas, "Left-handed materials do not make a perfect lens," *Physical Review Letters*, Vol. 88, No. 20, 2002.

[9] P.M. Valanju, R.M. Walser and A.P. Valanju, "Wave refraction in negative-index media: always positive and very inhomogeneous," *Physical Review Letters*, Vol. 88, No. 18, 2002.

[10] N. Garcia and M. Nieto-Vesperinas, "Is there an experimental verification of a negative index of refraction yet?" *Optics Letters*, Vol. 27, No. 11, 2002.

[11] V.G. Veselago, "Formulating Fermat's principle for light traveling in negative refraction materials," *Physics-Uspekhi*, Vol. 45, No. 10, 2002.

[12] R.W. Ziolkowski and E. Heyman, "Wave propagation in media having negative permittivity and permeability," *Physical Review E*, Vol. 64, 2001.

[13] N. Engheta and A. Alu, "Radiation from a travelling-wave current sheet at the interface between a conventional material and a material with negative μ and ε," *Microwave and Optics Technology Letters*, Vol. 35, No. 6, 2002.

[14] R.W. Ziolkowski, "Superluminal transmission of information through electromagnetic metamaterials," *Physics Review E*, Vol. 64, No. 5, 2001.

[15] A.N. Lagarkov and V.N. Kisel, "Electrodynamic properties of simple bodies made of materials with negative permeability and negative permittivity," *Doklady Physics*, Vol. 46, N0. 3, 2001.

[16] S.A. Tretyakov *et al.*, "Modelling and microwave propagation of artificial materials with negative parameters," *Advances in Electromagnetics of Complex Media and Metamaterials*, 2002.

[17] M. Mojahedi, O. Siddiqui, J. Woodley and G.V. Eleftheriades, "Pulse Propagation and negative group delay in metamaterials," *Progress in Electromagnetics Research Symposium*, 2002.

[18] M. Mojahedi, "Superluminal velocities in causal media," *KITP mini program on Quantum Optics*, 2002.

[19] J.B. Pendry, A.J. Holden, D.J. Robbins and W.J. Stewart, "Magnetism from conductors and enhanced nonlinear phenomena," *IEEE Transactions on Microwave Theory and Techniques*, Vol. 47, No. 11, 1999.

[20] R.N. Bracewell, "Analogues of an ionized medium: applications to the ionosphere," *Wireless Engineer,* Vol. 31, 1954.

[21] W. Rotman, "Plasma simulation by artificial dielectrics and parallel-plate media," *IRE Transactions on Antennas and Propagation*, Vol. AP10, 1962.

[22] C.R. Simovski and P.A. Belov, "Backward wave region and negative material parameters of a structure formed by lattices of wires and split-ring resonators," *IEEE Transactions on Antennas and Propagation, Special Issue on Metamaterials*, 2003.

[23] S.A. Tretyakov, S. Maslovski and P.A. Belov, "An analytical model of metamaterials based on loaded wire dipoles," *IEEE Transactions on Antennas and Propagation*, Vol. 51, No. 10, 2003.

[24] R. Marques, F. Medina and R. Rafii-El-Idrissi, "Role of bianisotropy in negative permeability and left-handed metamaterials," *Physical Review B*, Vol. 65, 2002.

[25] R. Marques, F. Mesa, J. Martel and F. Medina, "Comparative analysis of edge- and broadside-coupled split ring resonators for metamaterial design - theory and experiment," *IEEE Transactions on Antennas and Propagation*, Vol. 51, No. 10, 2003.

[26] P. Markos, I. Rousochatzakis and C.M. Soukoulis, "Transmission losses in left-handed materials," *Physical Review B*, Vol. 65, 2002.

[27] M.W. Feise, P.J. Bevelacqua and J.B. Schneider, "Effects of surface waves on the behavior of perfect lenses," *Physical Review B*, Vol. 66, 2002.

[29] I.V. Lindell, S.A. Tretyakov, K.I. Nikoskinen and S. Ilvonen, "BW media - media with negative parameters, capable of supporting backward waves," *Microwave and Optical Technology Letters*, Vol. 31, No. 2, 2001.

[30] D.R. Smith, D. Schurig and J.B. Pendry, "Negative refraction of modulated electromagnetic waves," *Applied Physics Letters*, Vol. 81, No. 15, 2002.

[31] S. Foteinopoulou, E.N. Economou and C.M. Soukoulis, "Refraction in media with negative refractive index," *Physical Review Letters*, Vol. 90, No. 4, 2003.

[32] D.R. Fredkin and A. Ron, "Effectively left-handed (negative index) composite material," *Applied Physics Letters*, Vol. 81, No. 10, 2002.

[33] S.A. Tretyakov, "Meta-materials with wideband negative permittivity and permeability," *Microwave and Optical Technology Letters*, Vol. 31, No. 3, 2001.

[34] C. Caloz and T. Itoh, "Application of the transmission line theory of left-handed (LH) materials to the realization of a microstrip 'LH line,'" *Proceedings IEEE AP-S*, 2002.

[35] G.V. Eleftheriades, A.K. Iyer and P.C. Kremer, "Planar negative refractive index media using periodically L-C loaded transmission lines," *IEEE Transactions on Microwave Theory and Techniques*, Vol. 50, No. 12, 2002.

[36] A.K. Iyer and G.V. Eleftheriades, "Negative refractive index metamaterials supporting 2-D waves," *IEEE MTT-S International Microwave Symposium Digest*, Vol. 2, 2002.

[37] R. Marques, J. Martel, F. Mesa and F. Medina, "A new 2D isotropic left-handed metamaterial design: theory and experiment," *Microwave and Optical Technology Letters*, Vol. 35, No. 5, 2002.

[38] R.W. Ziolkowski and A.D. Kipple, "Application of double negative materials to increase the power radiated by electrically small antennas," *IEEE Transactions on Antennas and Propagation*, Vol. 51, No. 10, 2003.

[39] A. Grbic and G.V. Eleftheriades, "Experimental verification of backward-wave radiation from a negative refractive index metamaterial," *Journal of Applied Physics*, Vol. 92, No. 10, 2002.

[40] A. Grbic and G.V. Eleftheriades, "A backward-wave antenna based on negative refractive index L-C networks," *IEEE Antennas and Propagation Society International Symposium*, 2002.

[41] G. Tayeb, S. Enoch, P. Sabouroux, N. Guérin and P. Vincent, "Compact directive antennas using metamaterials," *12th International Symposium on Antennas*, 2002.

[42] J.B. Pendry, A.J. Holden, W.J. Stewart and I. Youngs, "Extremely low frequency plasmons in metallic mesostructures," *Physical Review Letters*, Vol. 76, No. 25, 1996.

[43] J.B. Pendry, A.J. Holden, D.J. Robbins and W.J. Stewart, "Low frequency plasmons in thin wire structures," *Journal of Physics: Condensed Matter*, Vol. 10, 1998.

[44] D. Sievenpiper, L. Zhang, R.F.J. Broas, N.G. Alexopolous and E. Yablonovitch, "High-impedance electromagnetic surfaces with forbidden frequency band," *IEEE Transactions on Microwave Theory and Techniques*, Vol. 47, No. 11, 1999.

[45] J. McVay, A. Hoorfar and N. Engheta, "Radiation characteristics of microstrip dipole antennas over a high-impedance metamaterial surface made of Hilbert inclusions," *IEEE MTT-S Digest*, 2003.

[46] A.K. Iyer, P.C. Kremer and G.V. Eleftheriades, "Experimental and theoretical verification of focusing in a large, periodically loaded transmission line negative refractive index metamaterial," *Optics Express*, Vol. 11, No. 7, 2003.

[47] A. Grbic and G.V. Eleftheriades, "Growing evanescent waves in negative-refractive-index transmission-line media," *Applied Physics Letters*, Vol. 82, No. 12, 2003.

[48] G.V. Eleftheriades, O. Siddiqui and A.K. Iyer, "Transmission line models for negative refractive index media and associated implementations without excess resonators," *IEEE Microwave and Wireless Components Letters*, Vol. 13, No. 2, 2003.

[49] A. Grbic and G.V. Eleftheriades, "Dispersion analysis of a microstrip-based negative refractive index periodic structure," *IEEE Microwave and Wireless Components Letters*, Vol. 13, No. 4, 2003.

[50] A. Grbic and G.V. Eleftheriades, "Negative refraction, growing evanescent waves, and sub-diffraction imaging in loaded transmission-line metamaterials," *IEEE Transactions on Microwave Theory and Techniques*, Vol. 51, No. 12, 2003.

[51] A.K. Iyer, A. Grbic and G.V. Eleftheriades, "Sub-wavelength focusing in loaded transmission line negative refractive index metamaterials," *IEEE MTT-S International Microwave Symposium Digest*, Vol. 1, 2003.

[52] R.W. Ziolkowski and C.-Y. Cheng, "Tailoring double negative metamaterial responses to achieve anomalous propagation effects along microstrip transmission lines," *IEEE MTT-S International Microwave Symposium Digest*, Vol. 1, 2003.

[53] R. Islam and G.V. Eleftheriades, "A planar metamaterial co-directional coupler that couples power backwards," ?.

[54] C. Caloz and T. Itoh, "A novel mixed conventional microstrip and composite right/left-handed backward-wave directional coupler with broadband and tight coupling characteristics," *IEEE Microwave and Wireless Components Letters*, Vol. 14, No. 1, 2004.

[55] M.A. Antoniades and G.V. Eleftheriades, "Compact, linear, lead/lag phase shifters using negative refractive index metamaterials," *Antennas and Wireless Propagation Letters*, Vol. 2, No. 1, 2003.

[56] L. Liu, C. Caloz, C.-C. Chang and T. Itoh, "Forward coupling phenomena between artificial left-handed transmission lines," *Journal of Applied Physics*, Vol. 92, No. 9, 2002.

[57] K.G. Balmain, A.A.E. Lüttgen and P.C. Kremer, "Resonance cone formation, reflection, refraction, and focusing in a planar anisotropic metamaterial," *IEEE Antennas and Wireless Propagation Letters*, Vol 1, 2002.

[58] C. Caloz, C.-C. Chang and T. Itoh, "Full-wave verification of the fundamental properties of left-handed materials in waveguide configurations," *Journal of Applied Physics*, Vol. 90, No. 11, 2001.

[59] R. Marqués, J. Martel, F. Mesa and F. Medina, "Left-handed-media simulation and transmission of EM waves in subwavelength split-ring-resonator-loaded metallic waveguides," *Physical Review Letters*, Vol. 89, No. 18, 2002.

[60] I.V. Shadrivov, A.A. Sukhorukov and Y.S. Kivshar, "Guided modes in negative-refractive-index waveguides," *Physical Review E*, Vol. 67, 2003.

[61] B.-I. Wu, T.M. Grzegorczyk, Y. Zhang and J.A. Kong, "Guided modes with imaginary transverse wave number in a slab waveguide with negative permittivity and permeability," *Journal of Applied Physics*, Vol. 93, No. 11, 2003.

[62] H. Salehi, S.K. Chaudhuri and R.R. Mansour, "Unusual mode propagation characteristics of negative index slab waveguides," *IEEE Antennas and Propagation Society International Symposium*, Vol. 1A, 2005.

[63] G. D'Aguanno, N. Mattiucci, M. Scalora and M.J. Bloemer, "TE and TM guided modes in an air waveguide with negative-index-material cladding," *Physical Review E*, Vol. 71, No. 4, 2005.

[64] A.V. Novitsky and L.M. Barkovsky, "Guided modes in negative-refractive-index fibres," *Journal of Optics A*, Vol. 7, No. 2, 2005.

[65] I.S. Nefedov and S.A. Tretyakov, "Waveguide containing a backward-wave slab," *Radio Science*, Vol. 38, No. 6, 2003.

[66] A. Alu and N. Engheta, "Resonances in sub-wavelength cylindrical structures made of pairs of double negative (DNG) and double positive (DPS) or ε-negative (ENG) and μ-negative (MNG) coaxial shells," *Proceedings of the International Conference on Electromagnetics in Advanced Applications*, 8-12, 2003.

[67] A. Alu and N. Engheta, "Guided modes in a waveguide filled with a pair of single-negative (SNG), double-negative (DNG), and/or double-positive (DPS) layers," *IEEE Transactions on Microwave Theory and Techniques*, Vol. 52, No. 1, 2004.

[68] A. Peacock and N. Broderick, "Guided modes in channel waveguides with a negative index of refraction," *Optics Express*, Vol. 11, No. 20, 2003.

[69] K. Halterman, J.M. Elson and P.L. Overfelt, "Characteristics of bound modes in coupled dielectric waveguides containing negative index media," *Optics Express*, Vol. 11, No. 6, 2003.

[70] I.V. Shadrivov, R.W. Ziolkowski, A.A. Zharov and Y.S. Kivshar, "Excitation of guided waves in layered structures with negative refraction," *Optics Express*, Vol. 13, No. 2, 2005.

[71] R. Ruppin, "Extinction properties of a sphere with negative permittivity and permeability," *Solid State Communications*, Vol. 116, 2000.

[72] J. Li, L. Zhou, C.T. Chan and P. Sheng, "Photonic bandgap from a stack of positive and negative index materials," *Physical Review Letters*, Vol. 90, No. 8, 2003.

[73] Y. Hao, L. Lu and C.G. Parini, "Time-domain modeling on wave propagation through single/multilayer left-handed meta-material slabs," *Twelfth International Conference on Antennas and Propagation*, Vol. 2, 2003.

[74] I.V. Shadrivov, A.A. Sukhorukov and Y.S. Kivshar, "Beam shaping by a periodic structure with negative refraction," *Applied Physics Letters*, Vol. 82, No. 22, 2003.

[75] K.-Y. Kim, "Photon tunneling in composite layers of negative- and positive-index media," *Physical Review E*, Vol. 70, No. 4, 2004.

[76] C.J. Fu, Z.M. Zhang and D.B. Tanner, "Energy transmission by photon tunneling in multilayer structures including negative index materials," *Transactions of the ASME*, Vol. 127, 2005.

[77] I.V. Shadrivov, A.A. Sukhorukov and Y.S. Kivshar, "Complete bandgaps in one-dimensional left-handed periodic structures," *Physical Review Letters*, Vol. 95, No. 19, 2005.

[78] A.A. Houck, J.B. Brock and I.L. Chuang, "Experimental observations of a left-handed material that obeys Snell's law," *Physical Review Letters*, Vol. 90, No. 13, 2003.

[79] M.W. McCall, A. Lakhtakia and W.S. Weiglhofer, "The negative index of refraction demystified," *European Journal of Physics*, Vol. 23, 2002.

[80] Robert E. Collin, *Foundations for Microwave Engineering*, McGraw-Hill, Inc., USA, 1992.

[81] Constantine A. Balanis, *Advanced Engineering Electromagnetics*, John Wiley & Sons, Inc., USA, 1989.

[82] Soheilla Mirlohi, "Exact solutions of planar photonic crystal waveguides with infinite claddings," Master's Thesis, Virginia Polytechnic Institute and State University, 2003.

[83] Allan W. Snyder and John D. Love, *Optical Waveguide Theory*, Chapman and Hall, New York, USA, 1983.

Vita

Jeffrey R. Clark was born on December 8, 1977 in Rochester, New York. He graduated Summa Cum Laude with a Bachelor of Science in physics from the University of Richmond in 2001. In 2003, he earned a Master of Science in electrical engineering from Virginia Polytechnic Institute and State University. He has accepted a Junior Electrical Engineer position somewhere near Northern Virginia.